DLR
Deutsches Zentrum
für Luft- und Raumfahrt
German Aerospace Center

Master Thesis

Transient Measurement Method for the Determination of Parabolic Trough Receiver Heat Losses under Field Conditions - Testing and Optimization

Almería, September 30, 2014

Henning Heppner

Matriculation Number: 288411

Supervisors:
M.Sc. Dipl.-Ing. Simon Caron
Prof. Dr.-Ing. Robert Pitz-Paal

German Aerospace Center
Institute of Solar Research
Paseo de Almeria, 73 , 04001 Almería, Spain

RWTH AACHEN UNIVERSITY

Table of Contents

Abstract

Parabolic trough collectors represent one of the current most popular technology among concentrating solar power plants. Parabolic shaped mirrors concentrate solar radiation on a line of receiver tubes. These receiver tubes consist of an absorber steel tube inserted in a concentrical glass envelope. To provide an accurate measurement technique for the determination of parabolic trough receiver heat losses under field conditions, a transient infrared thermography measurement for the determination of parabolic trough receiver heat losses is developed.

The principle of this measurement method is to apply a thermal excitation to the absorber tube temperature and to investigate the glass envelope temperature response. Both temperature signals are measured with infrared thermography. The glass envelope temperature dynamic response is investigated with respect to the absorber temperature excitation to provide a diagnosis about the thermal properties of the investigated receiver. The experimental setup consists of a radiation shield, which is mounted around the glass envelope. It reduces thermal radiation heat losses from the glass envelope to the ambient to a minimum. Installed fans on one side of the radiation shield induces a steady air flow inside of the shield.

The measurement method was tested in previous measurement campaigns under laboratory conditions. This report covers the first implementation and optimization of the transient heat loss measurement method under field conditions. During the first field measurements that ambient conditions such as wind speed, wind direction and ambient temperature gradients have a significant influence on the measurement quality. A reproducibility of results could not be proven. Corrective measures were investigated to reduce the influence of ambient conditions.

The installation of a first wind screen on the radiation shield could decrease the influence of wind. A second wind screen was then designed and its impact on the experimental setup was tested under laboratory conditions. The measurements obtained with the original setup could be approached with the new wind screen by increasing the ventilation power of the radiation shield. Laboratory measurements showed a better reproducibility than first field measurements.

The optimized experimental setup was tested during a second field measurement campaign. The influence of wind could be eliminated up to 6 m/s, while the influence of ambient temperature variations remained critical. During this measurement campaign, the reproducibility of field experiments could be improved, reducing the uncertainty of heat loss measurements to 18.7 W/m.

Preamble

I hereby declare to have written the present master thesis on my own having used no other than the listed resources and tools. All contents cited from published or unpublished documents are indicated as such.

Almería, September 30, 2014.

Nomenclature

Latin Symbols

Symbol	Description	Unit
A	amplitude ratio	—
c_1	first radiation constant	$3.742 \cdot 10^{-16}$ W·m^2
c_2	second radiation constant	$1.439 \cdot 10^{-2}$ m·K
c_p	specific isobaric heat capacity	J /(kg·K)
E	irradiance	W/m^2
i	current	A
K	gain constant	—
k	thermal conductivity	W/(K·m)
L	radiance	W/(m^2·sr)
l	length	m
I	current	A
M	radiant emittance	W/m^2
$\dot{m}$	mass flow	kg/s
P	power, radiant flux	W
$\dot{Q}$	heat flow	W
$\dot{q}'$	specific heat flow	W/m
$\dot{q}$	heat flux	W/m^2
r	radius	m
T	temperature	K, °C
$\overline{T}$	mean temperature	K, °C
$\hat{T}$	temperature amplitude	K
$\tilde{T}$	temperature lift	K
t	time	s
u	voltage	V
V	volume	m^3

Greek Symbols

Symbol	Description	Unit
α	absorptivity	—
ϵ	emissivity	—
η_0	optical efficiency coefficient	—
λ	wavelength	m
ρ	density,	kg/m^3
	reflectivity	—
σ	standard deviation	—
σ_B	Stefan-Boltzmann constant	$5.670 \cdot 10^{-8}$ $W/(m^2 \cdot K^4)$
τ	transmissivity	—
τ_{PT1}	time constant	s
ω	angular frequency	rad/s
φ	phase shift	rad
Ω	solid angle	sr

Indices

Symbol	Description
abs	absorber
air	air
algo	algorithm
ann	annulus
amb	ambient
b	blackbody,
	bottom
coll	collector
cond	conductive
conv	convective
gl	glass
global	global
i	inner,
	inlet

continued on next page

Indices

Symbol	Description
in	in
λ	spectral
loss	heat loss
max	maximum
min	minimum
norm	normalized
o	outer,
	outlet
out	out
pyr	pyrometer
rad	radiation
sky	sky
solar	solar
t	top
th	thermal

Abbreviations

Symbol	Description
AR	Amplitude Ratio
CSP	Concentrating Solar Power
DLR	German Aerospace Center
DNI	Direct Normal Irradiance
HCE	Heat Collector Element
HTF	Heat Transfer Fluid
IR	Infrared
KONTAS	Konzentrator-Teststand Almería Spanien; Concentrator test bench Almería Spain
NETD	Noise Equivalent Temperature Difference
NREL	National Renewable Energy Laboratory
MENA	Middel East & North Africa
PS	Phase Shift

continued on next page

Abbreviations

Symbol	Description
PSA	Plataforma Solar de Almería
PTC	Parabolic Trough Collector
PTR	Parabolic Trough Receiver
STPP	Solar Thermal Power Plant
TC	thermocouple
TCU	temperature Control Unit
WP	Working Point

List of Figures

List of Tables

1 Introduction

1.1 Motivation

The International Energy Agency (IEA) forecasts an annual increase of 1.7 % in its world energy outlook for the global primary energy consumption [IEA, 2004]. While the demand for energy in industrialized countries is nearly at its top, two-thirds of the upcoming increase is expected to be in developing and newly industrializing countries, such as China, India or Brazil. Conventional fossil energy sources play a predominant role in the coverage of the current energy consumption. It is a desirable and worthwhile ambition to prevent this dominance in the future, because of the impact on climate change as well as environmental damages. In addition, the course of increasing energy demand meets the shortage of the limited and not renewable energy sources. Upcoming dependencies conducts to social inequalities and conflicts for access to energy sources.

The only sustainable way to solve this challenge of increasing energy demand is to focus the effort on the development of renewable energy technologies. Solar energy takes a key role among renewable energy technologies. The amount of solar energy received on earth represent an inexhaustible source of energy for mankind. So far, Solar Thermal Power Plants (STTP) represent a quite small part of worldwide energy supply, but its percentage is increasing at a steady pace.

In 2011, 1.3 GW of concentrating solar power (CSP) were operational worldwide . The biggest operational STPP capacities are based in the USA (479 MW in 2011) and Spain (850 MW). The planned capacities amount to 31.7 GW. STPP are not only planned in the traditional operating countries, but also in the region of Middle East and North Africa (MENA) as well as Australia, India and China. This is only a tiny fraction of the available solar resource. Only in Europe it is estimated that the annual energy output potential of CSP is around 1800 TWh, which represents half of Europe present energy consumption. This report deals with parabolic trough power plants, which represent today the most significant proportion of installed STPPs. [EASAC, 2011]

An economical operation of parabolic trough power plants requires measurement techniques to evaluate and improve the efficiency of existing facilities and technical components. One main interest for the plant maintenance is the accurate measurement of the receiver tubes' thermal efficiency, which determines the solar field heat losses. Advance measurement techniques which are capable of detecting deficient receiver tubes could help increasing the economic viability of a STPP. State of the art heat loss measurement methods based on steady-state infrared thermography deliver field diagnostics which accuracy is significantly affected by varying ambient conditions, such

as ambient temperature, wind speed and direction [Price et al., 2006]. The development of a transient infrared thermography method to determine receiver heat losses is investigated by the German Aerospace Center (DLR), to face the challenge of a high precision operating receiver thermal qualification [Roeger et al., 2014].

The aim of that new measurement method is the identification of the receiver heat loss mechanisms in order to provide information about the origin of potential receiver degradation in the field.

The Qualification of **Pa**rabolic Trough **Re**ceivers in the **So**lar Field (Pareso) Project consists of six work packages. Initially, in the work package "Theoretical Base and Method Development", a numerical heat transfer model was extended as well as validated for steady-state conditions [Potzel, 2009]. For the analysis of the dynamic glass temperature course and for the derivation of the receiver thermal properties, algorithms were developed in [Geller, 2012].

During the second work package, "Laboratory preparation and acquisition of receiver tubes", a laboratory test bench was built at the Plataforma Solar de Almería (Spain). Several PTR samples with different thermal properties were produced in cooperation with an industrial partner. First measurements were done under laboratory conditions during the third work package "Laboratory Measurements" in [Gaertner, 2013].

This report focuses on the next work package "Field Measurements". The measurement method is implement under field conditions for the first time. The practicability of the method is investigated in the field. Potential difficulties have to be explored in order to optimize the measurement method.

1.2 Scope

This thesis report describes the development and optimization of the transient thermography method under field conditions. This method was so far only tested under laboratory conditions. Technical issues arising during this work as well as corrective measures are described and discussed.

The second chapter gives the background on the parabolic trough collector technology, which is commonly used in thermal solar power plants. The main focus is on the parabolic trough receiver. Its construction is explained and its heat loss mechanisms are described. Principles of steady-state heat loss measurement are explained.

In the third chapter, the transient measurement method for heat loss determination of parabolic trough receivers is introduced. First, an overview of infrared thermography technology is given. This technology is used to measure the outer absorber tube and outer glass envelope temperature. Secondly, the chapter includes an overview about the transient measurement principle. The radiation shield, which is a principal component of the experimental setup, is presented. Finally, a

description of the absorber temperature excitation is given, which is essential for the experimental approach.

The fourth chapter presents the experimental setup. It describes the deployed equipment and the different settings used during this work. In the fifth chapter, the operating procedure as well as the data analysis is introduced. In the sixth chapter, the measurement results are presented and discussed. The developments, emerging difficulties and proposed solutions are also described in this chapter. In the seventh chapter the progressed development and results of the measurement method are assessed and recommendations for future measurement tasks are discussed.

2 Background

2.1 Parabolic Trough Power Plants

High energy densities and temperature levels can be achieved by concentrating solar radiation with mirrors on a target. A solar concentrating system can only take advantage of Direct Normal Irradiance (DNI), which corresponds to the solar radiation that comes in a direct line from the sun and is neither absorbed nor scattered by the earth atmosphere.

A concentrating solar thermal collector application can be subdivided into a concentrating system on the one hand and the solar receiver on the other hand. A concentrating system is an optical system consisting of several mirrors, which track the sun path to concentrate DNI (or beam radiation) on a receiver, where the solar energy is converted in thermal energy and from where the thermal energy is transmitted to a power block for electricity generation. A solar thermal power plant can be realized with different solar radiation concentrating configurations. Among CSP technologies, one can distinguish between point-focusing configurations and line-focusing configurations.

Point-focusing configurations track the sun along two axes and focus beam radiation on a circular target, while line-focusing configurations track the sun along one axis and focus beam radiation on a linear target. Most common point-focusing systems are Solar Tower Systems. The collectors are large flat mirrors, called heliostats. Each heliostat tracks the sun biaxially and concentrates the DNI on a fixed receiver, which is located at the top of a tower. Another point-focusing configuration is the parabolic dish. The collector has the shape of a circular paraboloid and concentrates the DNI on the receiver, which is positioned in the focal point of the dish. The most popular solar field configuration among existing solar thermal power plants is a line-focusing configuration consisting of Parabolic Trough Collectors (PTC).

A PTC consists of parabolic mirrors assembled in a trough configuration. These mirrors concentrate the DNI onto a line of receivers, identified as Parabolic Trough Receivers (PTR), which are positioned in the focal line of the parabola. The parabolic trough configuration currently provides the best compromise between thermal efficiency and levelized cost of electricity [EASAC, 2011]. Fig. 2.1 (a) shows a parabolic trough collector row, Fig. 2.1 (b) shows an overview of a solar field including the power block.

PTC rows are usually lined up along a North-South axis. The PTC support structure is mounted on a single axis tracker, which rotates the collectors in order to concentrate DNI onto the receivers. The concentration factor for parabolic trough collectors lays between 80 and 100 [Winter et al., 1991]. Several PTCs connected in line form a collector loop. Several loops form a solar field.

(a) Parabolic Trough Collector Loop (b) Solar field with power block unit

Figure 2.1: Andasol powerplant in the Spanish province of Granada [Gladen, 2009]

A heat transfer fluid (HTF) is pumped through the receiver line. The solar radiation, which is concentrated on PTRs, heats up the HTF by convection. Different HTF, such as synthetic thermal oils, molten salts or water/steam mixtures, can be selected. The heated HTF then flows to a heat exchanger, where the heat is exchanged to a secondary circuit. The collected heat is fed to a classical Clausius-Rankine thermodynamical cycle and a steam turbine converts this thermal energy to electrical energy.

An additional benefit of CSP in comparison to other renewable energy technologies is the option of large scale thermal storage. This allows the power station to operate when there is no sunlight, which extends the plant capacity factor and also improves its efficiency.

As the efficiency of a Clausius-Rankine cycle can be increased using higher fluid temperatures, systems using direct steam generation (DSG), generating steam in the receiver line directly up to a temperature of 500 °C at a pressure about 120 bar, are developed and will soon replace the nowadays common used synthetic thermal oils as HTF for the next generation of solar power plants using PTC. [Winter et al., 1991]

2.2 Parabolic Trough Receivers

2.2.1 Function and Construction

The receiver is a key element of any concentrating STTP. A large portion of the STTP capital cost and the thermal efficiency depend on the receiver, also called Heat Collector Element (HCE). Its function is to absorb as much solar irradiation as possible while losing as less heat as possible. The construction of a PTR is illustrated in Fig. 2.2.

A PTR consists of two concentric tubes. The inner tube is the absorber tube. This tube is made

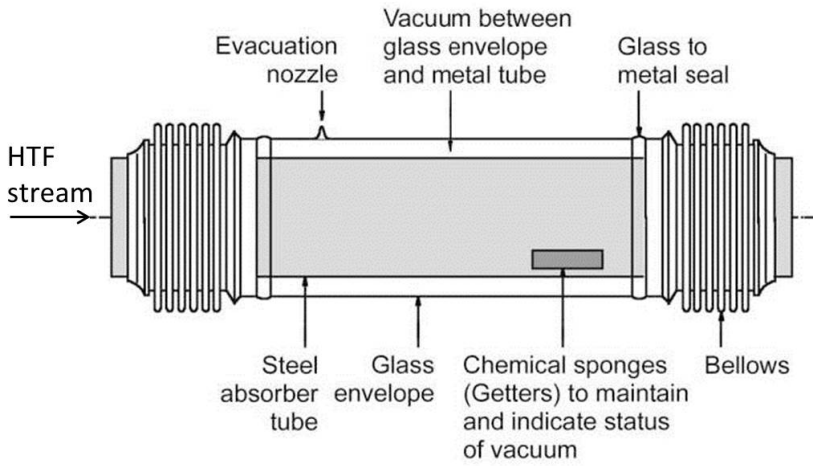

Figure 2.2: Scheme of a parabolic trough receiver [Burkholder & Kutscher, 2008]

of stainless steel. A selective coating is applied on its outer surface. The HTF is pumped through the absorber tube. The absorber tube is surrounded by a borosilicate glass envelope. Borosilicate glass is characterized by a low thermal expansion coefficient. An anti-reflective coating is applied on the inner and outer surfaces of the glass envelope.

As a first rough approximation, radiation can be subdivided in two wavelength ranges:

- ▹ short-wave radiation (0.3 to 2.5 µm)
- ▹ long-wave radiation (>2.5 µm)

Terrestrial solar radiation is classified as short-wave radiation. Thermal radiation is classified typically as long-wave radiation. Fig. 2.3 illustrates the spectrum of solar radiation (blue line) and the spectrum of a blackbody at 450 °C emitting thermal radiation (red line), which is higher than the typical mean operating temperature of 350 °C for a thermal oil HTF. The absorptance/emittance curve of the selective coating applied on the absorber surface is shown by the green line. It can be seen that it absorbs a maximum amount of solar radiation, while it emits a minimum of thermal radiation in the infrared spectrum. A small wavelength band remains in which both spectra overlap. With higher absorber temperatures, the radiation spectrum shifts towards smaller wavelengths and the overlap increases, which reduces the performance of the selective coating (look Subsection 3.1.1, Fig. 3.1). [Duffie & Beckman, 2006]

The annulus ring between the absorber tube and the glass envelope is evacuated. This reduces significantly convective heat losses to the ambient and prevents a potential oxidation of the selective coating. To monitor the annulus evacuation, vacuum indicators are placed in the annulus. They give a qualitative indication about the vacuum quality.

In addition, recent PTR constructions include a capsule filled with noble gas in the annulus to

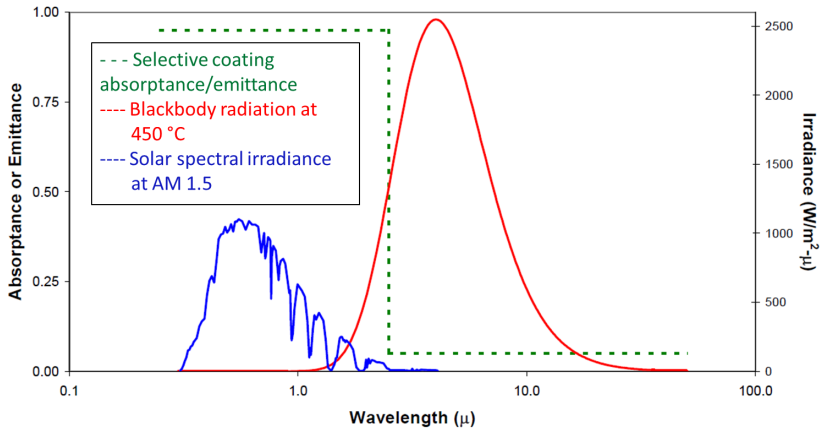

Figure 2.3: Illustration of the selective coating concept [Kennedy, 2002]

maintain a low thermal conductive gas mixture in the vacuum. The noble gas neutralizes gas particles with high thermal conductivity, such as hydrogen.

The absorber tube and the glass envelope are connected on each ends with vacuum tight bellows. These bellows compensate for the different thermal expansion of steel and glass.

2.2.2 Receiver Heat Loss Balance

The usable receiver power is the heat which is transferred by convection from the absorber tube to the HTF. The HTF heats up and a temperature difference builds up between the absorber inlet and outlet (Eq. 2.1) [Duffie & Beckman, 2006].

$$P_{th,useful} = \dot{m}_{HTF} \cdot c_{p,HTF} \cdot (T_o - T_i) \tag{2.1}$$

where:	$P_{th,useful}$	=	useful thermal power transferred to the HTF [W]
	$\dot{m}$	=	HTF mass flow [kg/s]
	$c_{p,HTF}$	=	HTF heat capacity [J/(kg·K)]
	T_o, T_i	=	HTF outlet / inlet temperature [K]

The PTR energy balance taking into account the incoming concentrated radiant flux and the collector optical efficiency are expressed in Eq. 2.2.

$$P_{th,useful} = P_{coll} \cdot \eta_0 - P_{th,loss} \tag{2.2}$$

where:	P_{coll}	=	concentrated radiant flux focused on the PTR [W]
	η_0	=	PTC optical efficiency [-]
	$P_{th,loss}$	=	PTR overall heat loss [W]

The optical efficiency η_0 includes factors such as [Duffie & Beckman, 2006]:

- ▷ collector intercept factor,
- ▷ incidence angle modifier,
- ▷ collector geometrical accuracy,
- ▷ mirror reflectance,
- ▷ glass envelope transmittance and
- ▷ soiling / cleanliness.

Within an operating PTR, all three heat transfer mechanisms occur:

- ▷ thermal conduction,
- ▷ thermal convection and
- ▷ thermal radiation.

Heat conduction occurs through the absorber wall and the glass envelope as well as through the bellows, if they are not insulated. Convective heat transfer takes part between the inner absorber tube surface and the HTF, inside the annulus between the outer absorber tube surface and the inner glass envelope surface as well as from the outer glass surface to the ambient. By radiation heat transfer, heat travels between the outer absorber tube surface and inner glass cover surface as well as from the outer glass surface to the sky respectively other surfaces in the ambient, the ground or collector mirrors. The heat transfer equations describing these mechanism are outlined in Section 2.2.3.

Fig. 2.4 shows schematically a radial PTR cross-section including all heat flows withing the receiver and the heat exchange to the ambient. Only radial directed heat flows are taken to account. Incoming irradiance is regarded as a heat flow. The glass envelope is assumed to be opaque for thermal infrared radiation. Bellow heat losses are not illustrated in this figure.

The largest percentage of the effective incoming solar radiant energy is absorbed by the selective coating on the absorber surface. Besides, a small fraction is absorbed by the glass envelope, which is assumed to be 0.02 % of the total incoming solar radiant power and therefore can be neglected

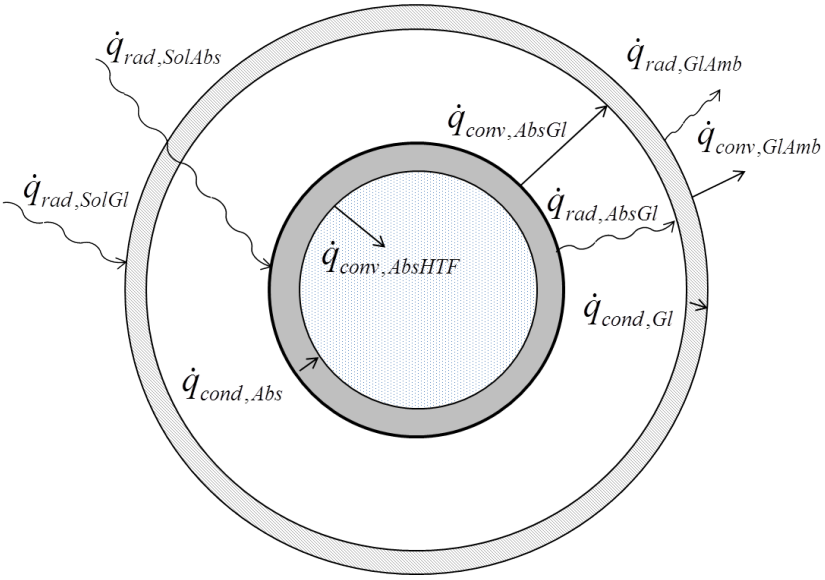

Figure 2.4: One-dimensional steady-state energy balance on a PTR radial cross-section [Forristall, 2003]; cond: conduction, conv: convection, rad: radiation, SolAbs: incident solar irradiation on absorber, SolGl: incident solar irradiation on glass, AbsHTF: from absorber to HTF, Abs: through absorber, AbsGl: from absorber to glass, Gl: through glass, GlAmb: from glass to ambient

[Forristall, 2003]. The heat is conducted through the absorber tube wall and transferred from the inner absorber tube surface to the HTF by forced convection.

The receiver heat losses depend on the absorber temperature as well as on the ambient conditions. The temperature differences between the absorber tube and the glass envelope, respectively between the glass envelope and the ambient, are driving heat loss mechanisms.

The annulus heat transfer mechanism induced by gas filling depends strongly on the gas pressure. In case of a high vacuum quality, gas thermal conduction is the main heat transfer mechanism and there is no natural convection. At higher annulus pressures, the natural convection becomes the main heat transfer mechanism. The interested reader is referred to [Ratzel et al., 1979] for more information on annulus heat transfer mechanism induced by gas fillings. In this work, both heat transport mechanisms, natural convection and thermal gas conduction, are later identified without specific distinction as convection heat flow inside the annulus.

A thermal radiation heat flow results from the temperature difference between the absorber surface and the facing glass surface, each one in fourth power. The glass envelope is considered to be opaque to thermal radiation. Consequently no direct radiation heat transfer occurs between the absorber surface and the ambient. With this assumption the receiver heat loss is completely transferred from the annulus to the ambient by heat conduction through the glass material (Eq. 2.5). [Forristall, 2003]

From the outer glass surface to the ambient the heat exchange occurs by convection and thermal radiation. The convection can be either natural or forced, depending on the wind speed. Thermal radiation depends on the ambient conditions, such as the sky, earth and mirror temperatures, depending on the orientation on the glass envelope.

For the PTR heat loss balance outlined in Eq. 2.3, 2.4 and 2.5, the incoming solar irradiance is not included. The absorber tube is heated up at a temperature higher than the ambient. This is the initial point of the heat losses. To fulfill the conservation of energy, all heat flows trough the different parts of the PTC must be equal. That means the heat flow from the outer absorber surface to the inner glass surface, the heat flow through the glass envelope wall as well as the heat flows from the outer glass surface to the ambient must be equal as expressed in Eq. 2.3, 2.4 and 2.5. All heat flows are normalized by the receiver length and expressed in W/m.

$$\dot{q}'_{rad,AbsGl} + \dot{q}'_{conv,AbsGl} = \dot{q}'_{cond,Gl} \tag{2.3}$$

$$\dot{q}'_{cond,Gl} = \dot{q}'_{rad,GlAmb} + \dot{q}'_{conv,GlAmb} \tag{2.4}$$

$$\dot{q}'_{rad,GlAmb} + \dot{q}'_{conv,GlAmb} = \dot{q}'_{loss} \tag{2.5}$$

where:

$\dot{q}'_{rad,AbsGl}$	=	thermal radiation heat flow from the outer absorber surface to the inner glass surface [W/m]
$\dot{q}'_{conv,AbsGl}$	=	heat exchange from the outer absorber surface to the inner glass surface by annulus convection [W/m]
$\dot{q}'_{cond,Gl}$	=	conductive heat flow through the glass envelope [W/m]
$\dot{q}'_{rad,GlAmb}$	=	thermal radiation heat flow between the outer glass surface and ambient [W/m]
$\dot{q}'_{conv,GlAmb}$	=	convective heat flow between the outer glass surface and ambient [W/m]
$\dot{q}'_{loss}$	=	PTR specific heat loss by unit length [W/m]

The processes of aging or degradation of some receiver properties leads to an increasing heat loss. Primarily, theses processes are the degradation of the absorber coating surface and a gas build-up within the annulus.

The degradation of the vacuum can be caused by the diffusion of gas molecules either through the glass envelope or through the absorber tube. Hydrogen can permeate through the steel tube by decomposition of the synthetic thermal oil. When the vacuum getters become saturated, the hydrogen pressure in the annulus will increase up to the partial pressure of hydrogen in the used HTF. Another vacuum degradation mechanism is the migration of helium through the glass envelope. If the glass envelope is broken or cracks arise, the annulus is filled with air at atmospheric pressure.

These mechanisms increase the convective part of heat exchange within the annulus and thus the specific heat loss. [Harding et al., 1985], [Price et al., 2006]

Besides the temperature difference in fourth power, the intensity of the radiation heat flow depends on the emissivity of the absorber and glass surfaces (Eq. 2.7). The glass envelope emissivity is regarded to be constant, whereas the emissivity of the selective coating on the absorber tube can degrade over the PTR lifetime. The higher the emissivity of the selective coating increases, the higher the radiation heat flow becomes.

The convective heat flow between the outer glass surface and ambient as well as the thermal radiation heat flow, which both combine the PTR heat loss (Eq. 2.4), depend strongly on the ambient air condition. The lower the estimated sky temperature, the higher the part of thermal radiation heat flow. The higher the wind speed and the lower the ambient temperature, the higher the convective part of the heat loss. [Price et al., 2006]

2.2.3 Heat Transfer Equations

The conduction heat transfer through the hollow cylinders of the absorber tube wall can be described by Fourier's law (Eq. 2.6).

$$\dot{q}'_{cond,abs} = \frac{2\pi \cdot k_{abs} \cdot \left(T_{abs,i} - T_{abs,o}\right)}{ln\left(\frac{r_{abs,o}}{r_{abs,i}}\right)} \tag{2.6}$$

where:	k_{abs}	=	absorber thermal conductivity at the average absorber temperature [W/(m ·K)]
	$T_{abs,i}$	=	absorber inner surface temperature [°C]
	$T_{abs,o}$	=	absorber outer surface temperature [°C]
	$r_{abs,i}$	=	inner radius of the absorber tube [m]
	$r_{abs,o}$	=	outer radius of the absorber tube [m]

The radiation heat flow between the inner glass surface and the outer absorber surface can be expressed with the equation of the radiation heat exchange between two concentric cylinder (Eq. 2.7).

$$\dot{q}'_{rad,AbsGl} = \frac{2\pi \cdot \epsilon_{abs} \cdot \epsilon_{gl} \cdot \sigma}{\epsilon_{gl} + \epsilon_{abs} \cdot \left(1 - \epsilon_{gl}\right) \cdot \frac{r_{abs,o}}{r_{gl,i}}} \cdot \left(T^4_{abs,o} - T^4_{gl,i}\right) \tag{2.7}$$

where:	σ_B	=	Stefan-Boltzmann constant [W/(m^2 ·K^4)]
	ϵ_{gl}	=	emissivity of the glass envelope surface [-]
	ϵ_{abs}	=	emissivity of the absorber tube surface [-]
	$r_{abs,o}$	=	outer radius of the absorber tube [m]

$r_{abs,i}$	=	inner radius of the glass envelope [m]
$T_{abs,o}$	=	temperature of the outer absorber surface [K]
$T_{gl,i}$	=	temperature of the inner glass surface [K]

The natural convection and thermal gas conduction between these surfaces can be combined into one equation. Thereby the heat flow can be described by Eq. 2.8, where h_{ann} is the annulus heat transfer coefficient. Which one of both heat transfer mechanisms occurs depend strongly on the quality of the vacuum, that means the annulus pressure, and the gas mixture.

$$\dot{q}'_{conv,AbsGl} = h_{ann} \cdot \pi \cdot r_{abs,o} \cdot \left(T_{abs,o} - T_{gl,i}\right) \tag{2.8}$$

where:	h_{ann}	=	heat transfer coefficient [W/(m^2·K)]

The thermal heat loss of the receiver is directly related to the glass temperature. Using the assumption that the glass envelope is opaque to thermal radiation, a direct radiation heat loss between the absorber tube and the ambient cannot occur. The conductive heat flow $\dot{q}'_{cond,Gl}$ can be described by the Fourier's law (Eq. 2.9). It can be assumed that the anti-reflective coating on the glass surfaces does not introduce a thermal resistance [Forristall, 2003]. It can occur, that the glass envelope is not fully opaque for some wavelength bands. Alternative heat loss models take this effect into account [Good, 2011]. This effect is neglected in further approaches.

$$\dot{q}'_{cond,abs} = \frac{2\pi \cdot k_{gl} \cdot \left(T_{gl,i} - T_{gl,o}\right)}{ln\left(\frac{r_{gl,o}}{r_{gl,i}}\right)} \tag{2.9}$$

where:	k_{gl}	=	absorber thermal conductivity at the average glass temperature [W/(m·K)]
	$T_{gl,i}$	=	glass inner surface temperature [°C]
	$T_{gl,o}$	=	glass outer surface temperature [°C]
	$r_{gl,i}$	=	inner radius of the glass envelope [m]
	$r_{gl,o}$	=	outer radius of the glass envelope [m]

The heat transfer from the glass envelope is described by Eq. 2.10.

$$\dot{q}'_{conv,GlAmb} = h_{amb} \cdot \pi \cdot r_{gl,o} \cdot \left(T_{gl,o} - T_{amb}\right) \tag{2.10}$$

where:	h_{amb}	=	convective heat transfer coefficient between outer glass surface and ambient [W/(m^2·K)]
	T_{amb}	=	ambient temperature [°C]

The convection heat transfer coefficient depends on the Nusselt number, which has to be calculated whether the convection heat transfer is natural or forced. It depends on the wind speed and wind direction, weather the wind direction is perpendicular or parallel to the receiver longitudinal axis. [Incropera et al., 2006]

$$h_{amb} = \frac{k_{air}}{r_{gl,o}} \cdot Nu_{amb} \tag{2.11}$$

where:	k_{air}	=	convection heat transfer coefficient for air [W/(m·K)]
	Nu_{amb}	=	Nusselt number [-]

The radiation transfer from the glass envelope to ambient, such as sky or surrounding objects, is caused by the upcoming temperature differences. If only the sky is taken in account, the envelope is regarded as a grey body, which is positioned in a blackbody cavity with infinitely large radius in comparison to the envelope, which represents the sky [Duffie & Beckman, 2006].

$$\dot{q}'_{rad,GlAmb} = \sigma_B \cdot r_{gl,o} \cdot \pi \cdot \epsilon_{gl} \cdot \left(T^4_{gl,o} - T^4_{sky}\right) \tag{2.12}$$

where:	$r_{gl,o}$	=	outer radius of the glass envelope [W/(K·m)]
	$T_{gl,o}$	=	temperature of the outer glass surface [K]
	T_{sky}	=	sky temperature [K]

Finally, the thermal quality of a PTR can be normalized by the temperature difference between the absorber and the glass temperature. This expression is called UA_L characteristic or UA_L value. [Potzel, 2009]

$$UA_L = \frac{\dot{q}'_{loss}}{\left(T_{abs,o} - T_{glass,o}\right)} \tag{2.13}$$

where:	UA_L	=	on PTR length normalized heat losses [W/(K·m)]

2.2.4 Steady-State Heat Loss Measurement Techniques

Today two practicable measurements are available to measure PTR heat losses. Both principles are applied for a steady-state absorber temperature.

The first heat loss measurement technique is a laboratory measurement. One approach used by National Renewable Energy Laboratory (NREL) is presented in [Burkholder & Kutscher, 2008]. The PTR is heated up by Joule heating, using four coil heaters and two cartridge heaters. These heaters

are placed in a copper tube, which evens the heat inside of the absorber tube. The cartridge heaters are used to heat up the inside of the absorber tube. At each end of the HCE two coil heaters are positioned. These coil heaters compensate end losses and create an adiabatic barrier. This is done to simulate the PTR operating installed in a PTC. A schematic of the experimental setup is illustrated in Fig. 2.5.

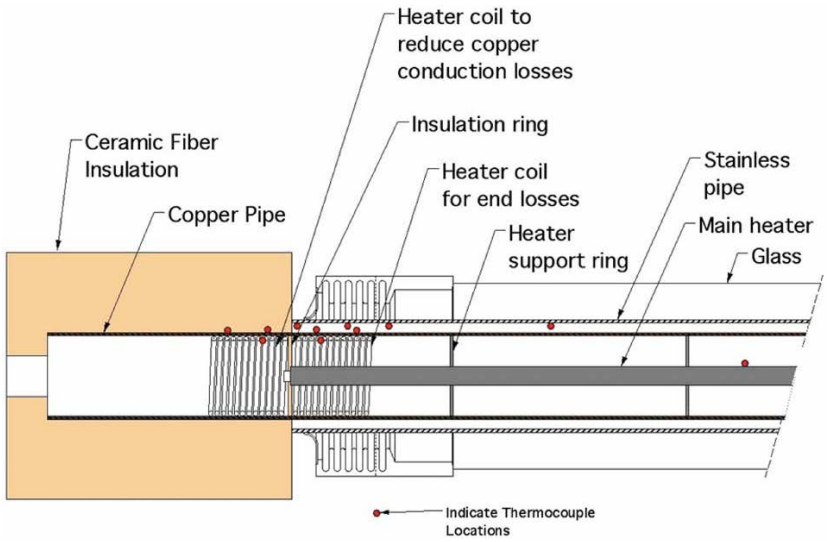

Figure 2.5: Thermal receiver test bench [Luepfert et al., 2008]

When the system is in steady-state, the electrical power input is equal to the PTR overall heat loss. The steady-state power can be varied to measure the PTR heat loss at different absorber temperatures in order to derive a heat loss correlation. [Burkholder & Kutscher, 2008]

An analog measurement technique is applied by DLR [Luepfert et al., 2008]. To compare both laboratory measurement approaches, a round-robin test campaign was carried out [Dreyer et al., 2010], involving DLR and NREL as independent investigation institutes and Schott Solar GmbH as a PTR manufacturer. The round-robin experiments showed that the different laboratory test benches agreed within ± 10 W/m for the measurement of PTR heat losses.

The advantage of laboratory test benches is the low uncertainty and the high reproducibility of measurements. A disadvantage is that the correlations are valid for stable ambient conditions, that means a constant ambient temperature and no wind. Furthermore, this method can only be used for dismounted receivers and is not a field measurement technique that can be applied to measure PTR heat losses in operating power plants.

A second measurement method for PTR heat losses designed for field investigation is presented in [Price et al., 2006]. With that method, an infrared camera is utilized to evaluate thermal heat losses by measuring the glass temperature and a developed numerical PTR heat transfer model is used [Forristall, 2003]. This model allows to evaluate the thermal performance of PTR and calculate the glass temperature. A fast and efficient glass temperature measuring method is developed

by using a mobile solar blind infrared camera. That means, the operating PTR can be investigated directly in the focusing PTC. A 50 MW plant can be surveyed within two days with this measurement technique. For evaluating the PTC, the measured glass temperature is compared with the numeric model simulated temperatures. By this, the PTR performance can be estimated. Evaluated glass temperatures indicate PTC aging and degradation, such as increased annulus pressure either caused by air penetration or by a hydrogen build-up.

Compared with laboratory test methods, the PTR heat loss is not measured by this method directly. This method contains apart from measurement uncertainties a second source of errors, namely numerical approximations. Furthermore, unsteady conditions of the ambient brings significant uncertainties. The wind direction and wind speed are not measured directly on the PTR surfaces and influences cannot be taken into account with the numerical model. One other ambient influence is the sky temperature variability, which is also not taken into account and brings an uncertainty regarding the radiation heat loss. The heat loss measurement technique can be only performed under stable ambient conditions, for example during the absence of wind. This leads to a questioning of the practicability of this field measurement method for accurate heat loss measurements.

Both heat loss measurement techniques only display the heat loss in one certain point of ambient conditions. The PTR thermal properties are not determined by these methods and by that, the origin of the heat loss is not determined. A prediction on the heat loss concerning other ambient conditions such as wind, ambient temperature and sky temperature can not be derived. [Potzel, 2009] apportions an uncertainty of 20 % on the UA_L characteristic caused by variant ambient condition for steady-state methods. This uncertainty increases specially with a higher uncertainty of the wind velocity.

3 Transient Infrared Thermography Heat Loss Measurement Methodology

3.1 Transient Infrared Thermography Measurement Principle

3.1.1 Infrared Thermography

The PTR absorber temperature, which is necessary to be measured in the following presented heat loss measurement methodology, cannot be measured by contact. The inner absorber surface is in contact with the HTF. The outer surface is surrounded by the glass envelope. Therefore, the absorber surfaces as well as the glass envelope surface temperatures will be measured by infrared thermography. This subsection introduces key concepts relevant for infrared technology.

Any body with a temperature higher than 0 K emits thermal radiation. A body's temperature can be measured by the intensity of this radiance, because it is directly correlated to its surface temperature. The advantage of infrared thermography in contrast to other temperature measurement methods is the absence of contact between the body and the measurement instrument. Surfaces which are difficult to access can be measured. Furthermore, infrared thermography shows a much higher dynamic of measurement compared to PT100 or thermocouple sensors. This is important for transient measurements, where dynamic responses are analyzed.

Among thermal radiators, the blackbody is of particular importance. It is defined in such way, that its radiant emittance does not depend on the material properties of the surface but only on the body temperature. The idealized blackbody absorbs and emits all thermal radiation at all wavelengths. This behavior is described by Planck's Law of Blackbody Radiation in Eq. 3.1. The radiant emittance is characterized by a wide wavelength range. Planck's law describes the intensity of a single wavelength. [Pfaender, 2006]

$$L_{\lambda,b}(T) = \frac{c_1}{\lambda^5} \cdot \frac{1}{exp\left(c_2/\left(\lambda \cdot T_b\right)\right) - 1} \cdot \frac{1}{\Omega_0} \tag{3.1}$$

where:	$L_{\lambda,b}$	=	spectral radiance [W/(sr $\cdot$m$^2\cdot$µm)]
	c_1;c_2	=	first and second radiation constants [W$\cdot$m^2], [m$\cdot$K]
	λ	=	considered wavelength [µm]
	T_b	=	blackbody temperature [K]
	Ω_0	=	solid angle of hemisphere [sr]

The wavelength distribution of the spectral radiance has a distinct maximum at a certain wavelength for each temperature. The position of that maximum shifts towards a shorter wavelength, as the temperature increases. Its position is expressed out by the Wien's Displacement Law (Eq. 3.2).

$$\lambda_{max} \cdot T_b = 2898\ \mu m \cdot K = constant \tag{3.2}$$

where:	λ_{max}	=	wavelength of maximum spectral radiance [µm]
	T_b	=	blackbody temperature [K]

Fig. 3.1 provides a graphical overview of Planck's and Wien's laws as a function of temperature and wavelength. The straight proportional dependency of the radiance peak temperature on the temperature is figured as a line.

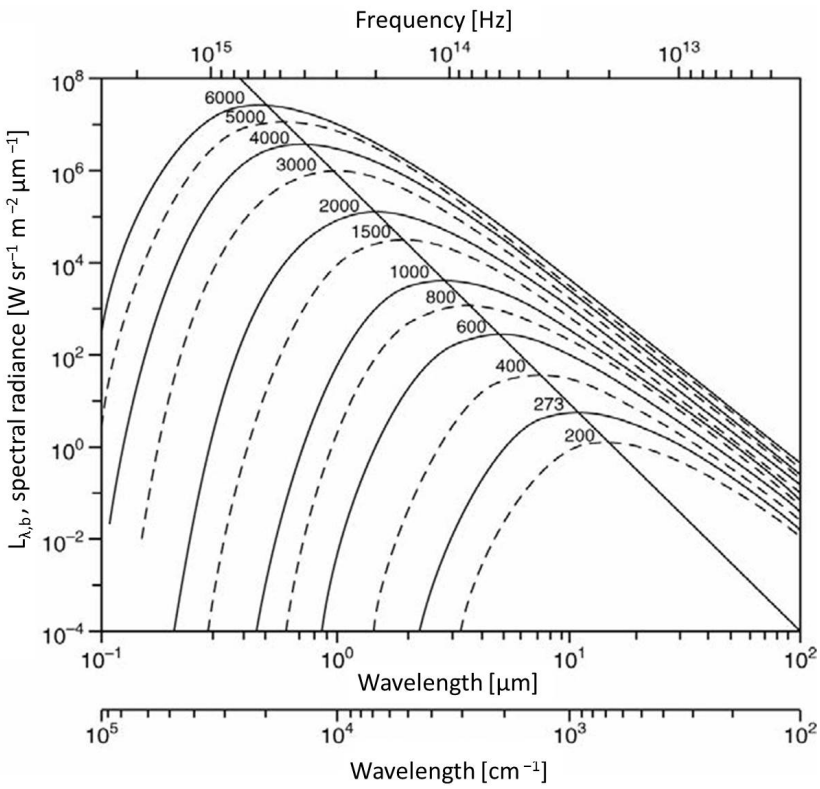

Figure 3.1: Spectral distribution of blackbody radiance [Pfaender, 2006]

The integration of the spectral radiance $L_{\lambda,b}$ expressed by Planck's law over the hemispherical solid angle of the ideal emitting blackbody leads to the blackbody spectral radiant emittance $M_{b,\lambda}$. A further integration over all wavelengths (λ = [0;∞]) leads to the Stefan-Boltzmann-Law (Eq. 3.3). It describes the radiant emittance M_b, which is proportional to the fourth power of the blackbody temperature.

$$M_b(T) = \sigma_B \cdot T_b^4 \tag{3.3}$$

where: $M_b(T)$ = radiant emittance [W/m^2]
σ_b = Stefan-Boltzmann constant [W/(m$^2 \cdot$K^4)]

The physical laws described so far refer to an ideal blackbody. The Kirchhoff's law of thermal radiation links these physical laws to real radiators and reflects the knowledge of the blackbody spectral power distribution on the real body radiant emittance. It defines the spectral emissivity, which is the quotient of the spectral radiant emittance of a real body to the spectral radiant emittance of a blackbody with the same temperature at a certain wavelength (Eq. 3.4). According to Kirchhoff's law, a real object only emits a part of a blackbody radiance at the same temperature. All absorbed radiance by the body is emitted. The spectral emissivity $\epsilon_\lambda(T)$, respectively absorptivity $\alpha_\lambda(T)$ are dimensionless values, which generally depend on wavelength, temperature and solid angle.

$$\epsilon_\lambda(T) = \frac{L'_\lambda(T)}{L_\lambda(T)} = \alpha_\lambda(T) \tag{3.4}$$

where: $\epsilon_\lambda(T)$ = spectral emissivity coefficient [-]
$L'_\lambda(T)$ = spectral emitted radiance of the observed body [W/m^2]
$\alpha_\lambda(T)$ = spectral absorptivity [-]

If the spectral emissivity of a real body is independent of the wavelength, temperature and solid angle, the body represents a so-called grey body. Per definition, its emissivity is constant and lower than one for the complete range of wavelength.

Referring to the principle of the conversation of energy, the sum of the of the absorptivity (α), transmissivity (τ) and reflectivity (ρ) must be equal to 1 (Eq. 3.5) [Pfaender, 2006].

$$\alpha_\lambda + \tau_\lambda + \rho_\lambda = 1 \tag{3.5}$$

where: $\tau_\lambda(T)$ = spectral transmissivity [-]

Thermal radiation can be measured with infrared sensors, such as infrared pyrometers. Infrared pyrometer consists of three parts:

- the optical system,
- the detector and
- the analog-to-digital conversion module.

The optical unit images the incoming radiosity on the detector unit, which converts the analog radiometric signal in an analog electrical signal. Modern pyrometers include an analog-to-digital conversion unit. An ambient temperature compensation reduces the influence of the pyrometer's own temperature.

The pyrometer analog signal is a linear function of the measured temperature. The pyrometer current analog signal, logged in [mA], is converted into a temperature signal [°C] according to Eq. 3.6.

$$T_{pyr} = \left[\frac{i_{pyr} - i_{min}}{i_{max} - i_{min}} \cdot (T_{max} - T_{min}) \right] + T_{min} \tag{3.6}$$

where:	T_{pyr}	=	infrared pyrometer temperature signal [°C]
	i_{pyr}	=	analog pyrometer signal [mA]
	i_{min}, i_{max}	=	minimal/maximal current of measurement range [mA]
	T_{min}, T_{max}	=	minimal/maximal temperature of measurement range [°C]

The pyrometer is primarily chosen by its wavelength range along with its temperature range. Spectral band pyrometers evaluate the incoming radiation within a band of wavelengths. This is realized by using interference filters and appropriate detectors. The selection of the wavelength range should be based on the spectral properties of the measured surface, such as the spectral emissivity and spectral transmissivity. The material must be opaque in the selected wavelength range. Otherwise, transmissivity in the selected wavelength range allows the infrared sensor to look through the material and enables to measure the temperature of a body behind that opaque material. [IMPAC, 1999]

To measure the temperature within a certain band, the measured spectral radiant emittance is integrated over this certain wavelength band. Using the integrated radiant emittance and the emissivity, the temperature can be determined. For infrared thermography, relevant wavelength bands can be generally subdivided into [Meola and Carlomagno, 2004]

- ▹ near infrared (0.75 - 3 µm)
- ▹ middle infrared (3 - 6 µm)
- ▹ far infrared (6 - 15 µm).

The infrared pyrometer is chosen depending on the spectral properties of the material to be measured and its expected temperature range.

Therefore, the spectral properties of the investigated test object must be known. In the case of PTRs, the focus lies primarily on the measurement of the absorber tube and glass envelope outer surface temperatures. One task is the glass envelope temperature measurement. For this task, the

infrared pyrometer faces directly the glass envelope. As glass is a transparent material in a wide range of wavelengths, the pyrometer measure radiant emittance in a wavelength band for which the glass remains opaque. The second task is to measure the absorber temperature. Here, the infrared pyrometer needs to look trough the glass envelope. That means, the pyrometer wavelength band must be in a region, where the glass material shows a high transmissivity. According to the measurement method principle, described further in Section 3.1.2, neither the absorber nor the glass envelope are directly irradiated by the sun.

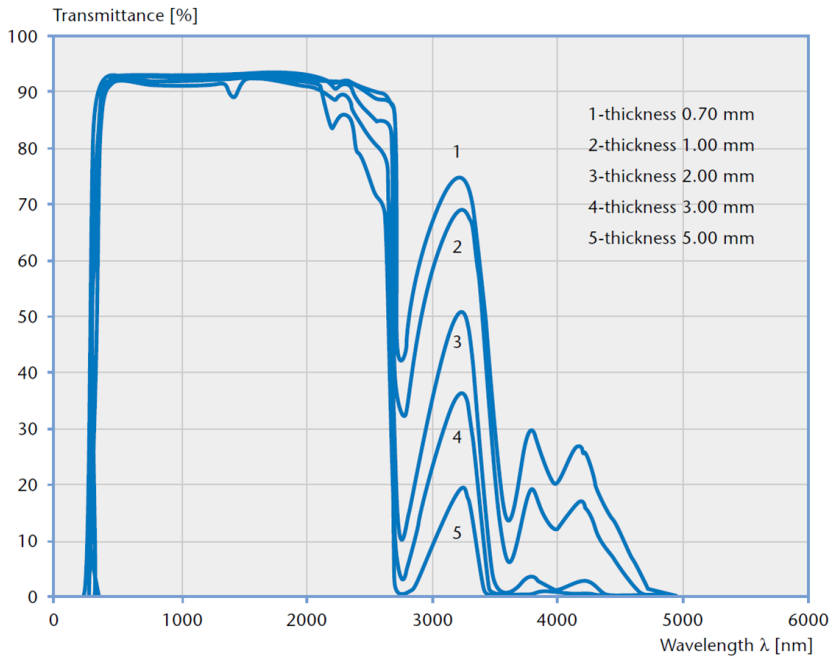

Figure 3.2: Transmissivity of borosilicate glass for different thicknesses (Borofloat® 33) [SCHOTT, 1999]

Fig. 3.2 illustrates the spectral transmissivity of borosilicate glass from 0 µm to 6 µm. Borosilicate transmissivity is high from approximately 0.3 µm to 2.7 µm and it decreases from 2.7 µm to 5 µm. For wavelengths above 5 µm, borosilicate glass can be considered as an opaque material. With the knowledge of the transmissivity and the reflectivity of the material, the emissivity of the material in the observed wavelength band can be derived according to Eq. 3.5. Thus, to measure the glass temperature, the appropriate range of wavelengths is above 4.5 µm for glass thicknesses up from 3 mm.

The emissivitiy of metal surfaces is high in the range of near infrared wavelength and decreases with increasing wavelength [IMPAC, 1999]. In any case, the optical property of the selective coating attached on the absorber surface has to be considered. As one can see in Fig. 2.3, the absorptivity respectively the emissivity of a selective coating should be high in the near infrared region up to 3 µm. Since the absorber tube is inserted within the glass envelope, the wavelength range of the infrared pyrometer measuring the absorber surface temperature is limited by the transmission

range of the glass cover, which shows a high transmissivity from 0.5 µm up to 2.7 µm.

In addition, the transmission of the atmosphere can be influence the infrared measurement as well. The measured radiation must pass through the atmosphere. The transmission of the air depends on its molecular composition. Water vapors as well as carbon dioxide absorption bands restrain certain atmospheric windows.

Available pyrometers for this project are built with wavelength band, which are not influenced by the atmosphere [IMPAC, 1999]. Furthermore, the infrared thermography application considered for PTR heat loss measurements is designed for small distances to the measurement object. The effect of atmospherical absorption can be neglected for short distances.

Based on this knowledge, broad bands pyrometers were chosen. During this work, the pyrometer *Pyrospot DT44LH* measures the glass envelope temperature in a wavelength band ranging from 8 µm to 14 µm. This is a suitable range for borosilicate glass based on spectral properties that is relevant for the considered temperature range (50 °C to 300 °C). The pyrometer *Pyrospot DGE 10N* measures the absorber tube temperature in a wavelength band ranging between from 2.0 µm to 2.6 µm. In this wavelength band, the absorber temperature can be measured through the borosilicate glass envelope because of its high transmissivity.

3.1.2 Measurement Principle

The principle of a transient infrared thermography method applied to PTR heat loss measurements is to investigate the dynamic glass temperature response for a given dynamic excitation of the absorber temperature. One example of an absorber temperature excitation and its corresponding glass temperature response can be seen in Fig. 3.3, where a sinusoidal excitation function is applied.

The aim is to separate between the internal heat loss mechanisms in PTR, presented in Subsection 2.2.2. That means, the emissivity ϵ_{abs} (Eq. 2.7) of the absorber coating and annulus heat transfer coefficient h_{ann} (Eq. 2.8) can be derived. Thus, the presented method delivers a more detailed knowledge for the PTR thermal properties in comparison to the methods outlined in Subsection 2.2.4. The exciting absorber surface temperature T_{abs}(t) and the responding outer glass surface temperature T_{gl}(t) are measured using infrared thermography, as described in Subsection 3.1.1.

To understand the transient measurement principle, one can start with the glass envelope dynamic heat balance, expressed in Eq. 3.7. One can see that the glass temperature variation dT_{gl}/dt depends on the inner and outer heat flows at the glass surface. These heat flows can be connected to the heat loss balance, presented in Subsection 2.2.2. $\dot{q}'_{gl,in}$ is the internal heat flow within the annulus, $\dot{q}'_{gl,out}$ is the external heat flow between the outer glass surface and the ambient. Both are the sum of a convective heat flow and a thermal radiation heat flow (Eq. 3.8 and Eq. 3.9).

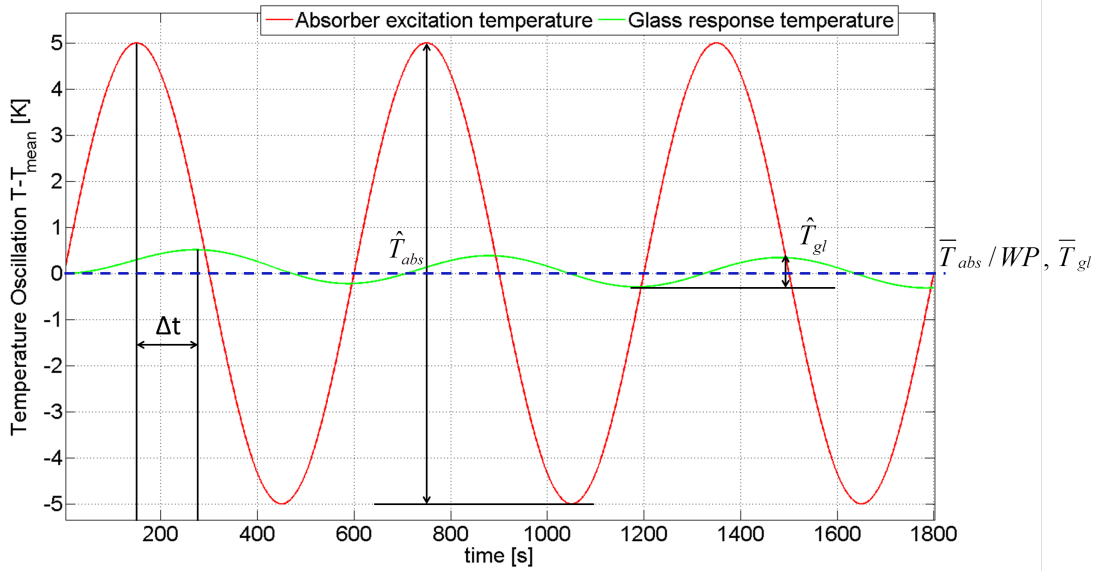

Figure 3.3: Exemplary temperature oscillation for a sinusoidal excitation function with an angular frequency of $\omega = 2\pi/600s$, an excitation amplitude of $\hat{T}_{abs} = 10$ K

$$\rho c_{p,gl} \frac{V_{gl}}{l_{PTR}} \frac{dT_{gl}}{dt} = \dot{q}'_{gl,i} + \dot{q}'_{gl,o} \tag{3.7}$$

$$\dot{q}'_{gl,i} = \dot{q}'_{conv,AbsGl} + \dot{q}'_{rad,AbsGl} \tag{3.8}$$

$$\dot{q}'_{gl,o} = \dot{q}'_{conv,GlAmb} + \dot{q}'_{rad,GlAmb} \tag{3.9}$$

where:

ρ	=	glass density [kg/m^3]
$c_{p,gl}$	=	glass specific heat capacity [J/(kg·K]
V_{gl}	=	glass volume [m^3]
l_{PTR}	=	PTR length [m]
$\dot{q}'_{gl,i}, \dot{q}'_{gl,o}$	=	specific heat flows at the inner and outer glass envelope surfaces [W/m^2]

The transient heat loss measurement method is based on the assumption, that the PTR thermal behavior can be characterized by a transfer function. This transfer function relates the glass temperature $T_{gl}(t)$, which represents the systems output signal, to the absorber temperature $T_{abs}(t)$, the input signal. Its response behavior depends on its thermal properties, as it is illustrated in Fig. 3.4 (a).

Applying a Laplace transform on both sides of the differential equation (Eq. 3.7), one can derive a frequency response F($j \cdot \omega$). The frequency response has the form of a first-order lag element, also called PT1 element (Eq. 3.10). The first-order lag element response signal on a step excitation is illustrated in Fig. 3.4 (b).

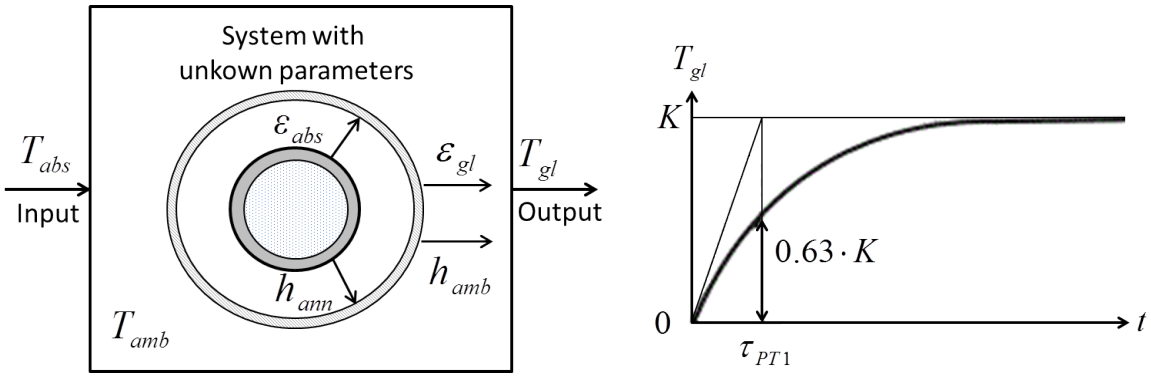

(a) The PTR as a black box, which glass temperature response depends on its thermal properties and ambient conditions

(b) A fist-order lag element step response profile with gain constant K and time constant τ_{PT1}

Figure 3.4: The PTR as a transfer function with the absorber temperature as input signal and the glass temperature signal as output function

The frequency response can be described by a bode diagram. The amplitude ratio A (Eq. 3.11) and the phase shift φ (Eq. 3.12) can be derived from this representation [Lunze, 2004]. These parameters can be derived out experimentally by analyzing the excited absorber temperature $T_{abs}(t)$ and the glass temperature response $T_{gl}(t)$.

$$F(\omega) = K \cdot \frac{1}{1 + j\omega \cdot \tau_{PT1}} \tag{3.10}$$

$$A(\omega) = \frac{K}{\sqrt{1 + \omega^2 \cdot \tau_{PT1}^2}} \tag{3.11}$$

$$\varphi(\omega) = -arctan(\omega \cdot \tau_{PT1}) \tag{3.12}$$

where:	K	=	gain constant [-]
	ω	=	angular frequency [rad/s]
	τ_{PT1}	=	time constant of first-order lag element [s]
	A	=	amplitude ratio [-]
	φ	=	phase shift [rad]

All in all, knowing the five values amplitude ratio A, phase shift φ, the mean absorber temperature $\overline{T}_{abs}$, mean glass temperature $\overline{T}_{gl}$ and the mean ambient temperature $\overline{T}_{amb}$ by experimental in-

vestigation on the one hand, knowing the geometrical quantities like the glass volume V_{gl} and the receiver length as well as the material properties like density ρ and specific heat capacity $c_{p,gl}$ on the other hand, one can derive the internal thermal properties ϵ_{abs} and h_{ann} of a PTR. The derivation process of a PTR specific heat loss for standard ambient conditions is outlined in Fig. 3.5.

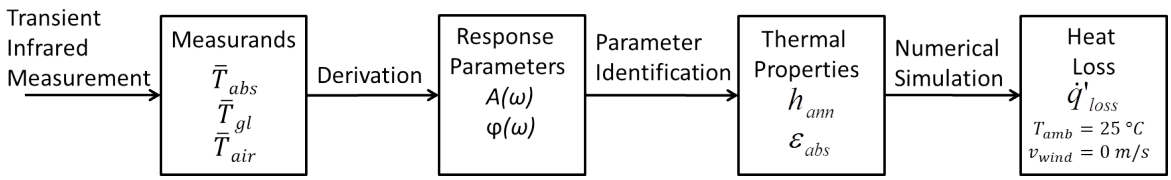

Figure 3.5: Process outline of a transient infrared thermography heat loss measurement

The identification of the PTR thermal properties ϵ_{abs} and h_{ann} is achieved by using a numerical heat transfer model in combination with a hybrid optimization algorithm. The optimization algorithm searches for the optimal combination for the parameters ϵ_{abs} and h_{ann} based on the set of experimental measurands absorber temperature T_{abs}, air temperature T_{amb} and air speed v_{air}, that best reproduces the experimental set of measurands $\left(A, \varphi, \overline{T}_{abs}, \overline{T}_{gl}, \overline{T}_{amb}\right)$ (Eq. 3.13 and 3.14).

$$\epsilon_{abs} = f\left(A, \varphi, \overline{T}_{abs}, \overline{T}_{gl}, \overline{T}_{amb}\right) \tag{3.13}$$

$$h_{ann} = f\left(A, \varphi, \overline{T}_{abs}, \overline{T}_{gl}, \overline{T}_{amb}\right) \tag{3.14}$$

The derivation of ϵ_{abs} and h_{ann} provides a diagnostic about the individual annulus heat loss mechanisms. With these receiver thermal properties, the specific heat loss $\dot{q}'_{loss}$ respectively the UA_L value can be simulated. This last simulation is done for standard laboratory conditions, that means an ambient temperature of 25 °C and a wind speed of 0 m/s.

The mean absorber temperature $\overline{T}_{Abs}$ defines the investigated working point (WP) and is defined before each test campaign. In this work two working points at 300 °C and 350 °C were investigated.

3.2 Radiation Shield

3.2.1 Radiation Shield Principle

A radiation shield surrounding the investigated part of the receiver is a main part of the transient heat loss measurement experimental setup. It reduces the radiation heat loss (Eq. 2.4) as a part of the outer heat flow at the glass surface. The inside of this shield is covered with an infrared reflecting foil. This foil reflects about 95 % of the thermal radiation emitted by the glass back to

itself [Roeger et al., 2014]. Therefore, the thermal radiation heat flow $\dot{q}'_{rad,GlAmb}$ between the glass and the ambient can be neglected. The external heat flow $\dot{q}'_{gl,o}$ reduces to the convective heat flow $\dot{q}'_{conv,GlAmb}$ between the glass envelope and the radiation shield. On one side of the radiation shield, a set of fans are mounted to bring in a steady air flow through the radiation shield in order to keep a constant forced convection regime and avoid a heat build-up. Apertures drilled in the radiation shield jacket allows the infrared thermography on the absorber tube and glass envelope surface. A sketch of the radiation shield design is shown in Fig. 3.6.

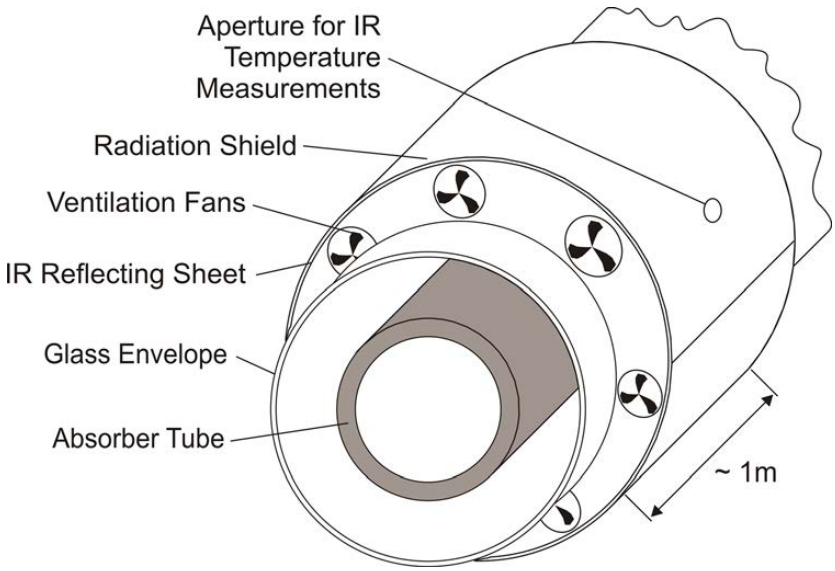

Figure 3.6: Radiation shield design [Roeger et al., 2014]

The air temperature within the radiation shield is higher than the ambient temperature. That means, not the ambient temperature influences the measured glass temperature in the middle of the radiation shield, but the actual air temperature. Therefore, the required measurand $\overline{T}_{Amb}$ changes to $\overline{T}_{Air}$ and has to be considered in the experimental set of measurands for the identification of the thermal properties (Eq. 3.15 and 3.16).

$$\epsilon_{abs} = f\left(A, \varphi, \overline{T}_{abs}, \overline{T}_{gl}, \overline{T}_{air}\right) \tag{3.15}$$

$$h_{ann} = f\left(A, \varphi, \overline{T}_{abs}, \overline{T}_{gl}, \overline{T}_{air}\right) \tag{3.16}$$

3.2.2 Radiation Shield Heat Balance

The radiation shield around the glass envelope modifies slightly the heat balance composing of the occurring heat flows. The heat flows illustrated in Fig. 2.4 are updated due to the introduction of the radiation shield according to Fig. 3.7.

As the investigated PTR is not irradiated by the sun and protected by the radiation shield, all heat flows within the PTR are part of the overall heat loss. In contrast to an irradiated PTR, where the initial point of heat loss is the heated outer absorber surface, within an unirradiated PTR the heat loss is driven by the heated up HTF and travels through the absorber wall, the annulus, the glass envelope wall to the ambient. The heat flows $\dot{q}'_{conv,AbsHTF}$, $\dot{q}'_{cond,abs}$ and $\dot{q}'_{cond,gl}$ turn around their direction. The heat loss balance presented in Section 2.2.2 is to be updated by these heat flows by Eq. 3.17 and Eq. 3.18.

$$\dot{q}'_{conv,AbsHTF} = \dot{q}'_{cond,Abs} \tag{3.17}$$

$$\dot{q}'_{cond,Abs} = \dot{q}'_{rad,AbsGl} + \dot{q}'_{conv,AbsGl} \tag{3.18}$$

The thermal radiation heat flow $\dot{q}'_{rad,GlAmb}$ is replaced by the thermal radiation between glass surface and inner shield surface $\dot{q}'_{rad,GlShield}$. That heat flow can be neglected as the infrared radiation is reflected by the inner face of the shield. The radiation shield is supposed to bring uncertainties depending on the derivation on wind speed, concerning the convective heat loss, and sky temperature, concerning the radiation heat loss in fourth power, to a minimum.

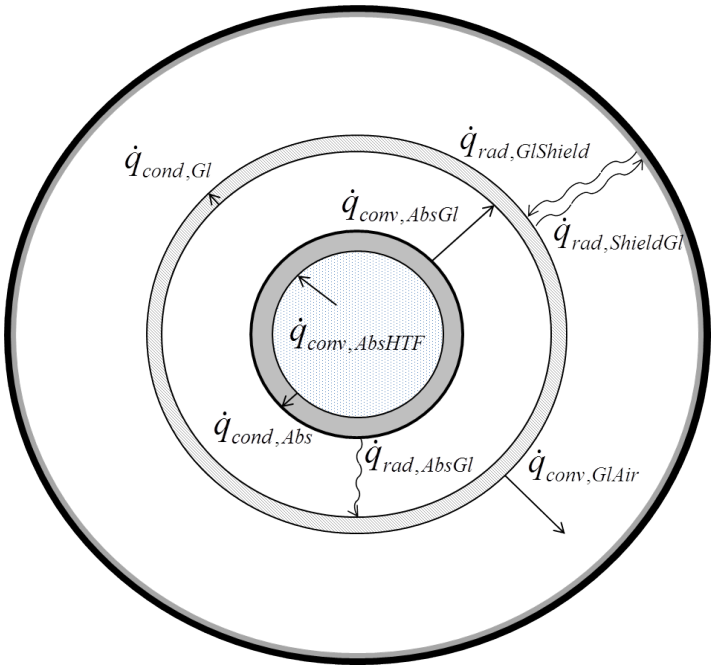

Figure 3.7: PTR heat flows within the radiation shield for transient infrared thermography heat loss measurement method

3.3 Absorber Temperature Excitation and Glass Temperature Response

3.3.1 Periodical Excitation

The principle of the transient heat loss measurement is based on the thermal excitation of the absorber tube temperature. Depending on the properties ϵ_{abs} and h_{ann} of the PTR, the glass temperature gives a certain response to that excitation. Any excitation function can be used, as long as the frequencies are in the magnitude of a proper response of the glass temperature, that it can be identified by common measurement devices. Investigated excitation functions include periodical excitation on the one hand, such as sinusoidal functions, and transient functions on the other hand, such as ramp-and-hold functions.

As the radiation heat flow depends on the fourth power of the temperatures (Eq. 2.7), the system shows a nonlinear response to the thermal excitation concerning the amplitude of the signal. Thus, the amplitude of the temperature variation around a defined working point should remain relatively small so that the observed response can be assumed to be linear.

If a sinusoidal excitation is applied on the absorber surface temperature, the response of the glass temperature follows as well a sinusoidal profile with the same period, but, as one can see in Fig. 3.3, by a lower amplitude than the absorber amplitude and a phase shift related to the excitation function. The mean temperature of the temperature oscillations is the mean absorber temperature $\overline{T}_{abs}$ respectively the working point and the mean glass temperature $\overline{T}_{gl}$ A mathematical description for both temperature profiles is given with Eq. 3.19 and Eq. 3.20. Both values can be derived by graphical analysis of the temperature profiles, like it is demonstrated in Fig. 3.3.

$$T_{abs}(t) = \overline{T}_{abs} + \hat{T}_{abs} \cdot e^{j(2\pi/t_{period})t} \tag{3.19}$$

$$T_{gl}(t) = \overline{T}_{gl} + \hat{T}_{gl} \cdot e^{j(2\pi/t_{period})t+\varphi} \tag{3.20}$$

where:

$\overline{T}_{abs}, \overline{T}_{gl}$	=	mean absorber respectively glass temperature [°C]
$\hat{T}_{gl}$, $\hat{T}_{gl}$	=	absorber respectively glass temperature amplitude [°C]
t_{period}	=	period of sinusoidal excitation [s]

For periodical excitations, the amplitude ratio is the quotient of the excitation and the response amplitude (Eq. 3.21). The phase shift can be calculated knowing the angular frequency and the measured time shift between both temperature signals (Eq. 3.22).

$$A(\omega) = \frac{\hat{T}_{gl}}{\hat{T}_{abs}} \tag{3.21}$$

$$\varphi(\omega) = \omega \cdot \Delta t \tag{3.22}$$

where: Δt = time shift between both signals

3.3.2 Transient Excitation

In the preceding laboratory investigations, the absorber temperature was excited by electrical heating. With this technique, a sinusoidal excitation can be applied easily. A periodical excitation is challenging to achieve in a solar field. In the solar field, the collector holding the PTR to be excited is defocused and does not track the sun path. The absorber temperature thus relies on the HTF temperature (Eq. 2.1). The absorber temperature excitation can be applied by controlling the HTF inlet temperature. The HTF temperature excitation will either be achieved by focusing and defocusing upstream solar collectors or directly varying the HTF mass flow [Geller, 2012]. In this work, the HTF temperature is controlled by a temperature control unit on a field PTC rotary test bench (See 4.2.1). To realize a periodic excitation function in a solar field brings difficulties and uncertainties. In this work, a ramp-and-hold transient excitation function was investigated, which profile was also used in proceeding laboratory measurements.

For transient excitations, the amplitude ratio A and the phase shift φ of the response signal can be hardly analyzed by a direct visualization. Only the response to a step function can be analyzed graphically by its gain constant K and time coefficient τ_{PT1} for an angular frequency equal to 0 rad/s. A step function at the response is illustrated in Fig. 3.8. The gain constant K is the ratio of the asymptotical response temperature to the excitation temperature and the excitation temperature (Eq. 3.23). The time constant is the time when the step response has reached 63 % of the asymptotical value (Eq. 3.24). Practically, the asymptotical time is the time, when the response profile has reached its stationary magnitude, which is approximately t = 4000 s in Fig. 3.8.

$$A(\omega = 0) = K = \frac{\tilde{T}_{gl}}{\tilde{T}_{abs}} \tag{3.23}$$

$$T_{gl}(t = \tau_{PT1}) = 0.63 \cdot \tilde{T} \tag{3.24}$$

where: $\tilde{T}_{abs}$ = stationary magnitude of absorber temperature excitation [K]
$\tilde{T}_{gl}$ = stationary magnitude of glass temperature response [K]

However, a step temperature function can be hardly realized in thermodynamical systems and is only approximated by a ramp-and-hold signal. As the step function changes immediately it shows only two values and thereby it is not continuous in its domain $f: \mathbb{R} \Rightarrow \mathbb{R}$ at $t = t_0$ (Eq. 3.25).

$$T_{abs}(t) = \begin{cases} \overline{T}_{abs} - \frac{\tilde{T}_{abs}}{2} & \text{if } t < t_0 \\ \overline{T}_{abs} + \frac{\tilde{T}_{abs}}{2} & \text{if } t \geq t_0 \end{cases} \tag{3.25}$$

In contrast, the ramp-and-hold function shows three sections (Eq. 3.26). It is characterized by two time transitions, the ramp starting point t_0 and holding point t_1. Between these time transitions, the function increases linearly. Therefore, it is continuous in its full domain $f : \mathbb{R} \Rightarrow \mathbb{R}$ and can be realized by a thermodynamical system.

$$T_{abs}(t) = \begin{cases} \overline{T}_{abs} - \frac{\tilde{T}_{abs}}{2} & \text{if } t < t_0 \\ \overline{T}_{abs} - \frac{\tilde{T}_{abs}}{2} + \frac{\tilde{T}_{abs}}{(t_1 - t_0)} \cdot t & \text{if } t_0 \leq t < t_1 \\ \overline{T}_{abs} + \frac{\tilde{T}_{abs}}{2} & \text{if } t \geq t_1 \end{cases} \tag{3.26}$$

The step function is the a specific case of the ramp-and-hold function, using $\lim_{(t_1 - t_0) \to 0} T(t)$.

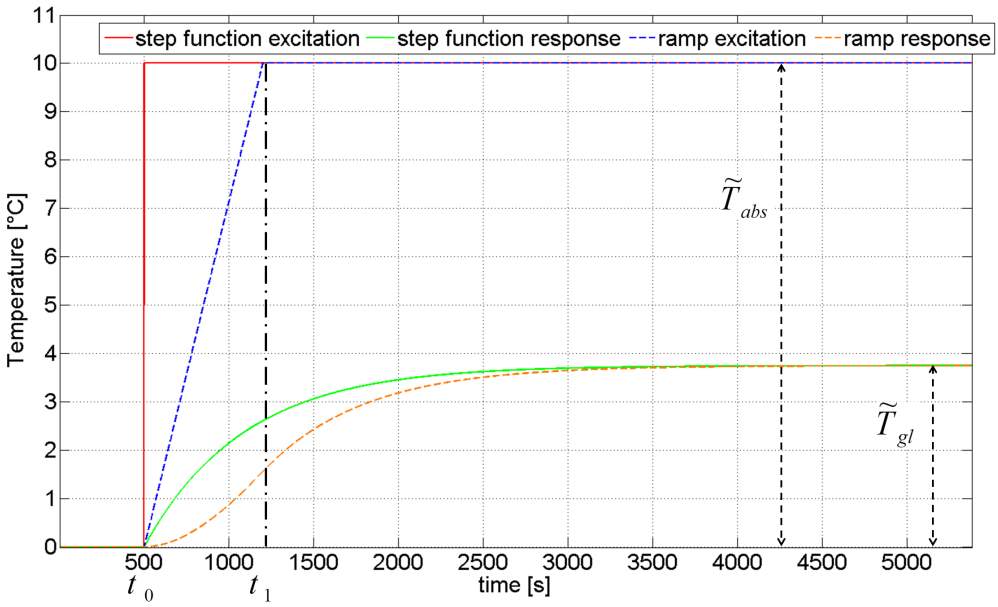

Figure 3.8: Illustration of step and ramp-and-hold excitation signal with simulated response signals. $t_0 = 500s$, $t_1 = 1200s$, $A(\omega) = 0.06$, $\varphi(\omega) = -1.4$ rad and $\omega = 2\pi/600\ s$

In Fig. 3.8 one can see both excitation functions, one ideal step function and one ideal ramp-and-hold function, as well as simulated responses for the given amplitude and phase shift values. The response signal is different. In fact the gain constant K for the response temperature $\lim_{t \to \infty} T(t)$ is the same value. But the dynamic of both response profiles differs concerning the slew rate. The moment, when the response value is 63 % of its final stationary magnitude is later for the response profile of ramp-and-hold excitations.

The amplitude ratio $A(\omega)$ for first-lag order systems ranges from 0 to 1. The phase shift $\varphi(\omega)$ range is [0°, 90°]. respectively [0 rad; -1.5758 rad]. Both values depend on the angular frequency. In Fig. 3.9, $A(\omega)$ and $\varphi(\omega)$ are plotted versus the angular frequency on a Bode Diagram.

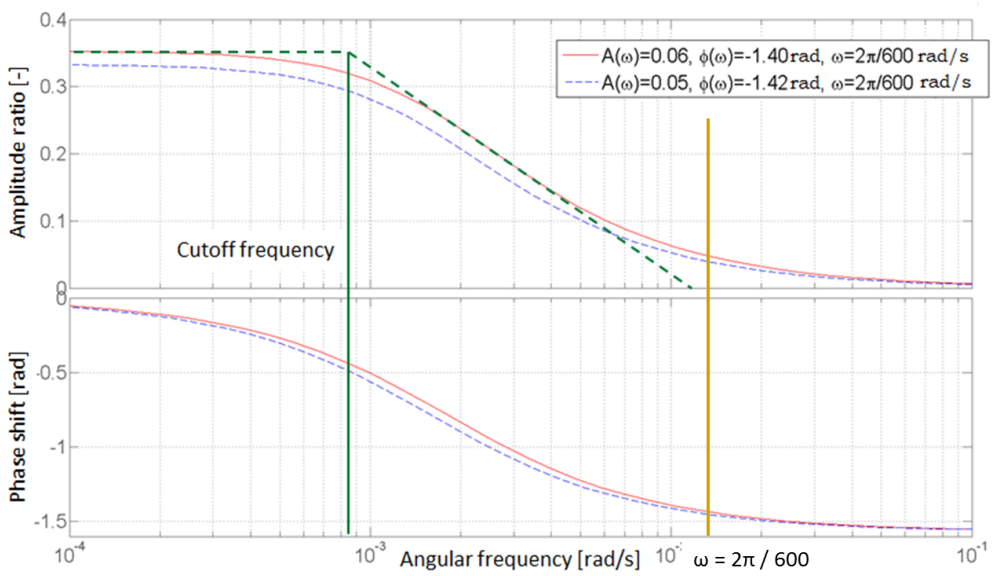

Figure 3.9: Bode diagram of two physically possible A and φ values with graphically cutoff frequency derivation (green line)

In this work, all response profiles are evaluated at the angular frequency of $\omega = 2\pi/600s$ (0.0105 Hz). For the investigated systems and its temperature response signals, this angular frequency is much greater than the cutoff frequency. The cut-off frequency is a certain frequency in a system's frequency response, at which the response signal amplitude start to reduces rapidly. It is graphically determined in Fig. 3.9. With a angular frequency much greater than the cutoff frequency, $A(\omega)$ tends towards zero and $\varphi(\omega)$ tends to -90°, respectively -1.5758 rad.

The amplitude ratio and the phase shift can be qualitatively linked to the receiver quality. For degraded PTR, the heat flows in the annulus between the absorber tube and the glass envelope are greater in magnitude in comparison to a new PTR. Receivers with degraded thermal properties shows a higher amplitude ratio A and a faster phase shift φ. That means, A is higher and φ increases to a faster phase shift.

Based on previous experimental work, φ is expected to be about -1.40 and -1.44 [rad] and A is about 0.055 to 0.065 for the working point of 350 °C, valid for a new, non-degenerated receiver. On Fig. 3.9 at an angular frequency of $\omega = 0$, one can read the gain factor K directly and thus the expected temperature response lift $\tilde{T_{gl}}$, valid for the expected A and φ values. That means, the ideal stationary magnitude of the glass temperature response should lie between 3 and 4 K, when

the absorber excitation temperature lift $\tilde{T}_{abs}$ is 10 K.

Fig. 3.10 illustrate different response signals to the same transient excitation. The response signal's properties phase shift φ and amplitude ratio A are in the range of the expected values of PTR transient measurements for an angular frequency of $\omega = 2\pi/600s$. The values can be looked up in Table 3.1. One can observe, that the phase shift φ influences the slew rate. A higher phase shift value leads to a faster increasing response signal (Eq. 3.12). Also, the phase shift has an influence of the stationary magnitude of the response temperature. The amplitude ratio only influences the gain constant and thus the temperature the stationary magnitude. Frequency responses with an equal phase shift but with different amplitude ratio reaches the $0.63 \cdot \tilde{T}$ value at the same moment. Frequency responses with an equal amplitude ratio but a different phase shift have a different $\tilde{T}$ value as well as they reach the $0.63 \cdot \tilde{T}$ value at a different moment. It is worth noticing, that the response signals for the values φ = -1.42 and A = 0.055 on the one hand, on the other hand with φ = -1.40 and A = 0.06 have a very similar course until they reach their $0.95 \cdot \tilde{T}$ value, as it can be seen in the subplot in Fig. 3.10.

Table 3.1: A and φ values and corresponding time constant τ at $T_{out}(\tau)$=$0.63 \cdot \tilde{T}_{out}$ and response temperature lift $\tilde{T}_{out}$ for a ramp-and-hold excitation with $\tilde{T}_{in}$ = 10 K and $t_1 - t_0$ = 600 s

Response	A [-]	φ [rad]	τ [s]	$\tilde{T}_{out}$ [°C]
y1	0.55	-1.42	1005	3.65
y2	0.55	-1.40	934	3.23
y3	0.60	-1.42	1005	3.99
y4	0.60	-1.40	934	3.53

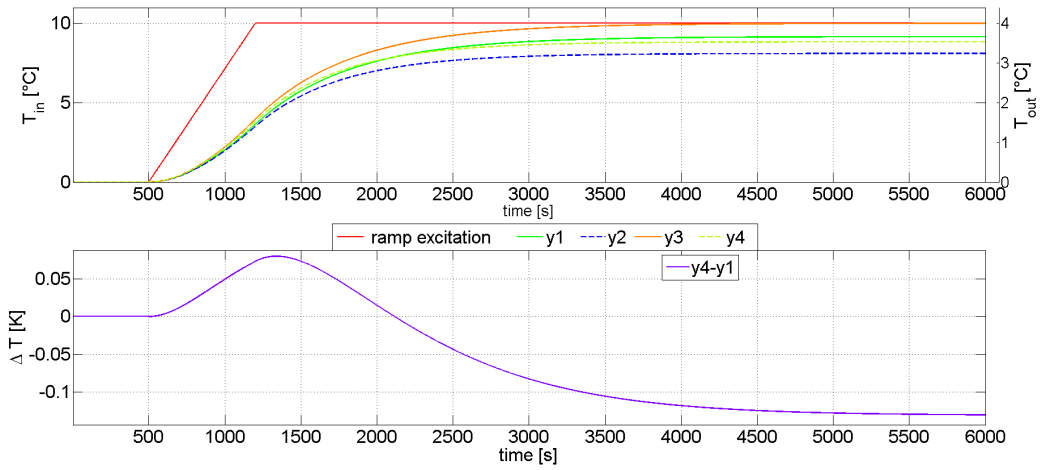

Figure 3.10: Simulated first-order lag element in response for different values (Table 3.1) of amplitude ratio and phase shift responding to a transient ramp-and-hold excitation

4 Experimental Setups

4.1 Experimental Equipment

4.1.1 Infrared Pyrometers

The absorber tube and glass envelope outer surface temperature measurements are performed with two infrared radiation pyrometers. Both devices are supplied by *DIAS Infrared GmbH*, Germany. The absorber temperature is measured with the *PYROSPOT DGE 10N* infrared pyrometer. The glass temperature is measured with the *PYROSPOT DT 44LH* infrared pyrometer. Table 4.1 reports briefly the technical specifications of both pyrometers. As described in Subsection 3.1.1 and according to Fig. 3.2, the spectral range of both pyrometers is chosen in that way, that the PTR's glass envelope is transparent for the pyrometer measuring the absorber temperature and opaque for the pyrometer measuring the glass temperature. Both pyrometers communicate with the software PYROSOFT Spot Pro. It is used to adjust the pyrometer settings and it records the temperature measurement of both devices.

Table 4.1: Pyrometer technical specifications

Pyrometer	**DGE 10N**	**DT 44LH**
Measuring point	absorber temperature $T_{abs}(t)$	glass temperature $T_{gl}(t)$
Measuring range	100 ... 600 °C	0 ... 1000 °C
Spectral range	2.0 ... 2.6 µm	8 ... 14 µm
Emissivity factor range ϵ	0.050 ... 1.000	0.2000 ... 1.000
Uncertainty[1]	0.5 % of meas. value in °C or 1 K	0.6 % of meas. value in °C or 1 K
Repeatability[1]	0.1 % of meas. value in °C or 0.5 K	0.3 % of meas. value in °C or 0.5 K
NEDT[2]	0.1 °C	0.1 °C

[1] higher value is valid
[2] noise equivalent temperature difference

4.1.2 Thermocouples

Thermocouples are used to measure different temperature on the experimental setup. Thermocouples consist of two conductors made of different materials contacting each other. When the temperature on one connecting end differs from the temperature on the other end, an electrical

potential appears that depends on the temperature difference. This thermoelectric effect can be measured. Thermocouples have a high temperature range. In comparison to infrared pyrometers, thermocouples have a slightly lower accuracy and a higher response time. Type K thermocouples can measure temperature in the range of 0 °C up to 1100 °C for long operating, from -180 °C up to 1300 °C concerning short-therm measurements. The smallest available uncertainty is ± 1.5 K in the temperature range between -40 °C and 375 °C. [Koertvelyessy, 1998]

Thermocouples measure the glass temperature, air temperature and, in laboratory applications, the inner absorber tube temperature. For glass temperature measurement, thermal paste is applied to the tip of thermocouples to enhance the thermal contact between these sensors and the glass envelope. The thermocouples are required to calibrate each pyrometer emissivity factor setting and cross-check analog pyrometer signals, in order to detect potential outliers. The allocation and positioning of thermocouples differs between field and laboratory experimental setups. A sketch of thermocouples positions during laboratory measurement is illustrated in Fig. 4.1. This setup can not be realized in field, as the inside of the absorber tube is not accessible. The experimental setups of each thermocouples setting is presented in Table 4.3. Further details of the air measurement approach are presented in Section 4.4.

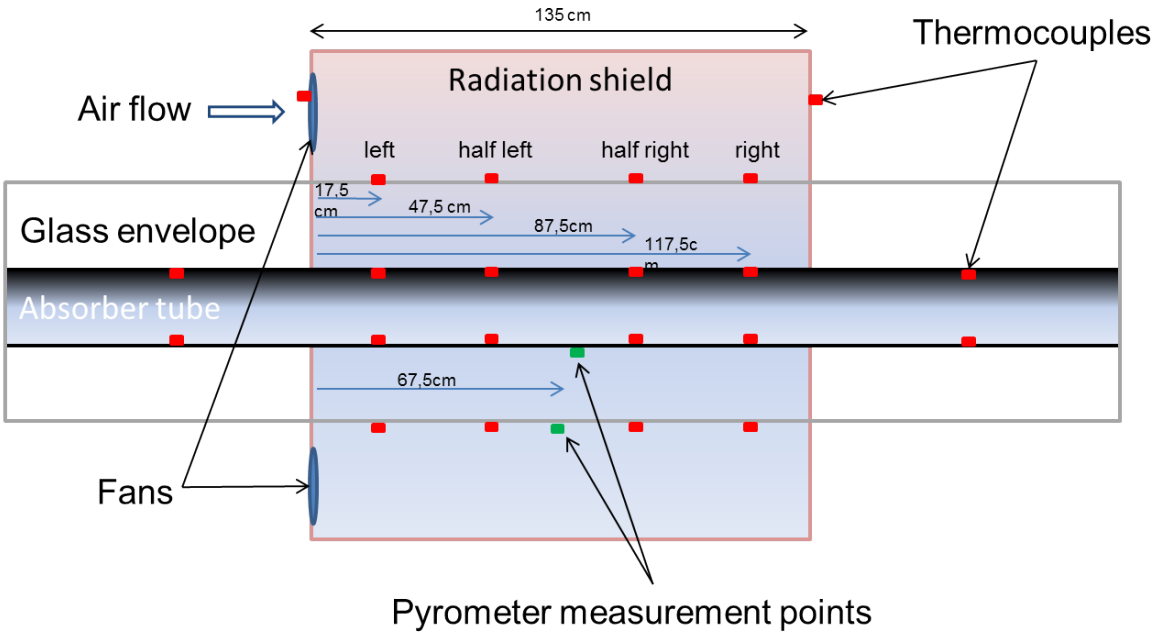

Figure 4.1: Positioning of thermocouples and pyrometer measurement points for laboratory experiments

4.1.3 Radiation Shield

The radiation shield is 1.35 m long. The radiation shield jacket is made out of a thin aluminum cylindrical jacket. An infrared reflecting foil covers the radiation shield inner surface. This reduces significantly thermal radiation exchange to the ambient. It is supposed to reflect 95 % of the thermal radiation emitted by the glass envelope back to itself [Roeger et al., 2014]. Hence, the radiation heat flow from the glass surface to the ambient can be neglected.

Two small apertures of 6 mm are drilled in the radiation shield jacket. These apertures allow infrared pyrometer measurements. The second aperture is added in order that the pyrometer can be aligned nearly perpendicular to their corresponding measurement surface. This reduces angular effects.

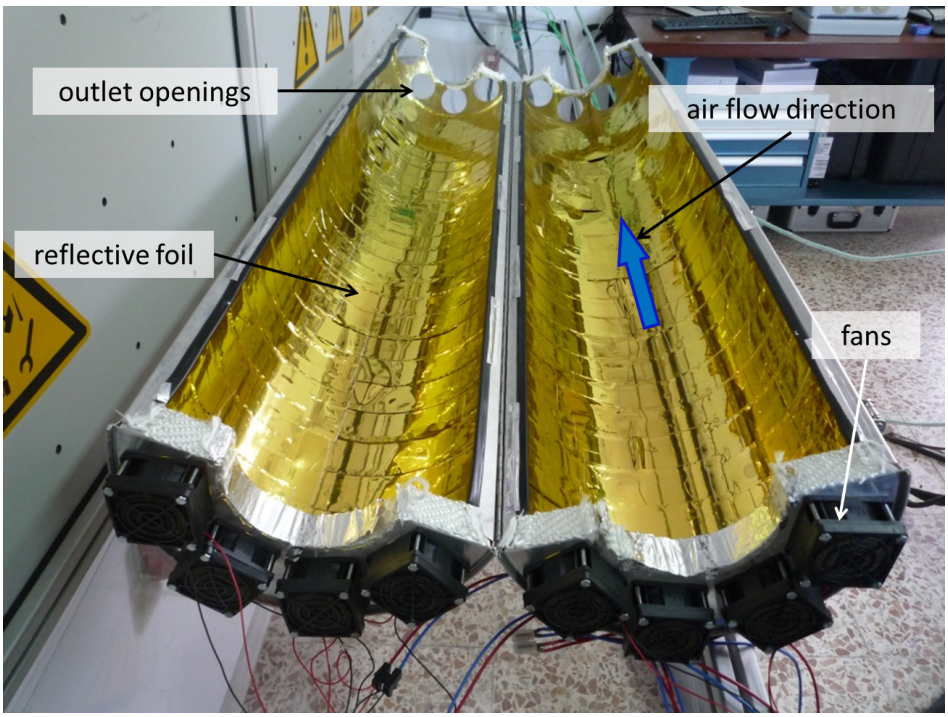

Figure 4.2: Inner face of dismounted and opened radiation shield

As described in Section 3.1.2, the radiation shield is supposed to provide a steady air velocity on the outer glass envelope surface. The steady air velocity parallel to the glass envelope is obtained by eight installed fans on the radiation shield inlet. The electrical cabling consists of two circuits for 4 fans connected in parallel. A programmable power supply is used to control the power settings of each loop circuit. The maximum power that can be supplied to each circuit is 9.6 W at a voltage of 12 V. The current setting ranges from 350 mA to 800 mA. Bellow a current setting of 350 mA at 4 V, the power is too small to guarantee a continuous operation of the fans. The air velocity inside the radiation shield at the lowest power setting is estimated between 0.33 and 0.49 m/s [Gaertner,

2013]. On the opposite side of the fans, at the radiation shield outlet, eight holes are positioned symmetrically. Each hole diameter is 60 mm. The holes provides, that a constant air flow can emerge within the radiation shield and a heat build-up is avoided.

Table 4.2: Original radiation shield properties

Length	1.35 m
Infrared foil reflectivity	approx. 95 %
Number of outlet holes	8
Outlet hole diameter	60 mm
Outlet area	0.01131 m^2
Maximum fan circuit power / voltage	9.6 W / 12 V
Estimated air velocity at i_{fan}=350 mA	0.33 - 0.49 m/s

4.1.4 Data Acquisition System

The control cabinet is the main part of the data acquisition system. The data acquisition system includes a controller (*Q.pac DL*) and a set of data acquisition modules: one *Q.bloxx A107* and three *Q.bloxx A104*. The *Q.bloxx A107* has two channel for pyrometer analog measurements, one channel for a PT100 measuring ambient temperature and one channel for the input voltage measurement of the Joule heating system during laboratory measurements. The three *Q.bloxx A104* provide 24 channels for thermocouples measurements, which set up is presented in Table 4.3.

The acquisition system is configured and the Ethernet interface is controlled by the *test.commander* software, supplied by *Gantner Instruments GmbH*, Germany. The measurement data are logged and visualized with the software *test.viewer*. The logging frequency is 5 Hz.

4.1.5 Parabolic Trough Receivers

This work is dealing with parabolic trough receivers *HCEOI-12* manufactured by *Archimede Solar Energy*, Italy. These PTRs have a selective coating on their absorber tube and are designed for thermal oil HTF. The absorber tube wall thickness is 2 mm. The annulus is evacuated to a pressure smaller than 10^{-4} mbar. The specific heat loss $\dot{q}'_{loss}$ is around 265 W/m at a absorber temperature of 400 °C, when the bellows are not insulated. PTR dimensions and specifications can be found in Appendix A.

Table 4.3: Allocation of data acquisition channels and thermocouple positioning for the first field measurement campaign (column 1), additional field measurement campaign (column 2) laboratory measurements (column 3). Indices: l: left; hl: half left; fr: far left; r: right; hr: half rigth; fr: far right; t: top position; b: bottom position; o: outlet; i: inlet

Channel Name	**Range & Unit**	**Application in**		
		1	**2**	**3**
1: Pyro1_DGE10N	0 ... 20 mA	T_{abs}	T_{abs}	T_{abs}
2: Pyro2_DT44LH	0 ... 20 mA	T_{gl}	T_{gl}	T_{gl}
3: InputVoltage	0 ... 10 V	—	u_{abs}	—
4: AmbientTemp	-50 ... 600 °C	T_{amb}	T_{amb}	T_{amb}
5: tc01	-100 ... 1000 °C	$T_{gl,hl,t}$	$T_{gl,hl,t}$	$T_{gl,hl,t}$
6: tc02	-100 ... 1000 °C	$T_{gl,hl,b}$	$T_{gl,hl,b}$	$T_{gl,hl,b}$
7: tc03	-100 ... 1000 °C	$T_{gl,hr,t}$	$T_{gl,hr,t}$	$T_{gl,hr,t}$
8: tc04	-100 ... 1000 °C	$T_{gl,hr,b}$	$T_{gl,hr,b}$	$T_{gl,hr,b}$
9: tc05	-100 ... 1000 °C	—	$\mathrm{T}_{abs,hr,t}$	—
10: tc06	-100 ... 1000 °C	—	$\mathrm{T}_{abs,hr,b}$	—
11: tc07	-100 ... 1000 °C	—	$\mathrm{T}_{abs,hl,t}$	—
12: tc08	-100 ... 1000 °C	—	$\mathrm{T}_{abs,hl,b}$	—
13: tc09	-100 ... 1000 °C	$T_{gl,l,t}$	$T_{gl,l,t}$	$T_{gl,l,t}$
14: tc10	-100 ... 1000 °C	$T_{gl,l,b}$	$T_{gl,l,b}$	$T_{gl,l,b}$
15: tc11	-100 ... 1000 °C	$T_{gl,r,t}$	$T_{gl,r,t}$	$T_{gl,r,t}$
16: tc12	-100 ... 1000 °C	$T_{gl,r,b}$	$T_{gl,r,b}$	$T_{gl,r,b}$
17: tc13	-100 ... 1000 °C	—	$\mathrm{T}_{abs,r,t}$	$\mathrm{T}_{air,o,b}$
18: tc14	-100 ... 1000 °C	—	$\mathrm{T}_{abs,r,b}$	$\mathrm{T}_{air,o,t}$
19: tc15	-100 ... 1000 °C	—	$\mathrm{T}_{abs,l,t}$	—
20: tc16	-100 ... 1000 °C	—	$\mathrm{T}_{abs,l,b}$	—
21: tc17	-100 ... 1000 °C	$\mathrm{T}_{air,o}$	$\mathrm{T}_{air,i}$	—
22: tc18	-100 ... 1000 °C	$\mathrm{T}_{air,o}$	$\mathrm{T}_{air,i}$	$\mathrm{T}_{air,i}$
23: tc19	-100 ... 1000 °C	$\mathrm{T}_{air,i}$	$\mathrm{T}_{air,o}$	—
24: tc20	-100 ... 1000 °C	$\mathrm{T}_{air,i}$	$\mathrm{T}_{air,o}$	—
25: tc21	-100 ... 1000 °C	—	$\mathrm{T}_{abs,fr,t}$	$\mathrm{T}_{air,o,b}$
26: tc22	-100 ... 1000 °C	—	$\mathrm{T}_{abs,fr,b}$	$\mathrm{T}_{air,o,t}$
27: tc23	-100 ... 1000 °C	—	$\mathrm{T}_{abs,fl,t}$	—
28: tc24	-100 ... 1000 °C	—	$\mathrm{T}_{abs,fl,b}$	—

4.2 Field Measurements

4.2.1 KONTAS Test Bench

The field measurement campaigns are realized at KONTAS (Konzentrator-Teststand Almería Spanien; Concentrator test bench Almería Spain), installed on the Plataforma Solar de Almería. KONTAS is a 360° rotary test bench for parabolic trough collector components, which was constructed in 2009.

It provides a field environment for the qualification of a PTC module with a maximum length of 20 m. The rotary test bench permits to set any desired tracking angle. Single collector modules can be investigated and tested under realistic operating conditions. A side view of the facility is illustrated in Fig. 4.3, on which the HTF temperature control unit can be seen (white block). On this figure, the PTC is tracking the sun during a midsummer day a noon time.

The HTF temperature is maintained by a LAUDA process temperature control unit (TCU) (*KH400 L*). The TCU includes a mechanical, air cooled chiller for the cooling unit and an electrical heater to heat up the HTF up to a temperature of 400 °C, which is the maximum temperature setting for thermal oil. The available cooling power is 100 kW. The integrated electrical heating power is 57 kW.

The HTF is *Syltherm 800*, which is pumped through the closed cycle and travels from the TCU through the PTC and returns back to the TCU. The HTF mass flow rate can be set between 0.5 and 5.2 kg/s. The maximum system pressure is 16 bar and can be monitored continuously. The HTF cycle is monitored by PT100 temperature sensors and a Coriolis mass flow sensor.

The thermal oil *Syltherm 800* is characterized as highly stable with low potential of fouling and is low in oral toxicity. Its physical properties are listed in Appendix A. The KONTAS facility allows the realization of ramp-and-hold excitation functions described in Subsection 3.3 on working points of 300 °C and 350 °C.

Figure 4.3: Side view of KONTAS rotary test bench

Furthermore, a high precision meteorological station is installed next to the facility and provides accurate data for solar radiation, ambient temperature, wind velocity and direction. [Heller et al., 2011]

In order to apply reproducible ramp profiles, the control parameters of the heating unit must be adjusted. The heating unit is controlled by a PID controller with its significant properties:

- ▹ P: proportional term,
- ▹ I: integral term,
- ▹ D: derivative term.

The proportional term takes the present difference between process variable and desired set point in account. The integral term depends on the errors in the past and the derivative term regards the actual rate of change between the process variable and desired set point. [Lunze, 2004]

The default settings defined by the TCU manufacturer generate an initial temperature overshoot followed by a dampened temperature oscillation. To avoid that, the optimal setting was determined in a short trial and error test campaign, following manufacturer proposals and adjustment rules defined by Chien, Hrones and Reswick [Lunze, 2004]. Table 4.4 presents the default and adjusted control parameters. The ramp-and-hold excitation profiles are shown in Fig. 4.4 before and after the adjustment of PID control parameters. The measured temperatures are performed on the outer absorber surface by infrared thermography.

Table 4.4: Adjustment of the ramp-and-hold excitation profile for the absorber temperature with different control settings for TCU

	P	**I**	**D**
original setting (1)	3.5	1.5	0.05
adjusted setting (2)	1.0	2.0	0.01

4.2.2 First Field Measurement Campaign

The experimental setup for transient thermography measurements installed on KONTAS test bench for the first field measurement campaign is shown in Fig. 4.5. The experimental setup is mounted on a 4 m long PTR located at the PTC mid-position. The radiation shield is mounted around the glass envelope. The PTC is not tracking the sun and it is oriented along an East-West axis. That means the inlet of the radiation shield is positioned in direction of 90 °N, the outlet in direction of 270 °N.

The pyrometers are mounted on mechanical supports which are attached to the radiation shield with clamps. A counter weight is mounted on the opposite side of the radiation shield to balance the torque induced by pyrometers.

Two thermocouples are placed at the radiation shield outlet to measure the outlet air temperature. The air temperature $\overline{T}_{air}$ inside of the radiation shield is calculated by averaging the this outlet temperatures with the ambient temperature, which is measured by a PT100.

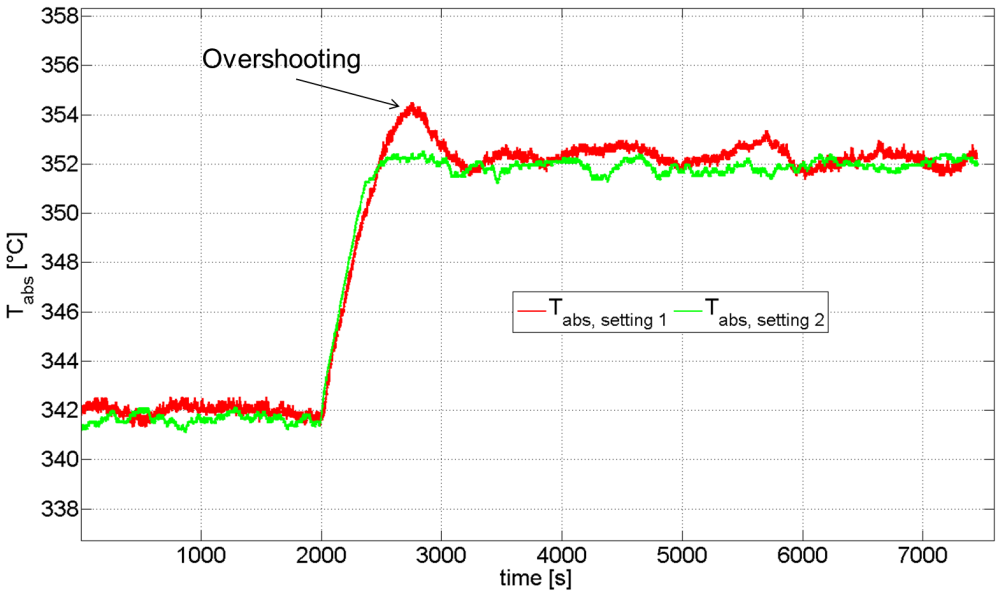

Figure 4.4: Ramps for transient measurement with different control settings of the HTF temperature controll unit

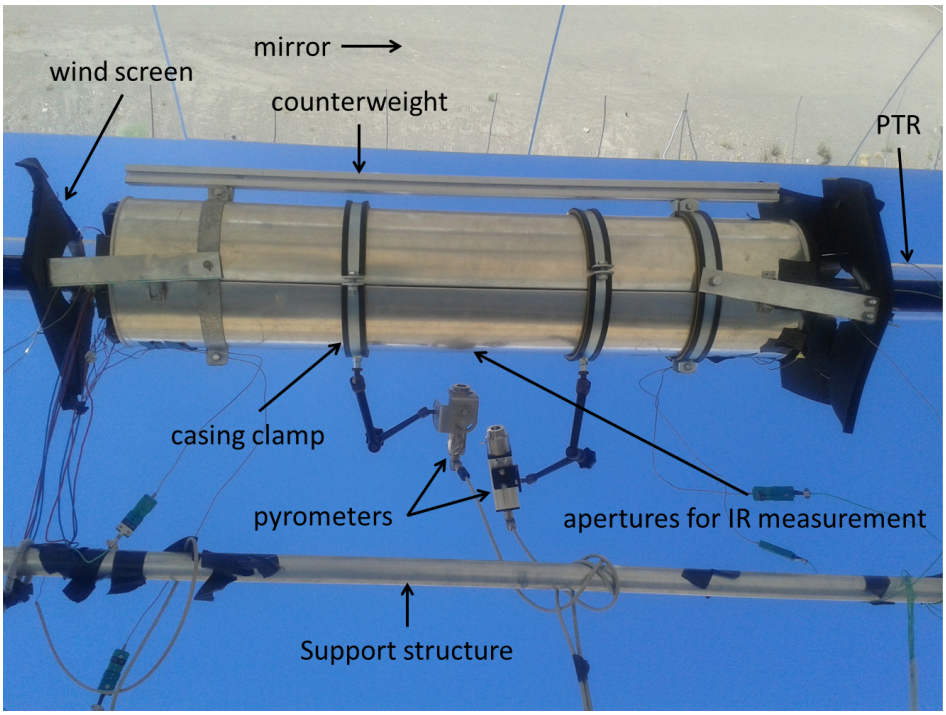

Figure 4.5: Experimental setup installed at KONTAS facility for transient thermography experiments during the first field measurement campaign

4.2.3 Additional Field Measurement Campaign

For the additional field measurement campaign, a bypass was installed on KONTAS facility. The line of PTRs was dismounted from the PTC focal line but remained connected to the HTF circuit. The PTR line was positioned 1.5 m above ground level, which improved the access to the experimental setup. The new setup is illustrated in Fig. 4.6.

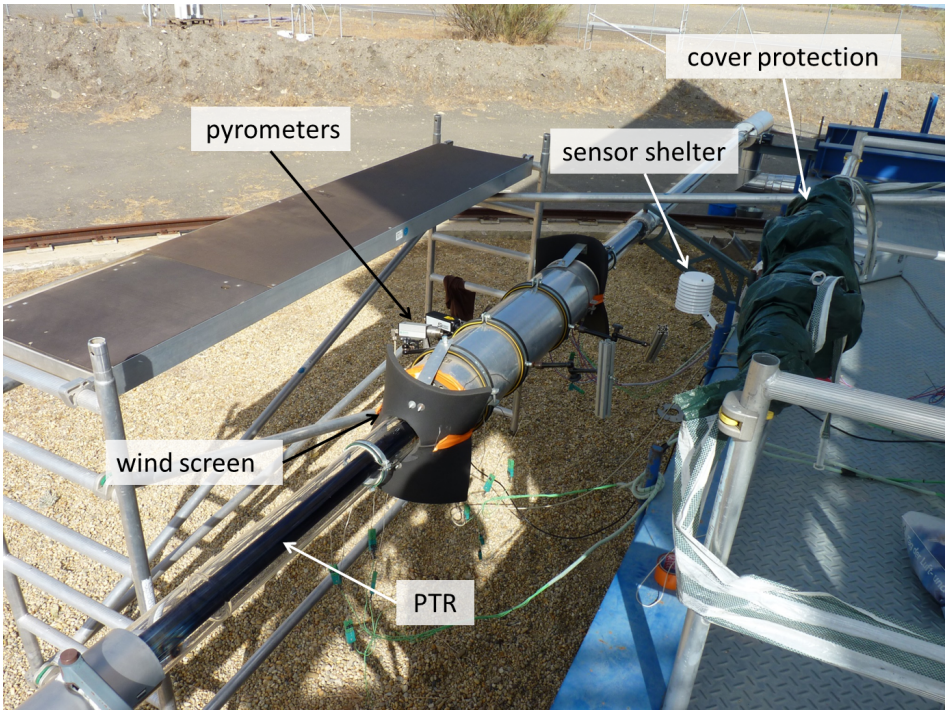

Figure 4.6: Experimental setup installed at KONTAS bypass for transient infrared thermography experiments during the additional field measurement campaign

The radiation shield air inlet temperature is measured by one thermocouple, which is placed inside of a sensor shelter. The sensor shelter protects the sensor of wind and radiation influences and avoids measurement errors.

In this setup, the receiver line is not longer shadowed by the mirrors, if the PTC axis is aligned along the East-West axis. In addition, the additional field campaign is performed during summer, with higher sun evaluation angles. To minimize the influence of solar radiation on the setup, a protective cover is mounted above the radiation shield.

In order to reduce the weight of the equipment mounted on the PTR, the counterweight balancing the torque induced by pyrometers is optimized.

Potential melting or flammability risks are reduced with this new setup. The rubber pads of the clamps, mounted on the glass envelope to attach thermocouples, are now insulated. Some rubber pads were observed to degrade when they were attached directly to the glass envelope.

4.3 Laboratory Measurements

To compare measurement results and investigate experimental setup improvements, laboratory measurements were performed between field measurement campaigns. Laboratory experimental setup is shown in Fig. 4.7. In this experimental setup, the absorber tube is connected to a transformer and heated by Joule heating. The absorber tube acts as a resistance. In contrast to field measurements, for laboratory measurements the infrared pyrometers are not directly mounted on the radiation shield for laboratory measurements. The pyrometer mechanical supports are mounted on an external mechanical framework. Otherwise, the laboratory setup is similar to the one described in [Gaertner, 2013].

In contrast to the previous measurement campaign documented in [Gaertner, 2013], another strategy was chosen to maintain a constant ambient conditions during the tests. Initial issue was a progressive ambient temperature increase during tests, due to the size of the laboratory and the heat loss of the receiver. During laboratory experiments, the window and door remained closed and the air conditioning temperature was set to 22 °C. With this setting, the air temperature was observed to remain stationary. A lower temperature could not be maintained constant during all tests, specially with high external temperatures at noon time. A higher ambient temperature setting led to temperature oscillations during experiments (See Fig. 4.10, between 9000 s and 15000 s).

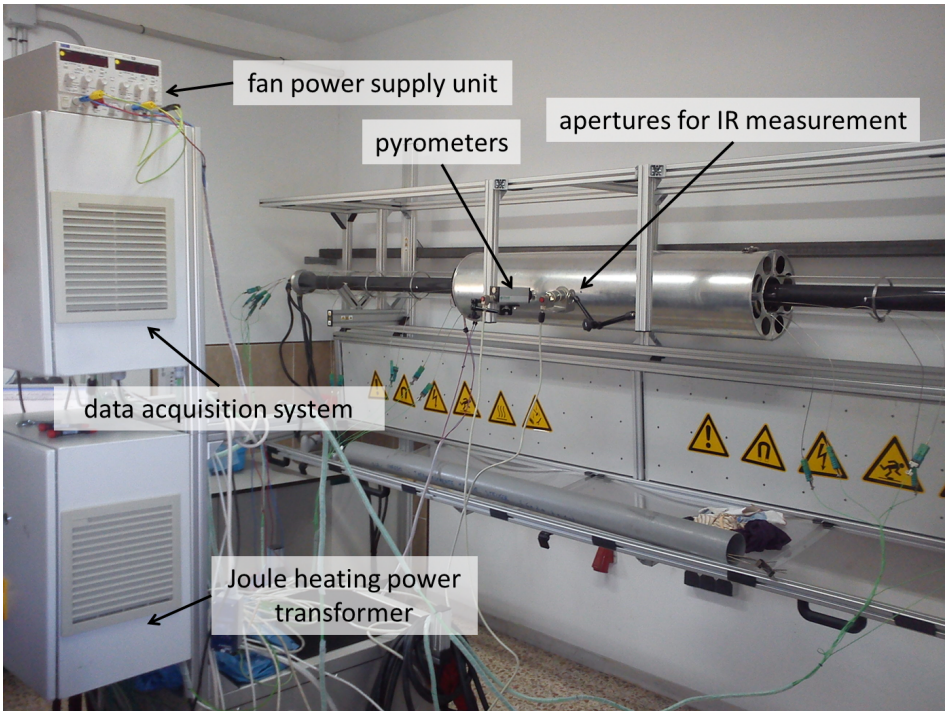

Figure 4.7: Laboratory test bench

4.4 Air Temperature Measurements

To determine the air temperature $\overline{T}_{air}$ inside the radiation shield, the inlet and outlet air temperatures are averaged.

The inlet temperature is equal to the ambient temperature, which is measured by a PT100 temperature sensor during the first field measurement campaign and the laboratory measurement. During the additional field campaign, the inlet air temperature is measured by a thermocouple placed in a sensor shelter (See Fig. 4.6). This is done, because some significant differences between the uncovered PT100 measuring the ambient temperature and the meteorological data logged by the meteorological station on KONTAS, where these sensor shelters are used as well, could be observed. One example is illustrated in Fig. 4.8, where a temperature difference up to 2 K can be observed during the transition time between day and night (09:00 PM).

The outlet temperature is measured by thermocouples at the radiation shield outlet openings. The type K, class 1 thermocouples have an temperature measurement uncertainty of ± 1.5 °C.

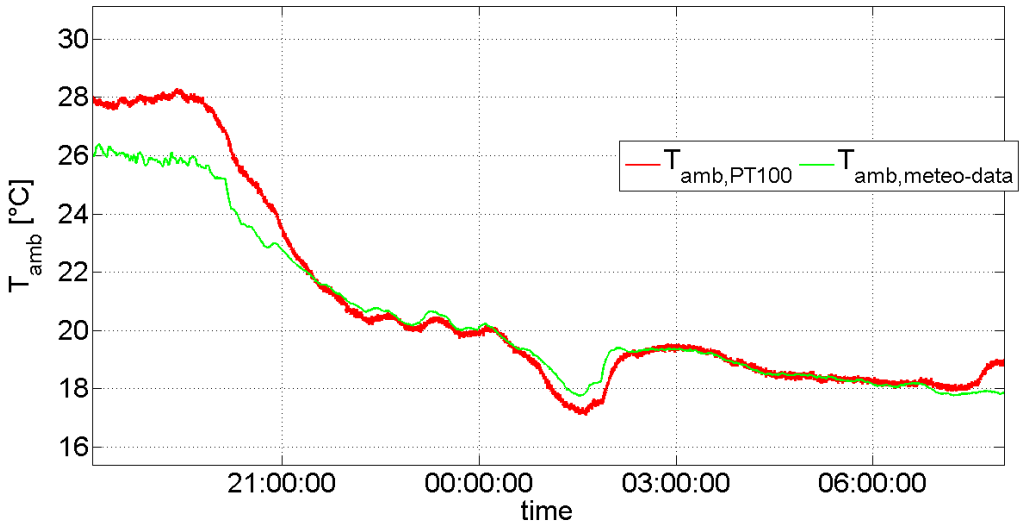

Figure 4.8: Ambient temperature measured by uncovered PT100 used in the experimental setup and measured by the meteorological station at KONTAS, Date of test: 05/20/2014

For the first approach, two thermocouples are positioned outside of the openings. In order to investigate if the glass temperature and the radiation shield reflection have an impact on the outlet air temperature measurement, one thermocouple is equipped with a provisional insulation. The thermocouple is inserted into a styrofoam cuboid enveloped by a thermal radiation reflective foil. A schematic of this cover and a picture are shown in Fig. 4.9.

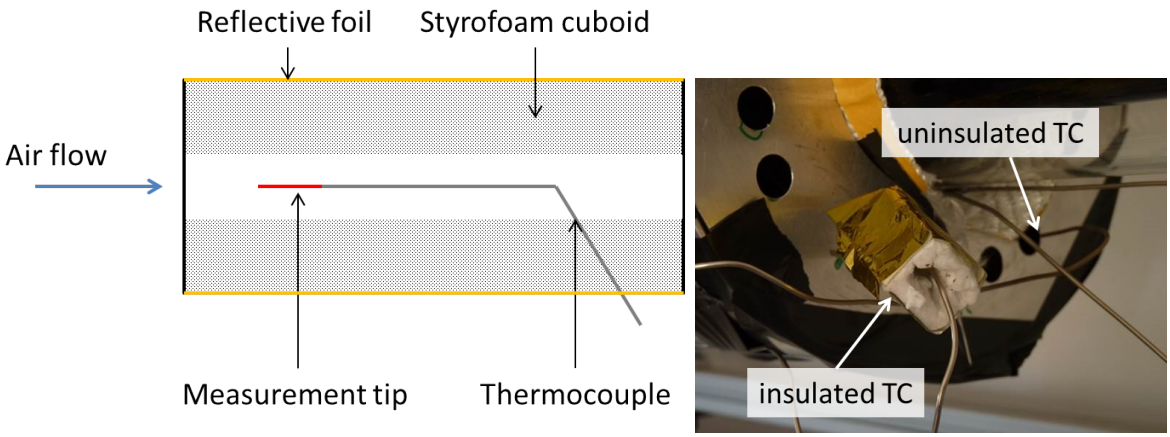

(a) Schematic of thermocouple insulation

(b) Thermocouple insulation mounted at the radiation shield outlet

Figure 4.9: Thermocouple insulation for outlet air measurement temperature measurement

During laboratory measurements, the insulation efficiency can be compared with the uninsulated measurement without ambient effects such like wind. Both thermocouples were placed at the same radiation shield outlet opening level. No significant difference could be observed between the two thermocouples measuring the outlet air temperature. An exemplary temperature profile is illustrated for the insulated and non insulated thermocouples measuring the outlet air temperature in Fig. 4.10. One can observe that the two air temperature measurements display a temperature difference always lower than 2 K and cross over at 24000 seconds. At this time, changes on the experimental setup were done. The thermocouples were displaced and placed again in the same configuration as before. This cross over and the difference between both temperatures can be allocated to uncertainties concerning the thermocouple measurement tip position as well as the type K thermocouple temperature measurement uncertainty. The provisional insulation does not change the measurement and it is assessed that it has a low insulation efficiency.

Exemplary air temperature measurements in the field are illustrated in Fig. 4.11. In contrast to laboratory measurements presented before, the insulated thermocouple was placed at the topmost radiation shield outlet opening. A difference of approximately 10 K between both temperature signals can be observed. This is caused by a temperature stratification of air temperature from the bottom to the top. This effect could be confirmed by the reversed configuration (Date of test: 05/26/2014)), even though the difference is observed to be smaller. In the field, the uninsulated thermocouple displays a higher noise. This could be explained by wind influences (v_{wind}> 6 m/s). The noise and a smaller difference in a reversed configuration tends to the observation that the wind influence decreases the measured temperature.

Another air temperature measurement setup investigated for field measurements is illustrated in Fig. 4.12. In this setup, the uninsulated thermocouple measurement tip is placed 20 mm inside of

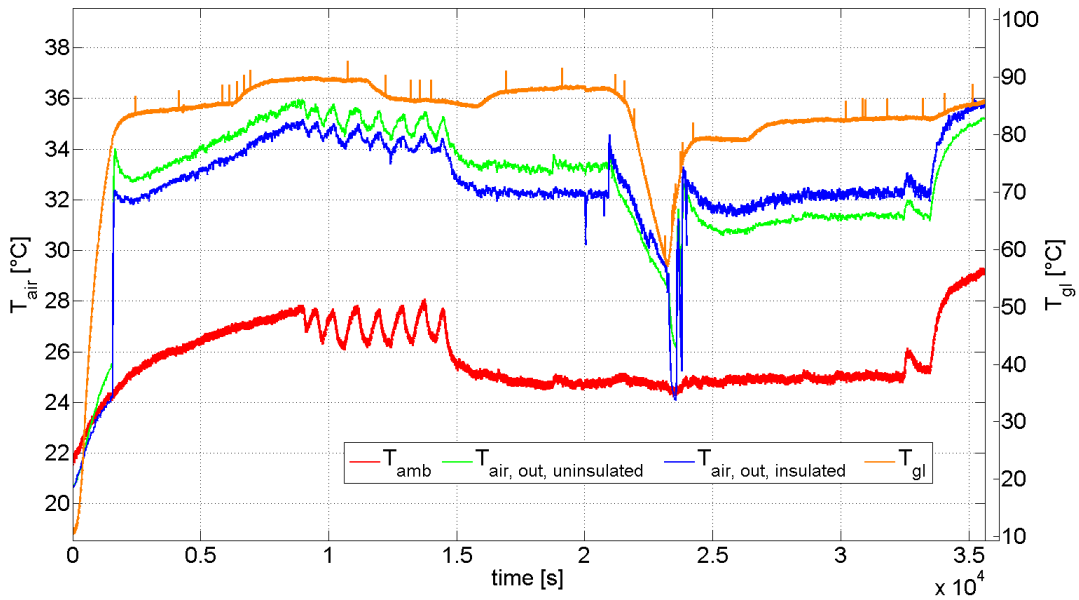

Figure 4.10: Air temperature measurement during laboratory measurements. Date of test: 07/17/2014, Complete test day. Stages: Heating up until approx. 2500 s, starting ramp at 6000 s, air conditioning set on 22 °C at 15000 s, starting ramp at 16000 s, working on experimental setup at 22000 s to 24000 s, turn of air conditioning at 33000 s

the radiation shield (Fig. 4.12, position 2). The uninsulated thermocouple on position 1 is mounted as in the previous setup and lies outside of the radiation shield. Thermocouples located at position 3 and 4 are covered by small tubes. On the outer surfaces of this tubes a reflective foil is applied. This is done to avoid wind influences on the measurement and that the radiation shield outlet air stream mixes with ambient air of lower temperature before the measurement. The thermal radiation insulation efficiency in this setup is expected to be higher, because the thermocouple does not touch the insulation material anymore. As well it is supposed to avoid wind influences.

The temperature profiles of the different thermocouples listed in the previous paragraph are compared in Fig. 4.13. The thermocouples for which the measurement tip is inserted inside the radiation shield (position 2) displays a higher temperature than the thermocouples mounted outside of the radiation shield outlet (position 1, 3 and 4). This observation could be explained by the influence of thermal radiation. This thermocouple faces the glass envelope on one side and the infrared reflecting foil on the other side. It absorbs more of the thermal radiation emitted by the glass envelope than the thermocouples positioned outside the radiation shield.

The thermocouples located on positions 3 and 4 confirm the temperature stratification observed in previous experiments (Fig. 4.11). Still the measured difference is smaller and below 5 K.

The thermocouple located on position 1 shows a slightly higher temperature, although it is posi-

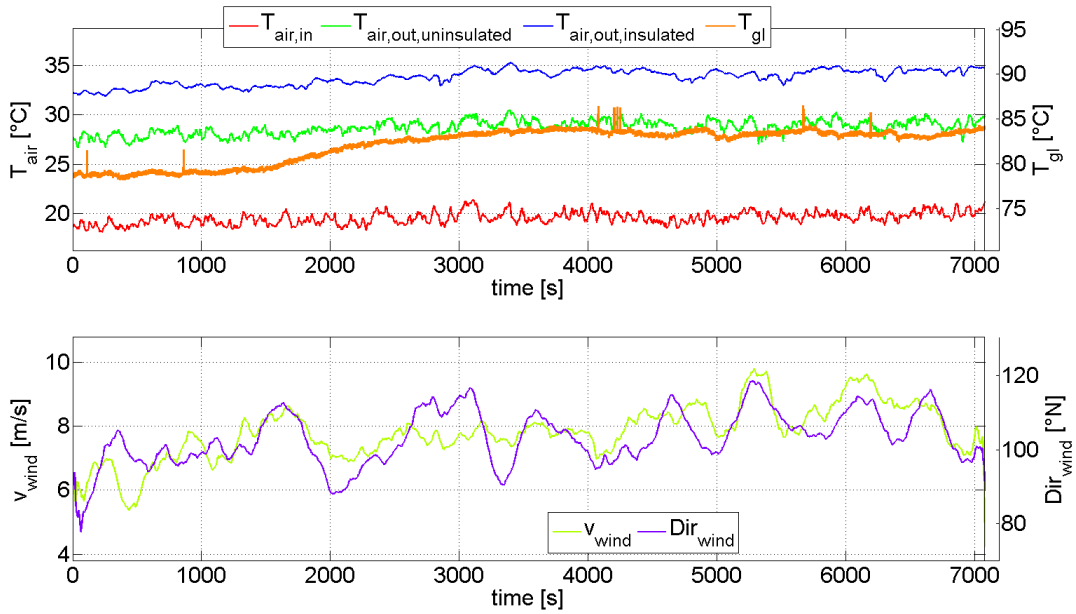

Figure 4.11: Air temperature measurement during field measurements. Date of test: 05/15/2014, Start of Ramp 01:15 PM

tioned on the same level as the thermocouple at position 3. It is approximated that this higher temperature is caused by thermal radiation influence by the elevated glass temperature. That would mean that the small tubes covering the thermocouples on position 3 and 4 is a more efficient thermal radiation insulation.

During the additional field measurement campaign only the outlet air temperatures measured on position 3 and 4 are considered to calculate the air temperature $\overline{T}_{air}$ within the radiation shield.

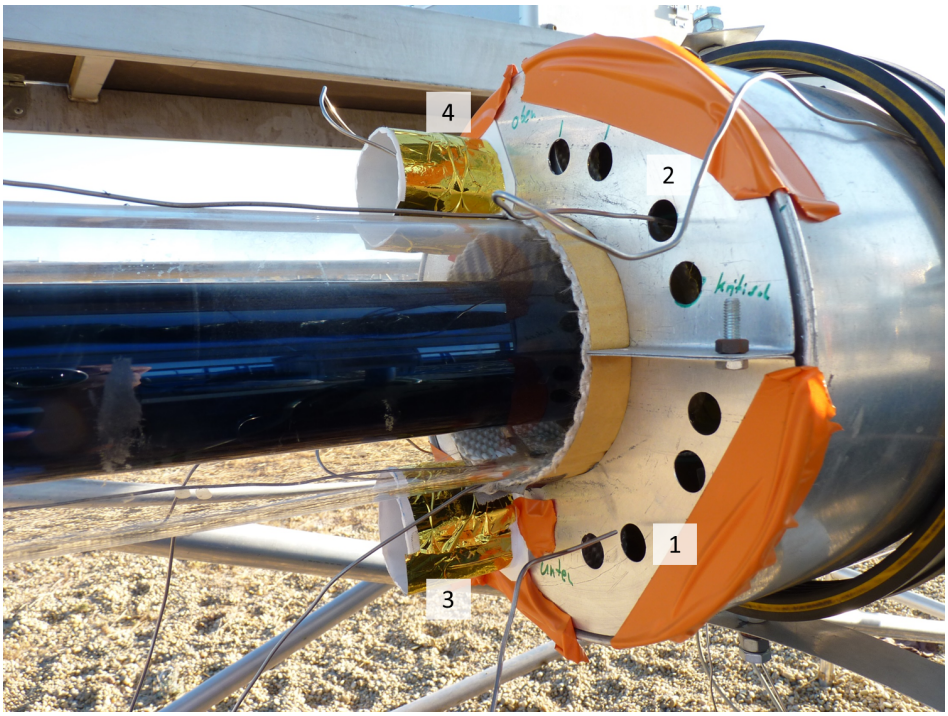

Figure 4.12: Different setups for air outlet temperature measurement during field measurements. Date of test: 09/02/2014, Start of Ramp 02:00 PM

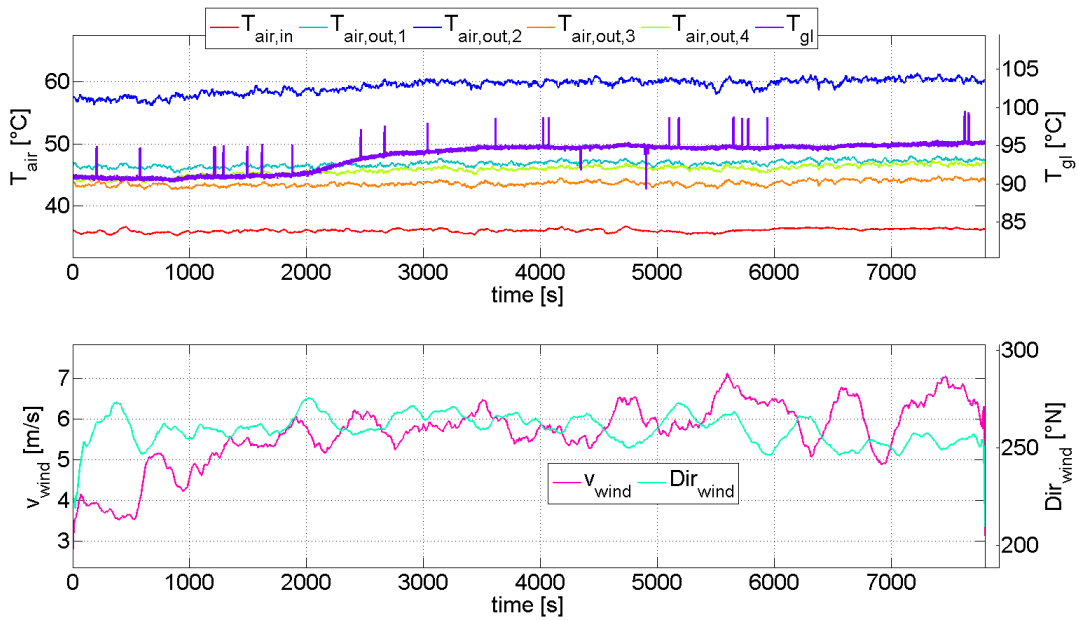

Figure 4.13: Air temperature measurement during laboratory measurements. Date of test: 09/02/2014, Start of Ramp 02:00 PM

5 Operational Procedures

5.1 Experimental Procedures

The operation procedure outline of a transient thermography test is illustrated in Fig. 5.1 and described in the following paragraphs.

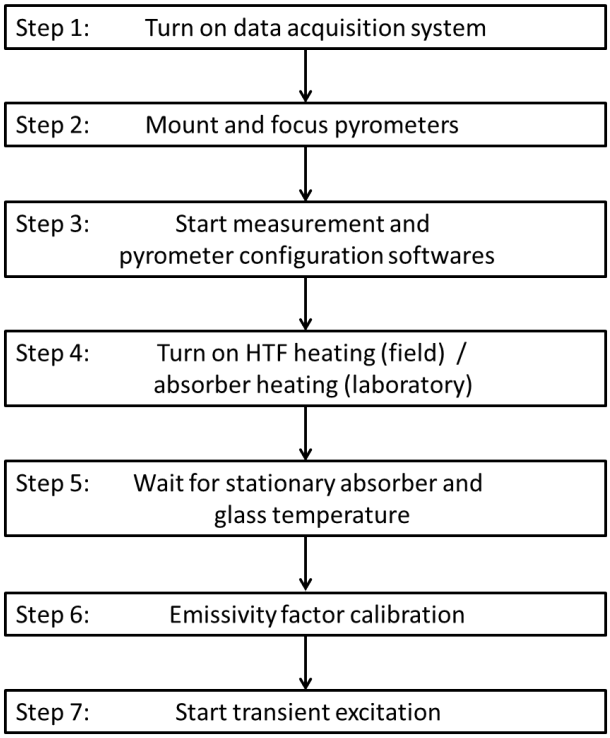

Figure 5.1: Operational procedure workflow

Step 1

The control cabinet main switch is turned on. The data acquisition system should be supplied with power.

Step 2

Both pyrometers are mounted on their mechanical supports and cabled to the data acquisition system. Both pyrometers can be focused on their targets using the integrated LED aiming lights. These aiming lights are aligned with their respective pyrometer optics and have to be focused at the corresponding apertures in the radiation shield. The diameter of

measurement points is related to the distance between pyrometers and corresponding radiation shield apertures. The diameter of the measurement point is minimal at the pyrometer focal point. The LED light indicates the diameter of the measurement point. The focal point of each pyrometer must correspond to the corresponding radiation shield aperture. Once both pyrometers are correctly positions, LED aiming lights have to be switched off.

Step 3

The data acquisition software (Test Viewer) and the pyrometer configuration software (Pyrosoft Spot Pro) can be started. The radiation shield fan power supply is turned on and adjusted to the desired voltage and current settings.

Step 4

The receiver heating system is turned on and the desired temperature is set. For field measurements, this requires the activation of the LAUDA TCU, which heats up the thermal oil HTF and pumps it through the line of PTRs. The desired temperature can be set with the KONTAS controlling system. For laboratory measurements, the receiver heating is done by Joule heating. Here, the desired temperature is set by applying the corresponding Joule heating voltage [Gaertner, 2013].

Step 5

The absorber heating process lasts approximately 120 minutes for field measurements, depending on the desired absorber temperature working point. For laboratory measurement, the desired absorber temperature can be achieved within 20 minutes. Once the absorber temperature is quasi-stationary, the glass temperature stabilizes within approximately 30 minutes, if the ambient conditions remain stable.

Step 6

For field measurements, it is assumed that the inner absorber surface temperature equals the HTF temperature averaged between the inlet and outlet of the collector. 0.5 K is subtracted from this temperature to account for the conduction loss across the absorber wall. The outer absorber surface temperature can only be approximated. The certain known temperature is the HTF inlet temperature as well as the outlet temperature in the additional field campaign, which are measured by PT100 temperature sensors.

For field measurements, it can be observed that the absorber outer surface temperature increases as the HTF mass flow increases. This effect is shown in Fig. 5.2. For this example, the pyrometer emissivity factor is calibrated for the lowest mass flow of 1 kg/s. As the mass flow increases, the outer absorber temperature increases due to a better convective heat transfer coefficient between the HTF and the absorber inner surface. If the pyrometer setting is not calibrated correctly, the pyrometer temperature reading for the absorber overshoots the PT100 temperature reading for the HTF, which is physically incorrect. To handle this problem, the emissivity factor of the absorber pyrometer is adjusted at the maximal mass

flow, where the highest convective heat transfer between the HTF and the absorber can be achieved.

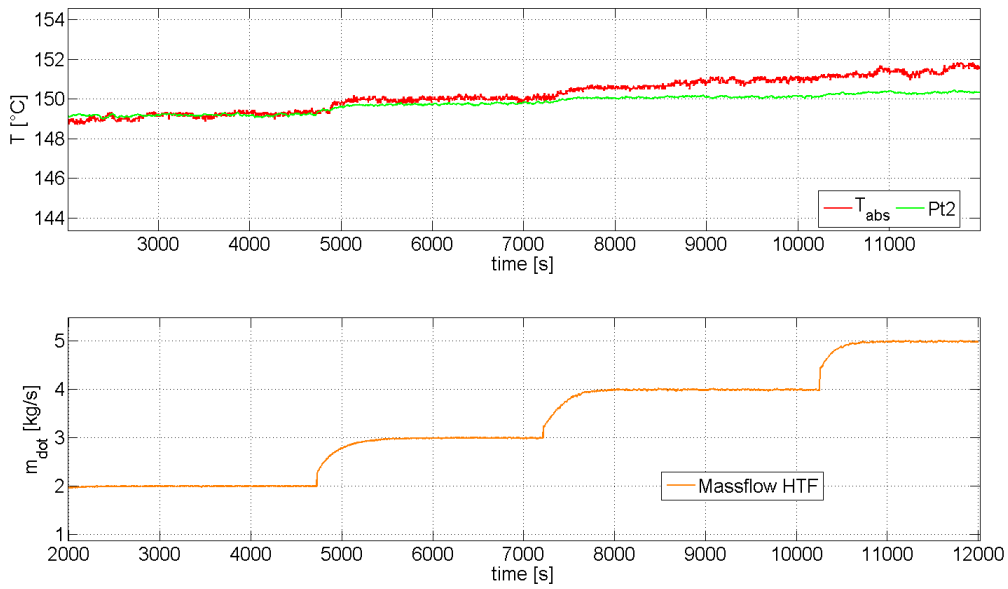

Figure 5.2: HTF temperature and absorber tube temperature as a function of mass flow

For laboratory tests, the emissivity factor is adjusted so that the temperature measured by the pyrometer (*Pyrospot DGE10N*) corresponds to the averaged thermocouple readings for the inner absorber surface (see Table 4.3).

For the glass pyrometer, the emissivity factor is set to a constant value of 0.89, based on previous experience [Gaertner, 2013]. The ambient temperature compensation remains activated.

Step 7

The last step of the experimental operation procedure is to start the transient measurement. The stability of the absorber and the glass pyrometer signals are monitored and recorded for 30 minutes before a transient excitation is applied to the absorber temperature. The ramp itself lasts approximately five minutes. The absorber temperature increases by about 10 K within this time. The absorber temperature is then stabilized again. From the beginning of the ramp on, the measuring lasts 70 minutes before a stable glass temperature level is reached. This is done to monitor the stability of the temperature according to its behavior affected by the ambient. Ambient parameters including ambient temperature, wind speed and direction are recorded during the experiment to investigate their potential influence on the transient measurement.

5.2 Data Evaluation Method

5.2.1 Data Evaluation Procedure

All measurement data is analyzed with MATLAB tools. The aim is to derive the mean temperatures $\overline{T}_{abs}$, $\overline{T}_{gl}$ and $\overline{T}_{air}$, to calculate φ and A measurands, as well as statistical indicators evaluating the quality of test results. The outline of the data evaluation method is listed in Table 5.1 and refers to the relevant MATLAB scripts.

Table 5.1: Data evaluation outline

Step	Action	Name Matlab Script
1.1	load raw data in workspace	LoadDataDLG.m
1.2	load KONTAS data in workspace	LoadKontas.m
2.1	query of general test information	ReportStampDLG.m
2.2	select type of excitation signal	SignalTypeSelectDLG.m
2.2	additional inputs for documentation and angular frequency selection	UserSettingsDLG.m
3	selection of thermocouples	Select_Ref_TCs.m
4	convert analog pyrometer signals	ConvertPyrometerSignals.m
5	select start and end points of selected data	ExtractDataSeries_multiplecuts.m
6 (a)	extraction of the selected time frame	ExtractDataSeriesTrans_multiplecuts.m
6 (b)	calculate mean temperatures	TransientMeanTempCalc_multiplecuts
6 (c)	generate variations of time frames and smooth glass temperature	ExtractVarAndSmooth_multiplecuts.m
6 (d)	calculate A and φ by two different algorithms	ExpCalcAmplPhaseTrans_multiplecut.m
6 (e)	simulate glass temperature function, compare with measured temperature profile	CheckResultPlots_multiplecuts.m
6 (f)	export results in excel sheet	ExtractResults_multiplecuts.m

Step 1

At first, the experimental raw data and KONTAS meteorological data are loaded to the MATLAB workspace. In the case of field measurements, KONTAS meteorological data must be extracted for the same time frame as transient experimental data and the sampling frequency must be identical. For laboratory measurements, a meteorological data set is not required.

Step 2

The user provides general information about the test evaluation, such as absorber temperature working point, angular frequency for the transient evaluation, date and time of test.

Step 3

Thermocouples are selected and allocated to the absorber, glass, outlet and inlet air temperatures, according to the experimental setup.

Step 4

Pyrometer analog signals, which are logged in [mA], are converted into temperature signals [°C], according to Eq. 3.6.

Step 5

The relevant excerpt of the recorded transient measurement data is selected for evaluation. In this step, the start point (start cut) is chosen close before the start of the ramp. Several end points (end cuts) are chosen in order to check the variability of the measurement results. During the second field measurement campaign (Section 6.3), the definition of end cutting points is selected automatically, in order to keep consistent between similar experiments. Fig. 5.3 shows the absorber and glass temperature signals measured by pyrometers. The start point and the five different end points are highlighted with lines. Five end cuts are set. Every time frame between the start point and each end point is evaluated independently.

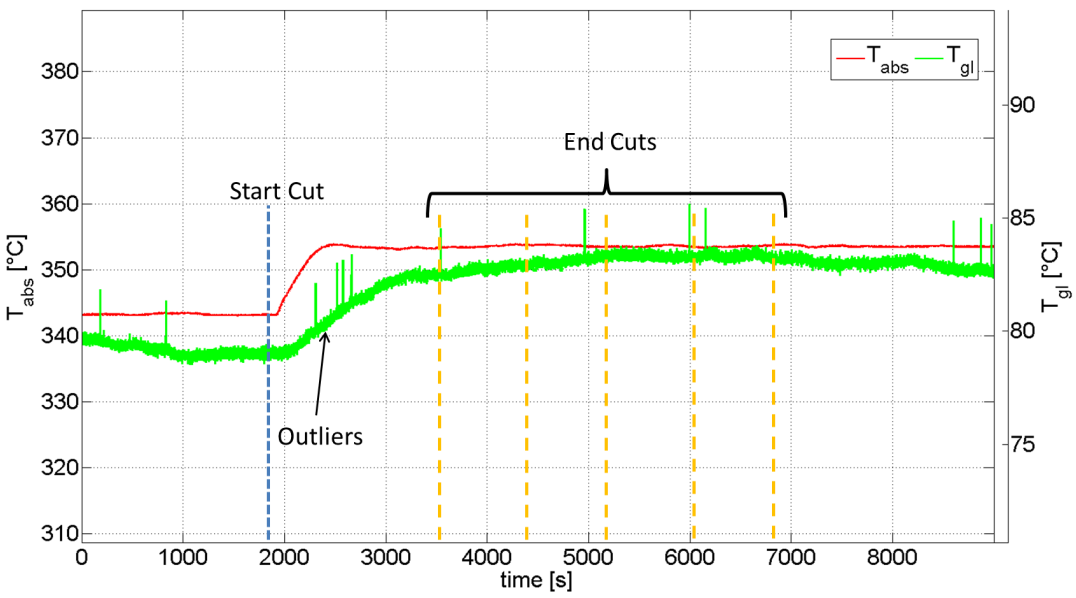

Figure 5.3: Example of start and end point selections for a transient measurement, Date of test: 05/05/2014, Ramp starts at 03:00 AM

Step 6

(a) After selecting start and end points, the transient experimental data is evaluated automatically. The time frames selected in Step 5 are extracted.

(b) The mean temperatures $\overline{T}_{abs}$, $\overline{T}_{gl}$ and $\overline{T}_{air}$ are derived. For ramp-and-hold measurements, $\overline{T}_{abs}$ and $\overline{T}_{gl}$ are calculated from the start and end temperatures. $\overline{T}_{air}$ is calculated for a complete time frame.

(c) Variations of the time frames selected in step 5 are defined by considering different start

and end cutting points. These variations help to prevent accidental cuts on outliers, as illustrated in Fig. 5.3 for the first end cut. Both temperature signals, the absorber and glass temperature, are normalized to the temperature at the start point, according to Eq. 5.1 and Eq. 5.2. This temperature is calculated averaging a short time frame before the start point. Then the normalized glass temperature signal is smoothed in order to remove outliers.

$$T_{abs,norm} = T_{abs}(t) - T_{abs}(t_{startcut}) \tag{5.1}$$

$$T_{gl,norm} = T_{gl}(t) - T_{gl}(t_{startcut}) \tag{5.2}$$

where: t_{endcut} = end cut of the evaluated time frame [s]
$t_{startcut}$ = start cut of the evaluated time frame [s]

(d) The script calculates amplitude ratio A and phase shift φ values for each time frame, using two different algorithms, which were developed in [Geller, 2012]. Both algorithms are based on the first-order lag model defined in Section 3.1.2 and approximate the corresponding transfer function.

In general, one can calculate the first-order lag element transfer function for any angular frequency. In order to compare the results derived in this report with previous researches in [Geller, 2012] or [Gaertner, 2013], throughout the work the chosen angular frequency will be $\omega = 2\pi/600$ rad/s .

(e) The glass temperature response corresponding to the derived values of A and φ are simulated with the results of both algorithms. The deviation to the actual glass temperature response is calculated. The simulated responses are compared graphically to the measured glass temperature signal.

(f) Finally, the results of the transient data evaluation and their standard deviations are exported for each time frame in an Excel sheet.

A list of the exported values is given in Table 5.2. The first group of documented results are the main temperatures. The second group includes the results obtained with the two algorithms used to derive A and φ. *AR algo - mean* and *PS algo - mean* correspond to the average values calculated for time frame variations extracted in step 6 (c). The standard deviations *AR algo - std* and *PS algo - std* correspond to the deviations among these variations. *AR algo - global* and *PS algo - global* correspond to the mean values aggregated from both algorithms.

The next group (3) lists information about the end cuts of the evaluated time frames. *CuttingPoint* indicates the elapsed time since the start of the measurement, while *CuttingPoint after ramp* shows the elapsed time in seconds since the start cutting point defined in step 5, and therefore the length

of the evaluated time frame. $T_{abs,norm}$ and $T_{gl,norm}$ correspond to the last temperature values in that time frame, normalized with respect to the start temperature (Normalization in Step 6 (c)).

The last group displays information about the accuracy of the algorithms simulating the first-order lag transfer function. *Delta Algo1* and *Delta Algo2* are the differences between the simulated first-order lag element transfer function using the values calculated by both algorithms and the measured glass temperature at the end cut of the time frame. *St.Dev. Algo1* and *St.Dev. Algo1* are the standard deviation between the simulated and the measured glass temperature signals

Table 5.2: List of extracted results from the data evaluation procedure

Name	Symbol	Unit	Description
Group 1: Mean temperatures			
AirTemp	$\overline{T}_{air}$	[°C]	Mean air temperature average between the radiation shield in- and outlet temperatures
AbsorberTemp	$\overline{T}_{abs}$	[°C]	Mean absorber temperature
GlassTemp	$\overline{T}_{gl}$	[°C]	Mean glass temperature
AmbTemp	$\overline{T}_{amb}$	[°C]	Mean ambient temperature
Group 2: Amplitude ratio and phase shift calculation			
AR algo1 - mean	A_{algo1}	[-]	Amplitude ratio calculated by algorithm 1
AR algo2 - mean	A_{algo2}	[-]	Amplitude ratio calculated by algorithm 2
AR global - mean	A_{global}	[-]	Amplitude ratio mean value
AR algo1 - std	$\sigma(A_{algo1})_{var}$	[-]	Standard deviation along time frame variations
AR algo2 - std	$\sigma(A_{algo2})_{var}$	[-]	Standard deviation along time frame variation
PS algo1 - mean	φ_{algo1}	[rad]	Phase shift calculated by algorithm 1
PS algo2 - mean	φ_{algo2}	[rad]	Phase shift calculated by algorithm 2
PS global - mean	φ_{global}	[rad]	Phase shift mean value
PS algo1 - std	$\sigma_{var}(\varphi_{algo1})$	[rad]	Standard deviation along time frame variations
PS algo1 - std	$\sigma_{var}(\varphi_{algo2})$	[rad]	Standard deviation along time frame variations
Group 3: End cutting point			
CuttingPoint	t_{endcut}	[s]	Time of EndCut regarding test time
CuttingPoint after ramp	$t_{timeframe}$	[s]	Duration of evaluated time frame
T_abs_norm	$T_{abs,norm}$	[°C]	Normalized absorber temperature at end cut
T_gl_norm	$T_{gl,norm}$	[°C]	Normalized glass temperature at end cut
Group 4: Quality of data evaluation			
Delta Algo1	ΔT_{algo1}	[K]	Difference between simulated and measured glass temperature signal at end cut by algorithm 1
Delta Algo2	ΔT_{algo2}	[K]	Difference between simulated and measured glass temperature signal at end cut by algorithm 2
St.Dev. Algo1	$\sigma(\Delta T_{algo1})$	[K]	Standard deviation between simulated and measured glass temperature signals by algo1
St.Dev. Algo2	$\sigma(\Delta T_{algo2})$	[K]	Standard deviation between simulated and measured glass temperature signals by algo2

To evaluate the quality of a transient measurement, the MATLAB script generate two plots in the data evaluation procedure. The first plot shows both pyrometer signals and compare the measured glass temperature response with simulated responses generated by first-order transfer function identification algorithms. Both temperature signals are normalized on their stationary temperature before the start of transient excitation. This first plot provides a graphical indication about the quality of the pyrometer measurements and the quality of the first-order lag system modelization. One example is illustrated in Fig. 5.2.1.

The second plot displays meteorological datas: wind velocity [m/s] at 5 m above ground, wind direction [°N] and ambient temperature [°C]. This second plot helps to identify potential environmental sources perturbing the transient measurement. One example is illustrated in Fig. 5.5.

With both plots, potential sources of disturbance on the glass temperature signal can be identified.

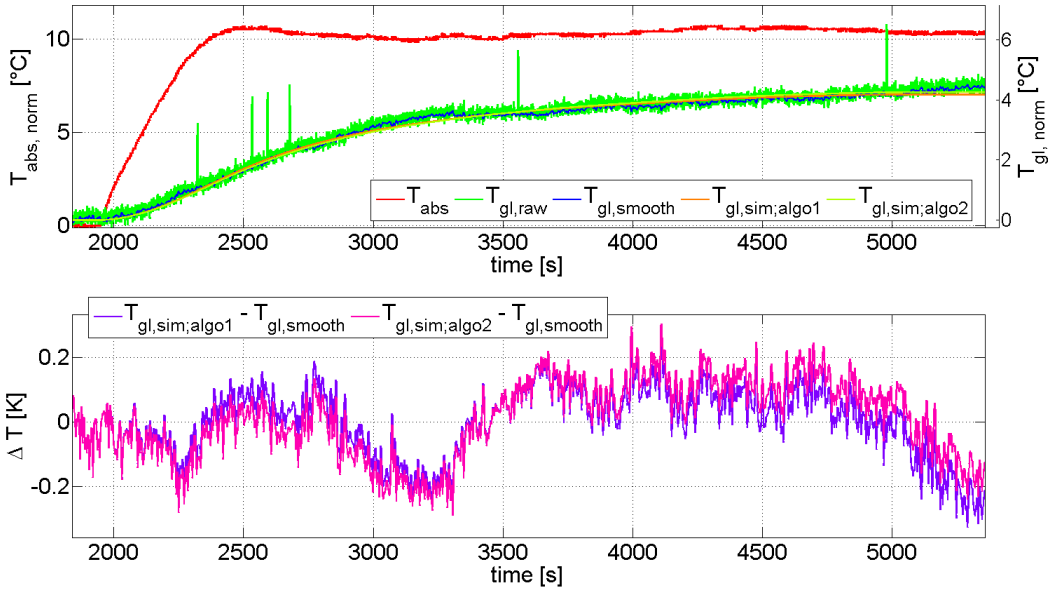

Figure 5.4: Measured in simulated temperature signal and deviation between measured and simulated signal, Date of test: 05/05/2014, Ramp starts at 03:00 AM

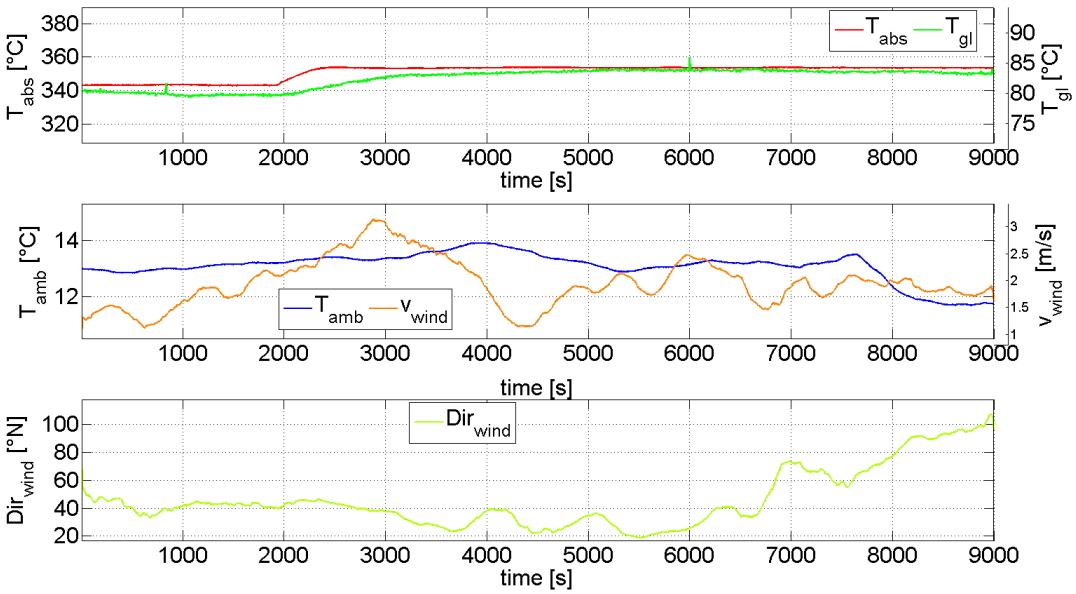

Figure 5.5: Measured absorber and glass temperature and meteorological data like wind direction, wind speed and ambient temperature, Date of test: 05/05/2014, Ramp starts at 03:00 AM

5.2.2 Assessment of the Data Evaluation Method

In order to assess the sensitivity of the data evaluation method and the quality of first-order lag element transfer function algorithms presented in the previous section, a quick simulation study was carried out. According to manufacturer specifications, both pyrometers are supposed to have a noise equivalent temperature difference (NETD) equal to ± 0.1 °C, (Table 4.1). However, the pyrometer *DT44LH* measuring the glass temperature tends to exhibit a greater NETD. The observed white noise standard deviation is around 0.1 °C to 0.15 °C. The aim of this simulation study is to check the influence of this deviation on the data evaluation procedure, especially on the derivation of A and φ. For this purpose, first-order lag transfer functions are simulated with certain A and φ values. In addition, a white noise is added on the temperature response signal. The outliers are copied from previous transient measurements and added to the simulated temperature response signal. Between every end cut, one outlier is placed. The different simulation scenarios are listed in Table 5.3. These simulated temperature signals are evaluated with the presented data evaluation procedure to derive corrupted A and φ. The difference between the expected A and φ values and the calculated A and φ values are plotted in Fig. 5.6 for both algorithms.

Table 5.3: Simulation scenarios for the simulated temperature response signal; φ = -1.41, A = 0.055

	1	**2**	**3**	**4**	**5**	**6**	**7**	**8**
Standard deviation of NETD	0	0	0.10	0.10	0.15	0.15	0.20	0.20
Outlier implemented	no	yes	no	yes	no	yes	no	yes

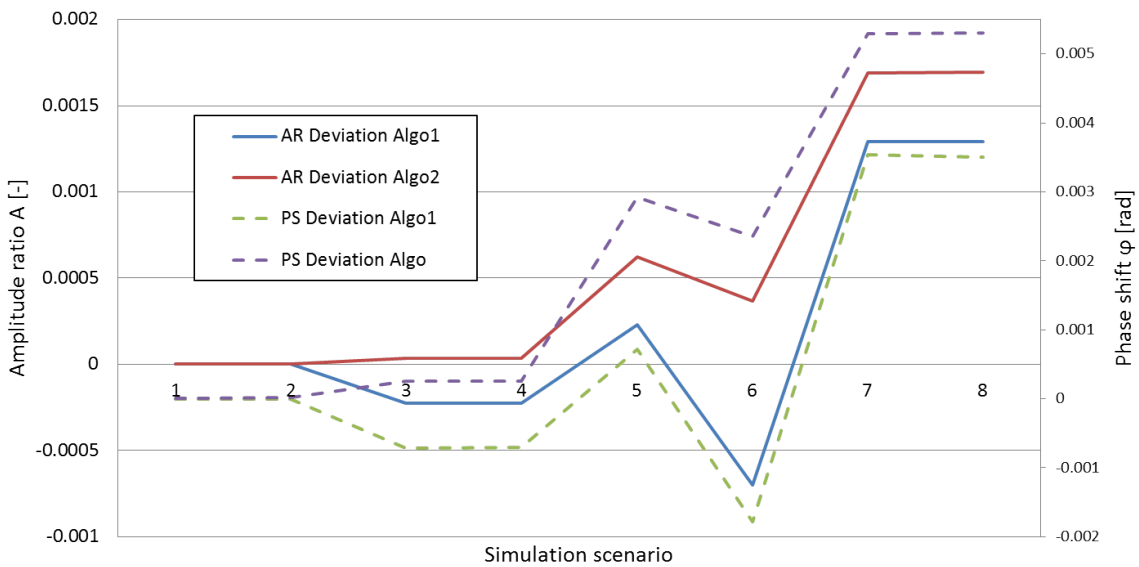

Figure 5.6: Influence of white noise and outliers on A and φ, according to the scenarios listed in Table 5.3

One can observe in Fig. 5.6 that in the absence of white noise (Scenarios 1 and 2), both algorithms derive the expected A and φ values. As the magnitude of white noise increases, the deviation between the A and φ values derived with data evaluation algorithms and the expected A and φ values increase. An uncertainty analysis presented in [Potzel, 2009] indicates that an uncertainty of 0.001 [-] for the amplitude ratio and an uncertainty of 0.01 rad for the phase shift imply a 6 % uncertainty on the UA_L value for the transient measurement principle (Eq. 2.13). For the scenarios listed in Table 5.3, the uncertainty threshold of 0.01 rad is not exceeded for the phase shift, while the uncertainty threshold of 0.001 can be exceeded for the amplitude ratio. The introduction of outliers does not seem to affect the data evaluation procedure. The deviation in A and φ values between both algorithms tend to increase as the white noise magnitude increases.

For small adapted white noise, it seems that the second algorithm of least square errors is more stable. Still both algorithms show an acceptable deviation with regards to the uncertainty thresholds. The analysis shows that the magnitude of the glass pyrometer white noise alone can be critical for the proper derivation of A and φ. This shows, that the magnitude of the white noise standard deviation should be monitored and not overrun 0.15 K.

6 Results and Discussion

6.1 First Field Measurements

First field measurements were proceeded in April and May 2014. Two absorber temperature working points were investigated, namely 300 °C and 350 °C. The objective of the first field campaign was to prove the practicability of the transient infrared thermography measurement principle, described in chapter 3. For the first time this measurement method was applied in the field. Potential difficulties have been detected and corrective actions have been developed.

First, the control parameters of the KONTAS temperature control unit were optimized. This optimization enabled to produce an absorber temperature excitation nearing a ramp-and-hold function and reduced overshoot and oscillations induced by the original PID control settings (See subsection 4.2.1).

At the beginning of this field measurement campaign, transient measurements were observed to be strongly influenced by ambient conditions, namely wind and ambient temperature variations.

6.1.1 Ambient Perturbations and Corrective Actions

6.1.1.1 Influence of Wind

Experimental Observations In the region of Tabernas, where the Plataforma Solar Almería is located, wind conditions can vary considerably during daytime, especially in the Spring. The initial openings on the radiation shield outlet represented a surface of 0.01131 m^2(See Table 4.2). These openings were made for the regulation of the radiation shield ventilation. Unfavorable wind conditions could perturb the ventilation process and thus the glass temperature measurements during transient experiments.

To reduce wind perturbation, wind screens were installed at the inlet and outlet of the radiation shield (See Fig. 4.5). These wind screens could only partially reduce wind perturbations.

One example of a wind perturbation can be seen in Fig. 6.1. In spite of wind screens, disturbances of the glass temperature profile could be attributed to the wind. The wind velocity is about 6 to 7 m/s, which is quite high. Furthermore, the main wind direction is around 100 °N, which means that the wind blows into the inlet of the radiation shield, which is aligned to 90 °N.

The transient glass temperature signal follows a typical first-order lag element response to the absorber temperature excitation, but the signal appears to be strongly perturbated with several irregular ripples. This kind of perturbation is problematic for the data evaluation procedure, as the glass temperature does not reach a clear equilibrium after the ramp.

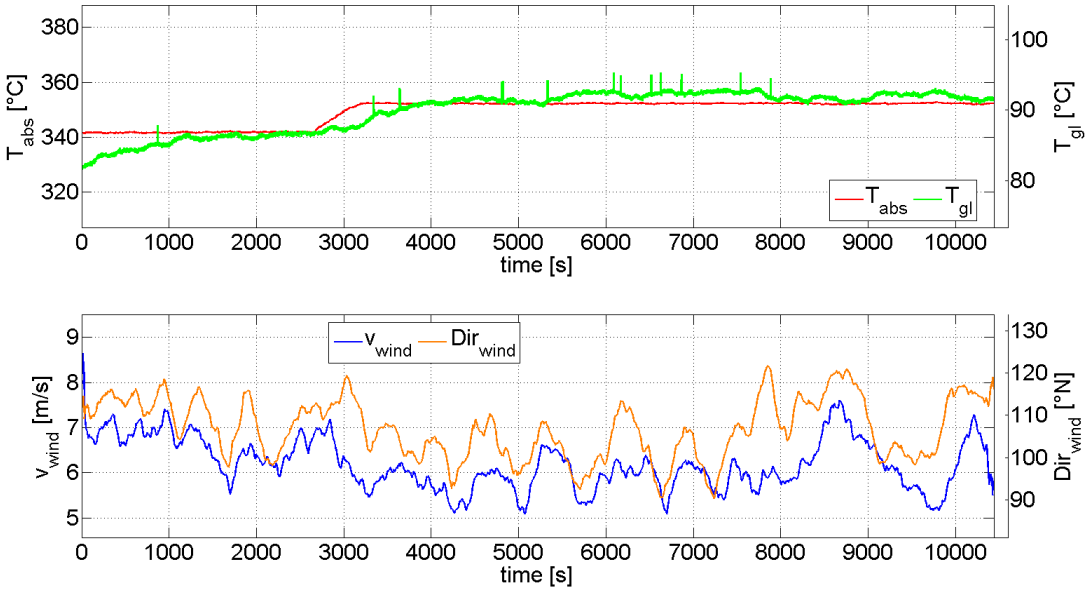

Figure 6.1: Influence of the wind on glass temperature. Date of test: 04/09/2014, Ramp starts at 01:00 PM

Table 6.1 displays the measurement results across five evaluated time frames. A continuously increasing deviation of the simulated response to the measured response can be observed. The calculated A and φ values differ across the time frames strongly.A high deviation is also observed between both algorithms. This deviation is as well displays Fig. 6.2. Among a high difference between simulated and measured response, the response profiles calculated by the algorithm results differ. The absolute difference between simulated and measured response shows a peak of more than 1 K at approximately 5250 s.

Table 6.1: Evaluation results of a transient measurement influenced by wind. Date of test: 04/09/2014, Ramp at 01:00 PM

Time frame	1	2	3	4	5
t_{endcut} [s]	4051.8	4551.8	5051.8	5551.8	6051.8
$t_{timeframe}$ [s]	1500	2000	2500	3000	3500
$\overline{T}_{abs}$[°C]	346.96	347.04	347.11	346.97	346.96
$\overline{T}_{gl}$[°C]	88.99	89.44	89.11	89.54	89.72
$\overline{T}_{amb}$[°C]	24.34	24.46	24.53	24.57	24.52
$T_{gl,norm}$[°C]	4.23	5.11	4.44	5.24	5.86
$\sigma_{algo1}(\Delta T_{gl})$ [K]	0.25	0.25	0.29	0.32	0.39
$\sigma_{algo2}(\Delta T_{gl})$ [K]	0.26	0.25	0.30	0.38	0.44
A_{algo1} [-]	0.0545	0.0611	0.0693	0.0738	0.0659
A_{algo2} [-]	0.0561	0.0556	0.0641	0.0592	0.0540
φ_{algo1}[rad]	-1.502	-1.467	-1.433	-1.415	-1.443
φ_{algo2}[rad]	-1.481	-1.483	-1.440	-1.452	-1.476

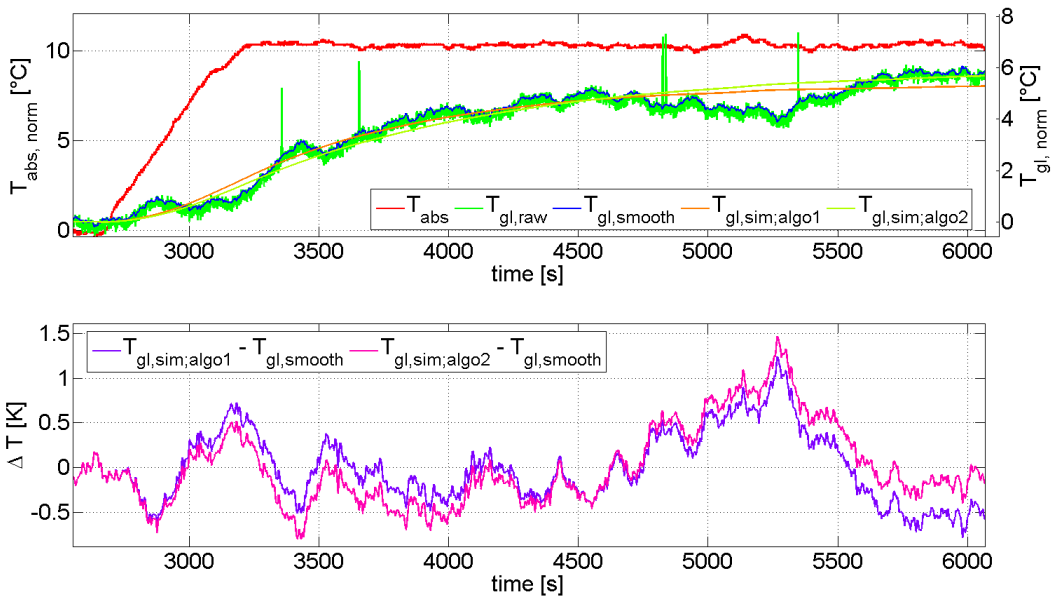

Figure 6.2: Comparison between measured and simulated glass temperature response for a wind influenced measurement. Date of test: 04/09/2014, Ramp starts at 01:00 PM

Corrective action In order to reduce wind perturbations more efficiently, a proper wind screen was constructed. The idea is to scale down the holes on the radiation shield outlet. Smaller openings cause a higher pressure drag on the air flow within the radiation shield. To maintain a similar air speed inside the radiation shield, the ventilation power has to be increased.

For the first wind screen construction, the radiation shield outlet was covered with a foam (Fig. 6.3 (a)) and the diameter of the holes was reduced from 60 mm to 8 mm. With this configuration, the pressure drag was observed to be too high. Without a proper air flow, heat builds up inside of the radiation shield. The glass temperature does not respond when the fan power increases. With increasing fan supply power, higher air velocities are expected. Higher air velocities induces higher convective heat transfer coefficients on the glass surfaces and by this the glass temperature decreases. If the glass temperature does not respond to a increasing fan power supply, the pressure drag is too high due to the small opening at the outlet and the air velocity does not increase.

For the next wind screen construction, the diameter of the holes was increased from 8 mm to 25 mm (Fig 6.3 (b)). Comparing the glass temperature response to the original settings, a temperature lift around 5.5 K was observed. The glass temperature decreases corresponding to a higher power. Shifting the fan supply current from 350 mA to 600 mA, the measured glass temperature response approached the glass temperature response without wind screen.

(a) Hole diameter: 8 mm (b) Hole diameter: 25 mm

Figure 6.3: First wind screen construction installed on the radiation shield outlet

The influence of wind perturbations on the glass temperature is significantly reduced with this wind screen construction, as illustrated in Fig. 6.4. In this example, wind conditions are comparable to wind conditions on April 4th (Fig. 6.1). The glass temperature response remains stable, even

with wind velocities above 6 m/s blowing in the direction of the radiation shield inlet. The wind perturbation appears again when the wind velocity exceeds 8 m/s.

The influence of wind on the glass temperature still strongly depends on the wind direction. The wind perturbation effect was observed to be significantly more dominant, when the wind blows into the radiation shield outlet (outlet direction: 270 °N). All in all, the maximum wind velocity should not exceed 6 m/s to perform a transient measurement that is not disturbed by wind.

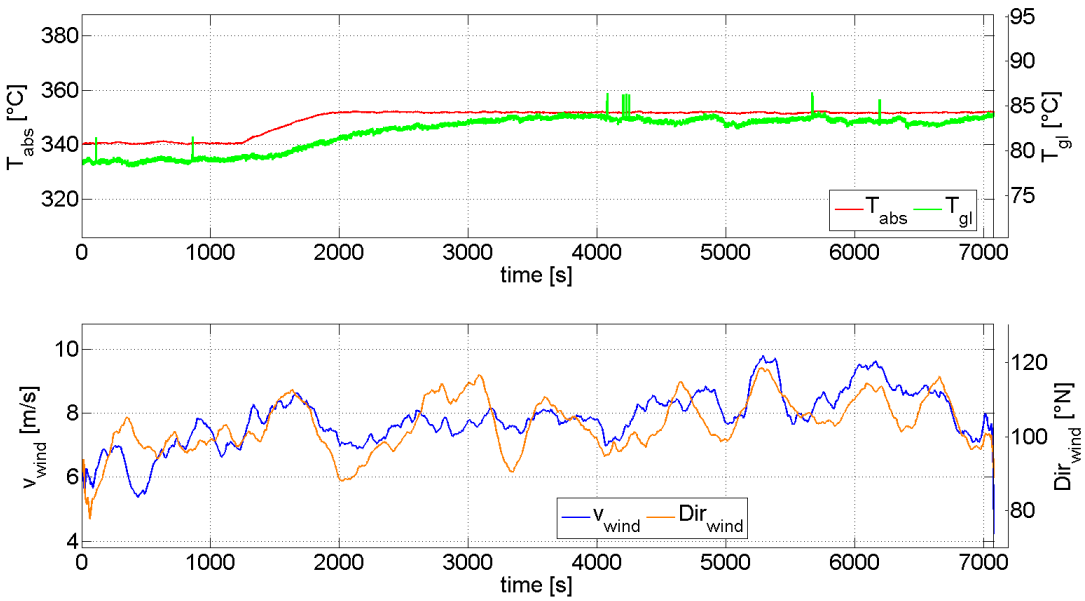

Figure 6.4: Influence of the wind on glass temperature with mounted wind screen. Date of test: 05/15/2014, Ramp starts at 01:15 PM

Analyzing historical meteorological data, strong winds tend to appear mostly in the late afternoon and early evening. The wind velocity is observed to be very low during nights and between 5 AM and 8 AM in the morning. Night measurements were accordingly planned.

Measurements perturbated by wind can still be processed to derive an amplitude ratio A and phase shift φ. The glass temperature response follows the predicted course among the different selected time frames. If wind perturbations become significant, the indicators introduced in Section 5.2, such as standard deviations between measured and simulated glass response, can help detect a suspicious transient measurement.

A wind perturbation causes a strong fluctuation of the glass temperature profile. A rule of thumb can be defined with respect to the standard deviation between the simulated and measured glass temperature signals: the *St.Dev. Algo1* ($\sigma_{algo1}(\Delta T_{gl})$) and *St.Dev. Algo2* indicator ($\sigma_{algo2}(\Delta T_{gl})$) (Table 5.2) should not exceed 0.2 K and the *Delta Algo1* (*Delta Algo2*) temperature difference should not exceed 0.4 K at any time, which can monitored by the graphically comparison. Otherwise, the

derivation of A and φ cannot be considered reliable for such a measurement.

6.1.1.2 Ambient Temperature Variations

Experimental Observations In the absence of wind, it could be further observed that ambient temperature variations could influence the glass temperature response.

The influence of the ambient temperature on the glass temperature is such, that a deviation of more than 1 K during a transient measurement can significantly impact the measurement evaluation. Based on simulations, it was estimated that a 1 K ambient temperature variation leads to a glass temperature variation of 0.9 K, for the type of investigated PTR (See Subsection 4.1.5).

One example of such a perturbation is shown in Fig. 6.5. The ambient temperature falls continuously after sunset. The glass temperature follows this pattern, even after the absorber temperature excitation. Even though the absorber excitation shows effect on the glass temperature, the glass temperature response deviates from the expected response pattern derived from a first-order lag transfer function.

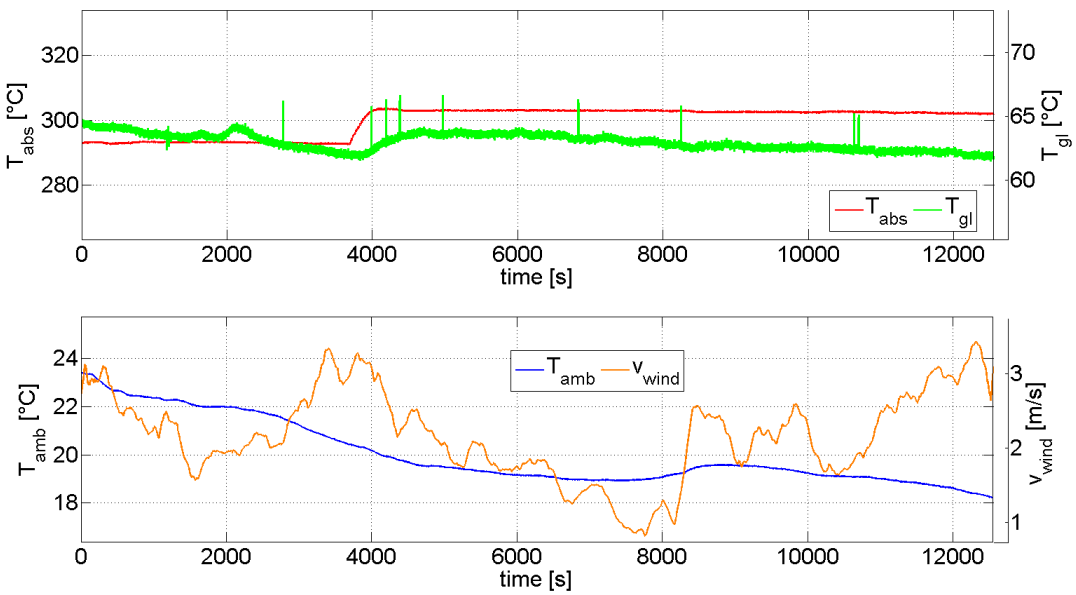

Figure 6.5: Influence of the ambient temperature on the glass temperature, Date of test: 05/07/2014, Ramp starts at 09:00 PM

If the glass temperature response is influenced by ambient temperature variations, the data evaluation indicators introduced in Section 5.2 do not necessarily help to detect this perturbation. The evaluation results of the five different time frames for the example in Fig. 6.5 are presented in Table 6.2. Among the different time frames, the simulated glass response fits quite well the measured

glass temperature response. The standard deviations between simulated and measured temperature responses are small, although increasing for larger time frames. Both algorithm results are close to each other.

Table 6.2: Evaluation results of a transient measurement influenced by temperature gradients. Date of test: 05/07/2014, Ramp at 09:00 PM

Time frame	**1**	**2**	**3**	**4**	**5**
t_{endcut} **[s]**	5531.8	6031.8	6531.8	7031.8	7531.8
$t_{timeframe}$ **[s]**	2000	2500	3000	3500	4000
$\overline{T}_{abs}$**[°C]**	297.86	297.94	297.85	297.92	297.88
$\overline{T}_{gl}$**[°C]**	62.95	63.12	63.51	62.94	62.91
$\overline{T}_{amb}$**[°C]**	20.76	20.53	20.28	20.13	19.96
$T_{gl,norm}$**[°C]**	1.51	1.73	2.42	1.60	1.33
$\sigma_{algo1}(\Delta T_{gl})$ **[K]**	0.16	0.16	0.26	0.28	0.29
$\sigma_{algo2}(\Delta T_{gl})$ **[K]**	0.16	0.16	0.27	0.28	0.29
A_{algo1} **[-]**	0.0305	0.0311	0.0253	0.0230	0.0265
A_{algo2} **[-]**	0.0316	0.0296	0.0232	0.0252	0.0237
φ_{algo1}**[rad]**	-1.386	-1.375	-1.432	-1.454	-1.424
φ_{algo1}**[rad]**	-1.376	-1.398	-1.467	-1.436	-1.438

For the evaluation of the perturbation on the measurement, only the comparison between the different time frames of evaluation can help. The glass temperature lift $T_{gl,norm}$ at the end of the time frame must not in- or decrease significantly, when the glass temperature is supposed to stabilize (approx. at 2500 s after excitation start). The effect of a perturbing ambient temperature variation will also be observable on A and φ values between the different time frames. In this example, the amplitude ratio A decreases for longer time frame, while the phase shift magnitude also increase. If the measurement was not perturbated, A and φ values should remain consistent for the different time frames.

Corrective Actions To handle the influence of an ambient temperature variation on the glass temperature, a first-order glass temperature correction is investigated for the measurement post-processing. The idea is that the effect of the ambient temperature variation on the glass temperature is overlapped to the glass temperature response and can be subtracted. If a linear temperature gradient is observed, the glass temperature response is expected to include this pattern. By numerical simulation, the ratio $\frac{\Delta T_{gl}}{\Delta T_{amb}}$ between the glass temperature gradient and the ambient temperature gradient is estimated to 0.9.

Looking at the measurement data, the linear ambient temperature gradient is identified manually between the instants t_0 and t_1, which are respectively the start and the end time of the ambient temperature shift. The glass temperature signal is corrected according to Eq. 6.1.

$$T_{gl,corrected}(t) = \begin{cases} T_{gl}(t) & if\, t < t_0 \\ T_{gl}(t) + \frac{\Delta T_{amb}}{t_1 - t_0} \cdot 0.9 \cdot (t - t_0) & if\, t_0 \geq t \geq t_1 \\ T_{gl}(t) + \frac{\Delta T_{amb}}{t_1 - t_0} \cdot 0.9 \cdot t_1 & if\, t_1 < t \end{cases} \tag{6.1}$$

If the ambient temperature shows more than one significant gradient, several temperature corrections are applied in a row.

To evaluate the correction graphically, the ambient temperature is corrected by the addition of its own gradient (Eq. 6.2). By plotting the corrected ambient temperature profile it can be monitored graphically, if a reasonable time frame to extract a ambient temperature shift gradient was chosen and the ambient variation decreased by the correction.

$$T_{amb,corrected}(t) = \begin{cases} T_{amb}(t) & if\, t < t_0 \\ T_{amb}(t) + \frac{\Delta T_{amb}}{t_1 - t_0} \cdot (t - t_0) & if\, t_0 \geq t \geq t_1 \\ T_{amb}(t) + \frac{\Delta T_{amb}}{t_1 - t_0} \cdot t_1 & if\, t_1 < t \end{cases} \tag{6.2}$$

Fig. 6.6 shows an example of the applied correction method. Until approximately 7000 s of measurement, the ambient temperature decreases rapidly. Three ambient temperature gradients are defined and three corresponding corrections are applied, corresponding to Table 6.3.

Table 6.3: Chosen time frames to extract an ambient temperature gradient. Date of test: 05/07/2014, Ramp starts at 09:00 PM

	t_0	t_1
1st gradient	0 s	2050 s
2nd gradient	2100 s	4900 s
3rd gradient	5000 s	7250 s

On the first subplot, it can be observed that the glass temperature profile is rectified with the applied ambient temperature correction. The second subplot shows the difference between the original and corrected glass temperature signals and the difference between the original ambient temperature and the ambient temperature subtracted by the gradient. The corrected glass temperature can now be evaluated with respect to the absorber temperature excitation starting at 4000 s, according to the first order lag model.

The evaluation results of the corrected measurement are presented in Table 6.4. Although the normalized glass temperature lift increases over the considered time frames, the comparison of A and φ values between time frames is not significantly better in comparison to Table 6.2. While the standard deviation of φ, evaluated over the different time frames, decreases from 0.032 for the original measurement to 0.020 for the corrected measurement, the standard deviation of A decreases

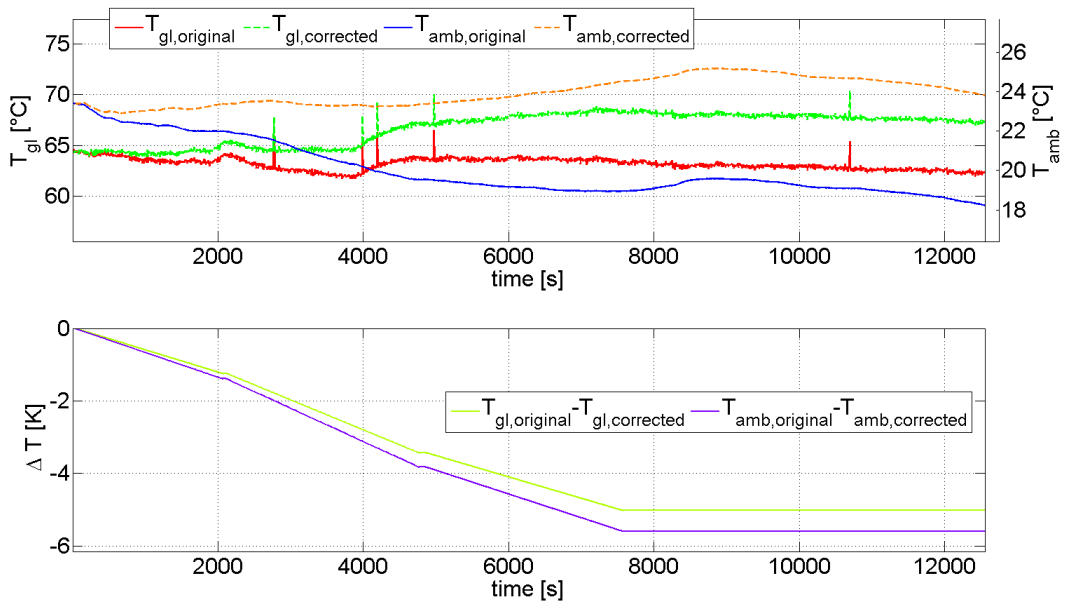

Figure 6.6: Ambient temperature correction applied to the glass temperature. Date of test: 05/07/2014, Ramp starts at 09:00 PM

from 0.0038 to 0.0033. The fitting of the simulated results to the glass temperature, indicated by $\sigma_{algo}(\Delta T)$, improves clearly for the later evaluation time frames. Still, the significant difference between time frame 1 and 2 to the other frames still exists. A overlap of the temperature excitation response on the one hand and the perturbation by the ambient temperature shift can not be eliminated.

The applied ambient temperature correction method does not fully contribute to an improvement of the evaluation results. Accordingly, the influence of ambient temperature variations on the glass temperature response remain critical. If the ambient temperature variation is higher than 1 K during the transient measurement, the measurement remains suspicious.

Table 6.4: Evaluation results of a transient measurement with ambient temperature corrections. Date of test: 05/07/2014, Ramp starts at 09:00 PM

Time frame	1	2	3	4	5
t_{endcut} [s]	5531.8	6031.8	6531.8	7031.8	7531.8
$t_{timeframe}$ [s]	2000	2500	3000	3500	4000
$\overline{T}_{abs}$[°C]	297.86	297.94	297.85	297.92	297.88
$\overline{T}_{gl}$[°C]	66.07	66.34	66.47	66.42	66.54
$T_{gl,norm}$[°C]	2.90	3.45	3.64	3.77	3.75
$\sigma_{algo1}(\Delta T_{gl})$ [K]	0.11	0.12	0.14	0.16	0.18
$\sigma_{algo2}(\Delta T_{gl})$ [K]	0.11	0.13	0.15	0.16	0.19
A_{aglo1} [-]	0.0472	0.0447	0.0366	0.0338	0.03665
A_{aglo2} [-]	0.0473	0.0417	0.0331	0.0375	0.0379
φ_{aglo1}[rad]	-1.395	-1.411	-1.459	-1.475	-1.460
φ_{aglo2}[rad]	-1.396	-1.433	-1.484	-1.457	-1.452

6.1.2 Experimental Results

Applying the wind shields on the inlet and outlet of the radiation shield, described in Section 6.1.1.1, 10 tests were proceeded at the absorber temperature working point of 300 °C. 5 tests can be considered not to be influenced by ambient conditions. The other 5 tests are discarded, as they are significantly influences by ambient conditions and not analyzable with the presented data evaluation procedure. 10 tests were also proceeded at an absorber temperature working point of 350 °C. 6 of these tests were not heavily influenced by ambient conditions. The experiments results are presented in Table 6.6. The evaluated tests show a high standard deviation for the A and φ values between the experiments. In addition to a low ratio of analyzable tests, which are not too high influenced by ambient conditions, there is a high failure of tests because of technical issues related with KONTAS temperature control unit, communication with the data acquisition system or programming errors. A test log of the measurements can be found in Appendix D.

Table 6.5: Experimental results of the first field measurement campaign after the application of wind screen; 04/08/14 - 05/14/2014

	WP 300		WP 350	
Number of tests	5		6	
	Average	σ	**Average**	σ
$\overline{T}_{abs}$ [°C]	297.92	0.51	347.56	0.71
$\overline{T}_{gl}$ [°C]	61.71	1.54	82.39	3.31
$\overline{T}_{amb}$ [°C]	21.15	9.55	20.75	6.08
A [-]	0.0425	0.0074	0.0640	0.0097
φ[rad]	-1.455	0.020	-1.426	0.0203

The improvement of the proper wind screen allowed to reduce the number of tests discarded because of wind perturbations. The ratio of analyzable transient measurements still remained low, because of the ambient temperature variation effects. This influence was not clearly identified before the installation of wind screens and the experiments were not planned accordingly in time windows with lower risk of ambient temperature variation. The measurement results are presented in Table 6.6. The standard deviation for the A and φ values between the experiments could be decreased. The average for both values increased slightly, which could be explained with the change of the experimental setup regarding the proper wind shield.

Table 6.6: Results of the second part of the first field campaign, using the provisional wind screen, 04/08/14 - 05/13/14

	WP 300		**WP 350**	
Number of tests	2		3	
	Average	σ	**Average**	σ
$\overline{T}_{abs}$ **[°C]**	297.35	0.08	345.82	0.02
$\overline{T}_{gl}$ **[°C]**	63.50	0.71	75.38	0.07
$\overline{T}_{amb}$ **[°C]**	20.60	0.53	16.26	0.07
A [-]	0.0521	0.0027	0.0687	0.0020
φ**[rad]**	-1.428	0.005	-1.387	0.01

After the first field measurement campaign, the focus was set on the 350 °C working point, in order to gain more significant statistics.

At the end of the first field measurement campaign, some irregularities were observed in the pyrometer glass temperature signal. The measured infrared glass temperature was observed to drop before a ramp or oscillate in the stationary regime. These effects could not be explained by analyzing available meteorological data or comparing the infrared temperature measurement with the corresponding thermocouple readings.

6.2 Laboratory Measurements

Laboratory measurements were carried out after the first field measurement campaign in order to test and develop the wind screen installed on the radiation shield outlet and investigate its impact on the measurands. Also the measurement devices could be checked. Furthermore, these measurements were not influenced by ambient conditions and the perturbations described in the previous section. By this, further observations could be made for the transient measurement method.

6.2.1 Wind Screen Construction

The wind screen constructed for the field measurement campaign was replaced by a new wind screen made of a steel sheet. The effect of this screen was investigated under laboratory conditions.

The new wind screen is built out of a 2 mm thick sheet of steel. The dimensions of the wind screen are listed in Table 6.7. The wind screen is fitted to the outlet of the radiation shield. To avoid scratches on the PTR surface, the inner edge of the wind screen is insulated with glass fiber. 16 holes with a diameter of 17 mm are drilled in this wind screen. The total area is 0.00272 m^2, which is exposed to wind. This area is similar to the area of the last wind screen built for the first field measurements. The new wind screen is shown in Fig. 6.7, mounted on the radiation shield outlet.

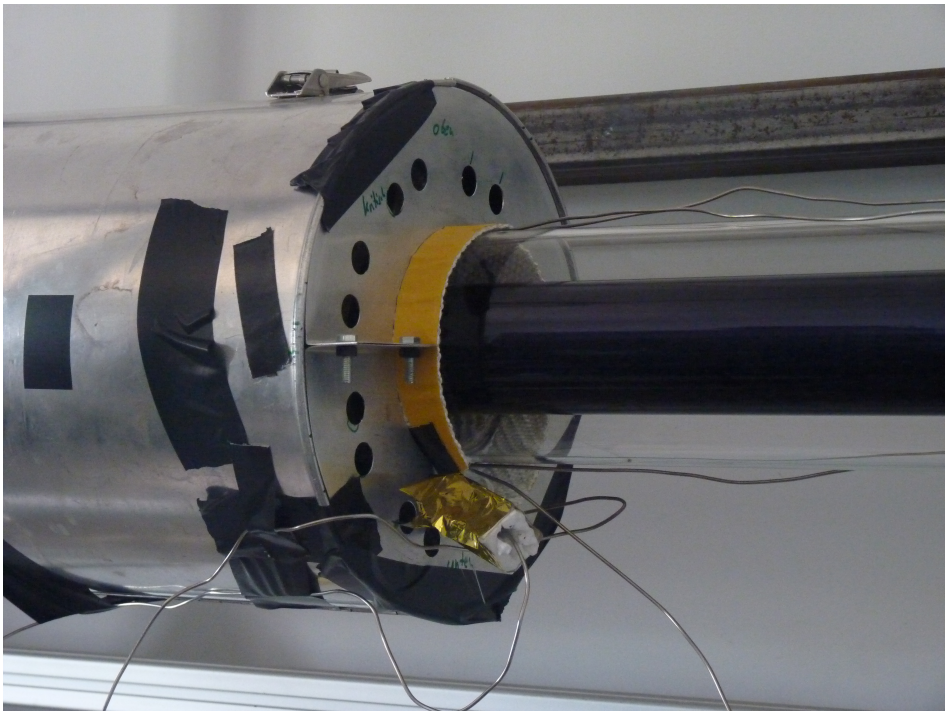

Figure 6.7: Wind screen mounted on the radiation shield during laboratory experiments

Table 6.7: Dimensions of the wind screen

Outer diameter [mm]	Inner diameter [mm]	Number of holes	Holes diameter [mm]	Total opening area [m^2]
290	128	16	17	0.00272

The task was to adjust the air flow of the radiation shield ventilation with the new wind screen. Several measurements were made with different settings for the fan power supply. According to simulations, the magnitude of the phase shift φ decreases with increasing air velocity, while the amplitude ratio A should not be affected significantly [Roeger et al., 2014].

6.2.2 Experimental Results

6.2.2.1 Measurements with Original Experimental Setup

Results Three transient measurements were carried out with the original experimental setup with the conditions presented in Section 4.3. The irregularities observed with the glass pyrometer under field conditions were not observed under laboratory conditions.

The exemplary results of one evaluated transient measurement under laboratory conditions are presented in Table 6.8. The glass temperature responses measured under laboratory conditions are significantly more consistent in comparison to first field measurements. This is confirmed by the standard deviation indicators calculating the deviation between simulated and measured glass temperature responses. An exemplary glass temperature response is illustrated in Fig. 6.8. The simulated responses using the two different algorithms deliver similar averaged A and φ values over the different selected time frames. The standard deviation indicator $\sigma_{algo1}(\Delta T_{gl})$ / $\sigma_{algo2}(\Delta T_{gl})$ is always lower than 0.1 K for laboratory experiments. The algorithms do not show a high difference between their results.

The ambient temperature is highly stable using the air conditioning and thus the effect on the glass temperature is eliminated.

Table 6.8: Evaluation results of a transient measurement under laboratory conditions. Date of test: 06/19/2014, 3rd test

Time frame	**1**	**2**	**3**	**4**	**5**
t_{endcut} [s]	2518.8	3018.8	3518.8	4018.8	5514.8
$t_{timeframe}$ [s]	2000	2500	3000	3500	4000
$\overline{T}_{abs}$[°C]	350.09	349.96	349.84	349.77	349.66
$\overline{T}_{gl}$[°C]	75.62	75.66	75.55	75.52	75.56
$\overline{T}_{air}$[°C]	26.23	26.27	26.27	26.27	26.27
$T_{gl,norm}$[°C]	3.60	3.76	3.57	3.50	3.52
$\sigma_{algo1}(\Delta T_{gl})$ [K]	0.06	0.05	0.06	0.06	0.06
$\sigma_{algo2}(\Delta T_{gl})$ [K]	0.06	0.06	0.07	0.07	0.06
A_{algo1}) [-]	0.0621	0.0612	0.0618	0.0625	0.0624
A_{algo2} [-]	0.0635	0.0632	0.0644	0.064	0.064
φ_{algo1}[rad]	-1.402	-1.407	-1.404	-1.401	-1.401
φ_{algo1}[rad]	-1.399	-1.401	-1.395	-1.394	-1.396

Laboratory measurements carried out with the original setup deliver a low uncertainty for A and φ, as described in Table 6.9. The reproducibility of experiments is demonstrated for the original setup.

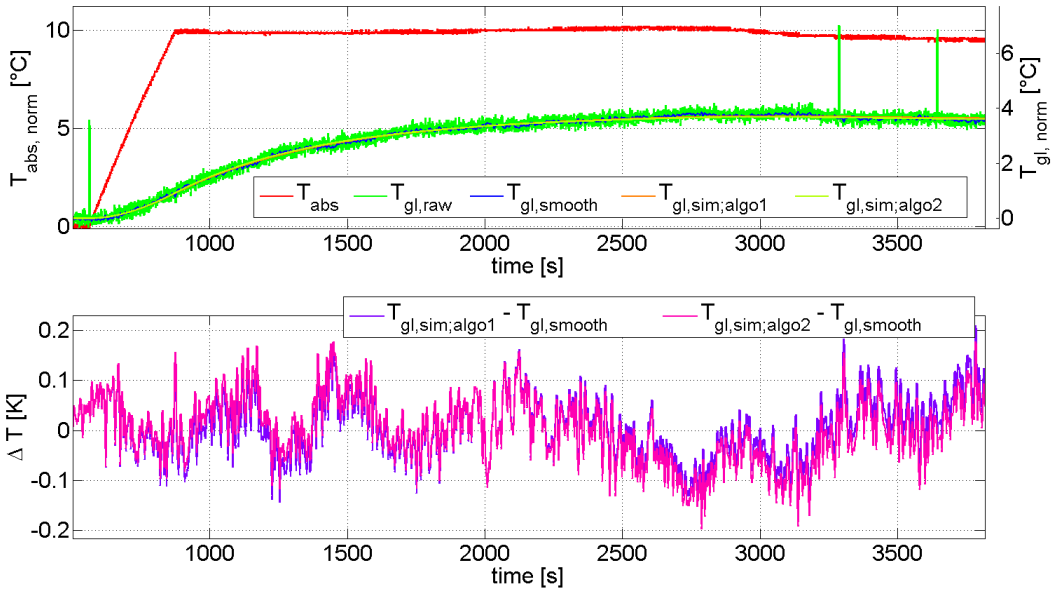

Figure 6.8: Comparison between measured and simulated glass temperature responses for a laboratory measurement. Date of test: 06/19/2014, 3rd test

Table 6.9: Results of laboratory measurements with the original experimental setup

Number of tests	3	
	Average	σ
$\overline{T}_{abs}$ [°C]	349.56	0.34
$\overline{T}_{gl}$ [°C]	75.12	0.19
$\overline{T}_{air}$ [°C]	25.92	0.23
$\overline{T}_{amb}$ [°C]	22.21	0.25
A [-]	0.0631	0.0005
φ[rad]	-1.395	0.004

The measurement results shown in Table 6.9 are compared with previous laboratory measurements [Gaertner, 2013] in Table 6.10. It is worth noticing that the standard deviations of measurands are lower for the recent laboratory measurement campaign, especially for the amplitude ratio A. The differences between the average of A and φ can origin from the slightly different working point.

Table 6.10: Results of laboratory measurement compared with results of proceeding work (Original Data - Standard Receiver - Ramp Measurements; [Gaertner, 2013])

	Laboratory measurements		**Previous Measurment [Gaertner, 2013]**	
	Average	σ	**Average**	σ
$\overline{T}_{abs}$ [°C]	349.57	0.35	364.27	2.25
$\overline{T}_{gl}$ [°C]	75.12	0.19	87.10	1.93
$\overline{T}_{amb}$ [°C]	22.21	0.23	28.8	3.42
A [-]	0.0659	0.0005	0.0628	0.0021
φ**[rad]**	-1.391	0.004	-1.427	0.008

It is worth noting that the data evaluation method has been slightly changed between both measurement campaigns. For the new measurement set, additional time frames were considered for the evaluation in order to check further the stability of A and φ values. Before, a variation of time frames were done around the manually set end cut.

Further Observations Different combinations of A and φ values exist, which give similar glass temperature responses during the first 2000 s after the beginning of the excitation. This could be observed in details during laboratory measurements. As the glass temperature is not influenced by ambient temperature variations, this effect has to be related to the data evaluation procedure.

To monitor the consistency of A and φ values during one test, 8 time frames were evaluated, beginning from 500 s after the start of the temperature excitation and continuing in intervals of 500 s. For the first evaluated time frame (500 s), the identified values of A and φ were not consistent among measurements, as observed in Fig. 6.9. As the span of the time frame increases, A and φ converge to consistent levels.

Based on this knowledge, all transient measurements are evaluated for time frames ranging from 2000 to 4000 seconds after the beginning of the temperature excitation.

6.2.2.2 Measurements with Wind Screen

The measurement results with the wind screen presented in Section 6.2.1 are presented for different fan power supply currents in Fig. 6.10. The phase shift value φ tends to increase as the fan supplied power increases, while the amplitude ratio remains nearly constant. In addition, the mean glass temperature decreases with increasing fan power, what proves the higher air velocity with higher fan power (Fig. 6.10 (b)). This confirms that the air velocity inside the radiation shield increases with higher fan power.

The results obtained with the new wind screen at the highest stable fan power setting (650 mA) are the most similar to the previous laboratory measurements with the original setup (See Table 6.11).

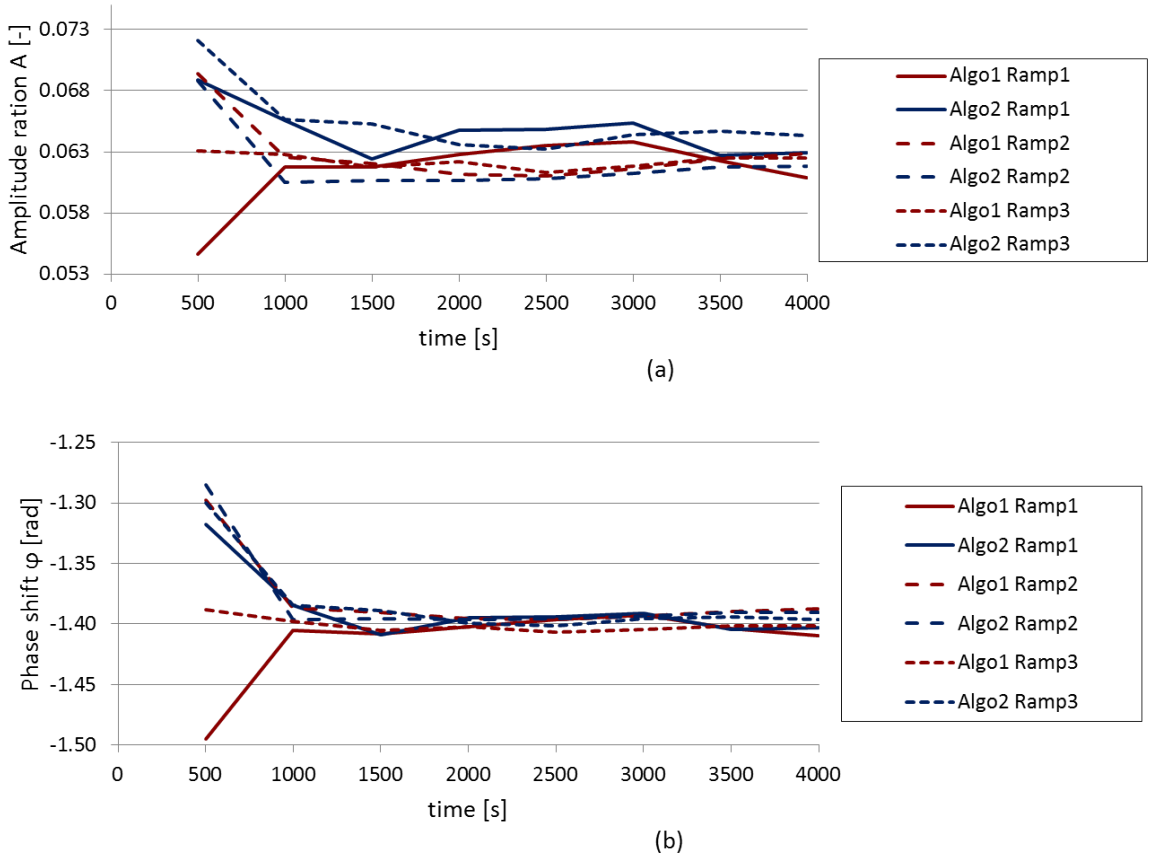

Figure 6.9: Calculated (a) amplitude ratio A and (b) phase shift φ for different time frames ranging from 500 s up to 4000 s after the excitation

This setting is hence defined for further field measurements with the wind screen in order to minimize the influence of wind perturbations on the glass temperature. There is still a difference of 5 K for the glass temperature. The means, the wind screens causes a higher heat build up inside the radiation shield.

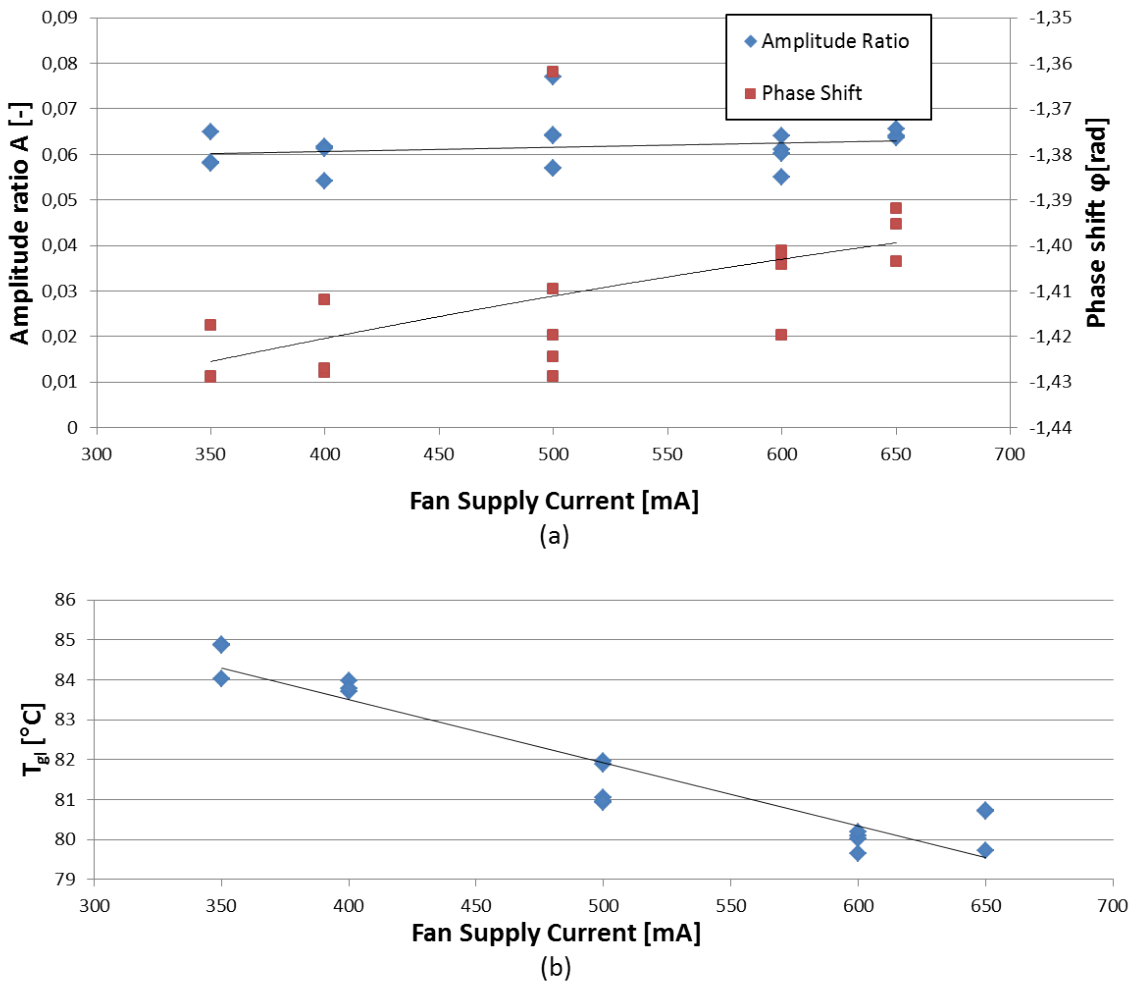

Figure 6.10: A and φ values (a) and glass temperature (b) with the wind screen as function of the fan supply current under laboratory conditions

Table 6.11: Comparison between laboratory measurement results obtained with wind screen and optimal fan power setting and original experimental setup

	With new wind screen		**Original experimental setup**	
i_{fan} **[mA]**	650		350	
	Average	σ	**Average**	σ
$\overline{T}_{abs}$ **[°C]**	348.74	0.36	349.57	0.35
$\overline{T}_{gl}$ **[°C]**	80.39	0.47	75.12	0.19
$\overline{T}_{amb}$ **[°C]**	24.24	0.80	22.21	0.23
$\overline{T}_{air}$ **[°C]**	28.20	0.57	25.92	0.23
$T_{gl,norm}$ **[°C]**	3.60	0.14	3.40	0.16
A [-]	0.0644	0.0009	0.0659	0.0004
φ **[rad]**	-1.397	0.005	-1.391	0.004
$\sigma_algo(\Delta T_{gl})$ **[°C]**	0.07	0.01	0.06	0.01

Using the average measurand values derived from laboratory measurements with the wind screen at the optimal fan power setting, the PTR thermal properties are identified using a numerical model, as described in Section 3.1.2. The estimation of h_{ann} and ϵ_{abs} parameters are:

$$\begin{aligned} h_{ann} &= 0.0039\ W/(m^2 \cdot K) \\ \epsilon_{abs} &= 12.15\ \% \end{aligned}$$

With these thermal properties, the PTR specific heat loss can be derived at the corresponding absorber temperature for standard laboratory conditions (T_{amb} = 25 °C, v_{wind} = 0.0). The estimated specific heat loss with the given measurands uncertainties is:

$$\dot{q}'_{loss} = 206.6 \pm 8.1\ W/m$$

This estimation can be compared with a previous steady-state specific heat loss measurement (Section 2.2.4): 198.5 ± 7.5 W/m. The transient heat loss measurement deviates from the steady-state heat loss measurement by 8.1 W/m (4.1 %) and has a similar uncertainty.

6.3 Additional Field Measurements

The additional field measurement campaign was carried out at the beginning of September 2014. The experimental setup described in Section 4.2.3 was implemented for this measurement campaign. The objective was to test the wind screen under field conditions and collect more consistent measurement results.

To avoid the influence of an ambient temperature shift, the local climatic situation was studied closely by analyzing the meteorological conditions of previous days. In contrast to the first field measurement campaign, where time windows with high probability of wind were avoided, time windows with high probability of stable ambient temperature were chosen for this new field campaign. Additional time windows with expected stable ambient temperature gradients were also chosen to check the validity of the glass temperature correction method described in Section 6.1.1.2.

6.3.1 Ambient Perturbations

During the additional field measurement campaign, unfavorable wind conditions with wind velocities up to 8 m/s were observed for some tests. No significant influence on the glass temperature

could be observed. One example is presented in Fig. 6.11. Besides of high wind velocities, the wind direction is critical as the wind faces the radiation shield outlet with an average direction of 260 °N.

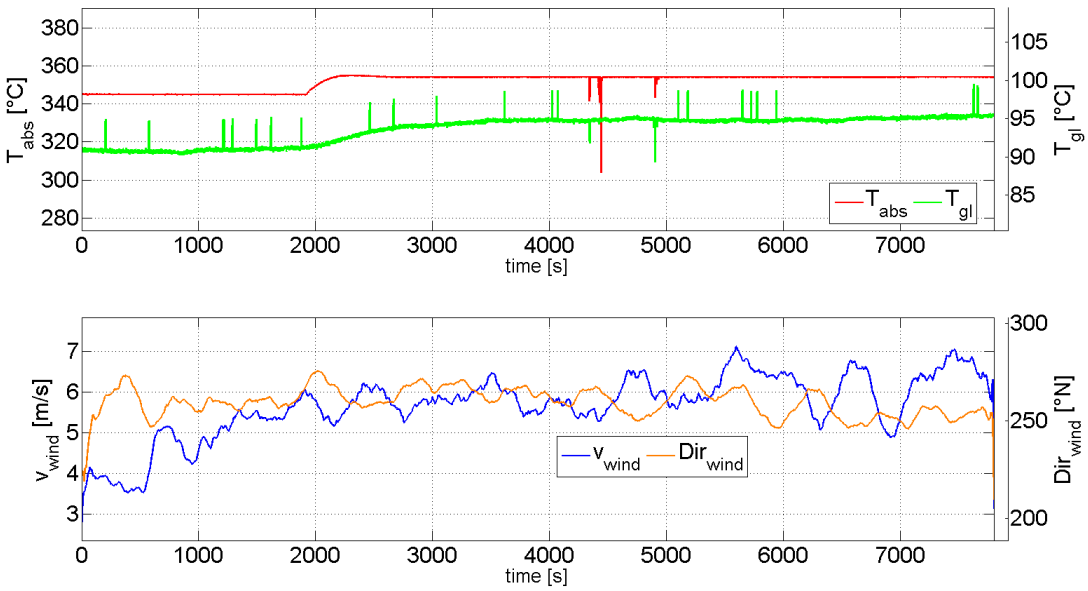

Figure 6.11: Measurement excerpt for high wind velocities and stable ambient temperature. Date of test: 09/02/2014, Ramp starts at 02:00 PM

During late afternoon measurements, around 05:00 PM, another ambient perturbation could be identified. In contrast to the first field experimental setup (Section 4.2.2), the experiment respectively the radiation shield was not shadowed by the PTC mirrors for the second field measurement campaign. Thus, thus the radiation shield was observed to be exposed to solar irradiation around 05:30 PM. This can be seen, as the glass temperature increases with a different profile than expected. One example of such a perturbation is illustrated in Fig. 6.12. This perturbation leads to an increase of the radiation shield temperature and affects the glass temperature.

The sun irradiation started at 5:30 PM at the same time of the glass temperature excitation. At 06:10 PM, the radiation shield is shadowed with a protective cover. The glass temperature is observed to decrease after this action. The steady-state glass temperature that is reached one hour after the start of the excitation is comparable to the other experiments. However the glass temperature response has been perturbated by solar irradiation, which leads to a miscalculation of A and φ values.

Three transient test were carried out in the transition period time between day and night. These time between 09:00 PM and 01:00 AM is characterized by a stable gradient of decreasing ambient temperature. The glass temperature correction method was applied on these measurement. The evaluation results of the original temperature profiles and the corrected temperature profiles are

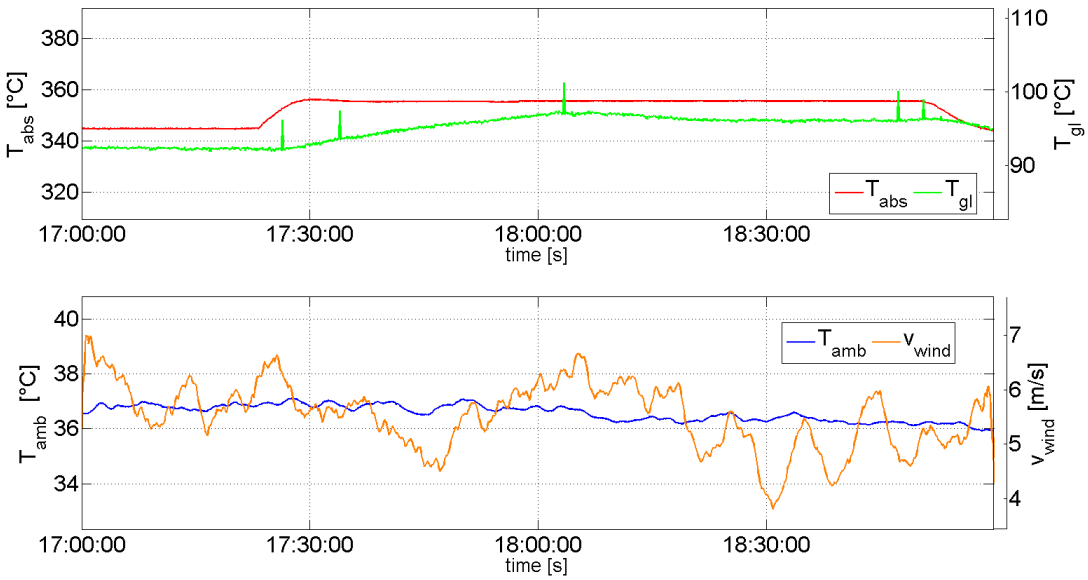

Figure 6.12: Example of a transient measurement influenced by solar irradiation. Date of test: 09/02/2014, Ramp start at 05:25 PM. From 05:30 PM, the sun shines directly on the radiation shield. Afterwards a cover was applied and the glass temperature decreases again

presented in Table 6.12.

Table 6.12: Results of measurement during stable ambient temperature gradient, original measurement and corrected temperature

	Original measurement		**Corrected measurement**	
	Average	σ	**Average**	σ
$\overline{T}_{gl}$ **[°C]**	84.77	0.07	86.66	0.06
$T_{gl,norm}$ **[°C]**	2.92	0.12	3.92	0.19
A [-]	0.0504	0.0022	0.0521	0.0039
φ **[rad]**	-1.397	0.009	-1.436	0.013
$\sigma_{algo}(T_{gl})$ **[K]**	0.14	0.01	0.14	0.4

It can be observed, that the correction method adjusts the influence of a negative ambient temperature gradient on the glass temperature correctly. The averaged glass temperature as well as the normalized glass temperature increases. Specially the normalized glass temperature approaches more previous laboratory measurement results. But it can not be observed, that the combination of A and φ values tends both to the previous observed average, which is around A = 0.065 and φ = -1.39 rad. The temperature correction method does not improve the repeatability of measurements. It might be able to correct single tests, which has to be proven in each case. The fitting

between simulated and measured temperature profile does not improve.

6.3.2 Experimental Results

The measurement results of relevant transient tests are presented in Table 6.13. Among the 12 transient measurements that were carried out in time windows with expected stable ambient temperature, 6 measurements were carried out during time windows with high ambient temperature variations than expected and were not evaluated. Among the measurement during stable ambient temperatures, 3 measurements occurred during daytime and 3 during nighttime. The average results are presented for the 6 measurements as well as for the day and night tests separately. The working point was 350 °C.

Table 6.13: Measurement results of additional field experiments with wind screen and optimal fan power setting

Number of tests	6 (3 at day / 3 at night)					
	Global measurements		**Day measurements**		**Night measurements**	
	Average	σ	**Average**	σ	**Average**	σ
$\overline{T}_{abs}$ **[°C]**	349.46	0.40	349.21	0.35	349.40	0.02
$\overline{T}_{gl}$ **[°C]**	86.85	4.83	91.53	1.06	82.19	0.25
$\overline{T}_{air}$ **[°C]**	34.36	6.23	40.68	0.059	28.24	0.02
$\overline{T}_{amb}$ **[°C]**	29.09	7.29	36.38	0.36	21.80	0.08
A [-]	0.0608	0.0036	0.0618	0.0046	0.0597	0.00057
φ**[rad]**	-1.418	0.012	-1.407	0.0053	-1.429	0.0025

Slight trends between the day measurements and night measurements can be distinguished. For daytime measurements, the ambient temperature was about 36 °C, while it decreased to 22 °C for night-time measurements. This difference leads to a higher average air and glass temperature for daytime measurements (Day: T_{air} = 40 °C, T_{gl} = 91 °C; Night: T_{air} = 28 °C, T_{gl} = 82 °C). In addition, the amplitude ratio A is higher for daytime measurements than for night-time measurements, and the phase shift φ is higher respectively faster during daytime. This trend is confirmed by standard deviation indicators for A and φ, which decrease when day and night measurements are separated. The effect of ambient/air temperature on A and phi is not observed for heat transfer numerical simulations, but is confirmed for the mean glass temperature.

One possible explanation for this experimental observation could be related to sky temperature. A clear, cloudless night is characterized by a low sky temperature. A low sky temperature leads to a higher differences of the radiation shield out surface and the sky, both temperatures in fourth power. The heat loss by thermal radiation could change and by this the heat loss balance within the radiation shield, as it is presented in Fig. 3.7, varies. So far, this is a not confirmed conclusion and could not be reproduced by simulations.

Using the overall average measurands, PTR thermal properties can be identified and specific heat loss can be simulated as in Subsection 6.2.2.2:

$$
\begin{aligned}
h_{ann} &= 0.0038 W/(m^2 \cdot K) \\
\epsilon_{abs} &= 11.81\ \% \\
\dot{q}'_{loss} &= 199.6 \pm 18.7\ W/m
\end{aligned}
$$

The uncertainty on the specific loss is higher in comparison to previous laboratory measurements (Section 6.2.2.2). A deviation of 24.6 W/m is observed in comparison to the corresponding steady-state measurement (175 ± 10 W/m), which corresponds to a relative deviation of 14 %.

7 Conclusion and Outlook

During this project, a transient infrared thermography measurement method for the determination of parabolic trough receiver heat losses was implemented for the first time under field conditions. The measurement method distinguishes itself from other steady state measurement methods by identifying the PTR thermal key properties, such as the absorber coating emissivity ϵ_{abs} and the annulus heat transfer coefficient h_{ann}. These thermal properties can be used to simulate the PTR specific heat loss under standard conditions. The experimental setup features a radiation shield, which reduces the PTR radiation heat exchange with the ambient.

The experimental setup was implemented at the KONTAS test facility at the Plataforma Solar de Almería in Spain. The heat transfer fluid temperature is regulated by a temperature control unit. The control parameters were adjusted in order to realize reproducible transient excitations.

After a first field measurement campaign, it was observed that wind velocity was one ambient parameter that could exert a significant influence on the glass temperature response and thus on the quality of transient measurands. To avoid the influence exerted by high wind velocities on the experimental setup, a wind screen solution was progressively optimized to protect the radiation shield outlet. The wind influence could be successfully reduced. In some cases, a stable transient measurement could be carried out with wind velocities around 8 m/s within critical wind directions. Still, some transient measurements were significantly influenced by the wind conditions, even with slower velocities than 6 m/s.

Field measurements were also carried at night time, in the absence of wind. The influence of ambient temperature variations during transient measurements was observed to perturb the glass temperature response. The ambient temperature shift is the crucial influence on the transient measurement method. This ambient perturbation exerts a critical influence on the transient measurement method.

During the first measurement campaign, the ratio of highly influenced transient measurements was around 50 %. Among unperturbated transient measurements, a high uncertainty was observed for the relevant transient measurements. Due to some irregularities in the infrared temperature measurement of the glass envelope, the experimental setup was further tested under laboratory conditions. The glass pyrometer infrared measurements did not show any further irregularities. Laboratory measurements could be reproduced with a lower uncertainty than field experiments.

A new wind screen was constructed and tested under laboratory conditions. The air flow within

the radiation shield was investigated for different fan power supply settings with the new wind screen under laboratory conditions. The experimental results obtained with a fan supply current of 650 mA were similar to the results obtained with the original experimental setup without wind screen and a fan supply current of 350 mA.

The wind screen was implemented for the next field measurement campaign. The field measurements were not longer perturbated by wind influences, even with wind velocities reaching up to 7 m/s. The failure ratio of transient experiments could be reduced significantly. The measurement results could be repeated with a low uncertainty among the transient measurement.

The identification of PTR thermal properties was achieved by combining a heat transfer numerical model in combination with an optimization algorithm, which searches for the best combination of absorber emissivity and annulus heat transfer coefficient that matches the transient measurands. For the laboratory and the additional field measurements, PTRs were identified as evacuated (h_{ann} = 0.004 W/(m$^2 \cdot$K). On the other hand, the absorber emissivities were higher in comparison to manufacturer data.

Table 7.1: Results of receiver thermal properties identification for transient measurements

Identified thermal properties	**Laboratory measurements**	**Field measurements**
$\boldsymbol{\epsilon_{abs}}$**[%]**	12.15	11.81
$\boldsymbol{h_{ann}}$**[W/(m$^2 \cdot$K)]**	0.0039	0.0038

The derived specific heat loss values are compared to previous steady-state heat loss laboratory measurements performed with DLR THERMOREC test bench. Besides it is assumed that the thermal properties of the PTC investigated in the laboratory differs slightly with the PTC installed on KONTAS test bench.

Table 7.2: Comparison of specific heat loss $\dot{q}'_{loss}$ values derived from transient measurements with steady-state heat loss measurements

	Laboratory receiver	**Field mounted receiver**
Transient measurements (PSA)	206 ± 6 W/m	199.6 ± 18.7 W/m
Steady state measurements (DLR Cologne, Thermorec)	198.5 ± 7.5 W/m	175 ± 10 W/m

The relative deviation between transient and steady-state heat loss values is about 4.1 % for the laboratory receiver and 14 % for the field mounted receiver.

The next steps in the development of the transient infrared thermography measurement method is the replacement of the glass pyrometer. The new pyrometer (*Sensortherm MY84*) is expected to show less irregularities in terms of outliers and noise in comparison to the pyrometer used during

this work (Dias Infrared DT44LH). Additional field measurements have to be performed at KONTAS with this new configuration.

To prove further the feasibility of field transient measurements, additional tests should be carried out in PTC loops. The HTF would not be heated up by a HTF temperature control unit but by the sun-tracking PTCs placed upstream of the investigated receiver tube in a non tracking PTC. The transient excitation would not be achieved by a HTF temperature control unit but by varying the HTF mass flow or by a dynamic defocusing and focusing of the upstream PTCs. This process has to be adapted at the Plataforma Solar de Almería.

To handle the critical impact of ambient temperature variation on the glass temperature profile, the dynamic heat transfer model determining first A and φ values, then thermal properties h_{ann} and ϵ_{abs} could be further developed. The existing first-order lag element model has to be extended to include the effect of ambient temperature variations. This means that the average air temperature should be replaced by the corresponding dynamic air temperature profile measured during the test.

Bibliography

[IEA, 2004] N.U.: *World Energy Outlook 2004.* International Energy Agency, 2004. ISBN 92-64-10817.

[Burkholder & Kutscher, 2008] BURKHOLDER, F. AND KUTSCHER, C.: *Heat Loss Testing of Solel's UVAC3 Parabolic Trough Receiver.* National Renewable Energy Laboratory technical report, 2008. NREL/TP-550-42394.

[Dreyer et al., 2010] DREYER, S., EICHEL, P., GNAEDIG, T., HACKER, Z., JANKER, S., KUCKELKORN, T., SILMY, K., PERNPEINTER, J. AND LUEPFERT, E.: *Heat loss measurements on parabolic trough receivers.* SolarPaces Conference, Perpignan, France, 21-25 September 2010.

[Duffie & Beckman, 2006] DUFFIE, J. A. AND BECKMAN, W. A.: *Solar Engineering of Thermal Processes.* John Wiley & Sons, INC, 2006. ISBN 978-0-471-69867-8.

[Forristall, 2003] FORRISTALL, R.: *Heat Transfer Analysis and Modeling of a Parabolic Trough Solar Receiver Implemented in Engineering Equation Solver.* National Renewable Energy Laboratory technical report, 2003. NREL/TP-550-34169.

[Gaertner, 2013] GAERTNER, D.: *Laboratory Heat Loss Measurements of Parabolic Trough Receivers Based on Transient Thermography.* Master thesis, University of Kassel, 2013.

[Geller, 2012] GELLER, J.: *Bestimmung der Waermeverluste von Receiverrohren Mittels Transienter Thermografie* Diploma thesis, Friedrich-Schiller-University of Jena, 2012.

[Gladen, 2009] GLADEN, H.: *Andasol - Europas erstes kommerzielles Parabolrinnenkraftwerk am Netz.* Technical report, SolarMillennium, 2009.

[Good, 2011] GOOD, P.: *Heat Transfer Modeling of a Solar Parabolic Trough Receiver by Direct Simulation Monte Carlo Method.* Master thesis, ETH Zuerich, 2011.

[Harding et al., 1985] HARDING, G., CHOW, S. AND COLLINS, R.: *Degradation of All-Glass Evacuated Solar Collector Tubes.* Solar Energy Materials Vol. 12, 1984.

[Heller et al., 2011] HELLER, P., MEYER-GRUENEFELDT, M., EBERT, M., JANOTTE, N., NOURI, B., POTTLER, K., PRAHL, C., REINALTER, W. AND ZARZA, E.: *Kontas - A Rotary Test Bench for Standardized Qualification of Parabolic Trough Components.* SolarPaces Conference, Granada, Spain, 20-23 September 2011.

[IMPAC, 1999] N.U.: *The Pyrometer Handbook.* IMPAC Infrared GmbH, 2004.

[Incropera et al., 2006] INCROPERA, R., DEWITT, D., BERGMAN, T. AND LAVINE, A.: *Fundamentals of Heat and Mass Transfer.* John Wiley & Sons, Inc., 2007. ISBN 978-0471457282.

[Kennedy, 2002] KENNEDY, C. E.: *Review of Mid- to High- Temperature Solar Selective Absorber Materials* National Renewable Energy Laboratory technical report, 2002. NREL/TP-520-31267

[Koertvelyessy, 1998] KOERTVELYESSY, L. V.: *Thermoelement-Praxis: neue theroretische Grundlagen und deren Umsetzung.* Vulkan-Verlag, 1998. ISBN 978-3802721816.

[Luepfert et al., 2008] LUEPFERT, E., RIFFELMANN, K.-J., PRICE, H., BURKHOLDER, F. AND MOSS, T.: *Experimental Analysis of Overall Thermal Properties of Parabolic Through Receivers.* Journal of Solar Energy Engineering, Vol 130, 2008.

[Lunze, 2004] LUNZE, J.: *Regelungstechnik.* Springer Verlag, 2004. ISBN 978-3540207429 .

[Meola and Carlomagno, 2004] MEOLA, C. AND CARLOMAGNO, G.: *Recent advances in the use of infrared thermography.* Measurement Science and Technologie, Vol 15, 2004.

[EASAC, 2011] N.U.: *Concentrating Solar Power: Its Potential Contribution to a Sustainable Energy Future.* European Academies Science Advisory Council (EASAC) Policy Report, 2011. ISBN: 978-3-8047-2944-5.

[Pfaender, 2006] PFAENDER, M.: *Pyrometrische Temperaturmessung an solarthermischen Hochtemperatur-Receivern.* PhD thesis, Faculty of Chemistry and Physics Faculty of Chemistry and Physics, Freiberg University of Mining and Technology, 2006.

[Potzel, 2009] POTZEL, P.: *Modeling and Simulation for Determination of Parabolic Trough Receiver Heat Losses Using Transient Thermography.* Diploma thesis, University of Stuttgart, 2009.

[Price et al., 2006] PRICE, H., FORRISTAL, R., WENDELIN, T. AND LEWANDOWSKI, A.: *Field survey of parabolic trough receiver thermal performance.* Solar 2006 Conference (ISEC'06), Denver, USA, 08-13 July 2006.

[Ratzel et al., 1979] RATZEL, A. C., HICKOX, C. E. AND GARTLING, D. K.: *Techniques for Reducing Thermal Conduction and Natural Convection Heat Losses in Annular Receiver Geometries.* Journal of Heat Transfer, Vol 101, 1979.

[Roeger et al., 2014] ROEGER, M., POTZEL, P., PERNPEINTNER, J. AND CARON, S.: *A transient thermography method to separate heat loss mechanisms in parabolic trough receivers.* Journal of Solar Energy Engineering, Vol. 136, P. 109-113, 2014.

[SCHOTT, 1999] N.U.: Schott borofloat 33 - The Versatile Floated Borosilicate Glass. Commercial brochure, Schott AG, 1999.

[Winter et al., 1991] WINTER, C.-J., SIZMANN, R. L. AND VANT-HULL, L. L.: *Solar Power Plants*. Springer Verlag, 1991.

Appendices

A Data Sheets

HCEOI12

Characteristics of the steel tube:	
Dimensions	Length 4060 mm, OD 70 mm, thickness 2 mm, at ambient temperature
Material	Longitudinally electric-welded austenitic stainless steel tube with lapped external surface
Characteristics of the glass tube:	
Dimensions	Length 3900 mm, OD 125 mm, thickness 3 mm
Material	Borosilicate glass
Transmittance of solar radiation with anti-reflective coating (%)[1,2]	≥ 96.6% according to ASTM standard [0.3…2.5μm]
Photo-thermal characteristics for spectrally selective coating:	
Solar absorbance[1]	≥96.0% according to ASTM standard [0.3…2.5μm]
Thermal emissivity[1]	≤8.5% @ 400°C
Note	The coating is stable in vacuum up to 600°C
Functional characteristics:	
Weight of the receiver	~ 28 kg
Heat Transfer Fluid	Mineral or synthetic diathermic oil
Physical state of the HTF	Liquid
Max operating condition	< 37 barg at maximum operating temperature of 400°C
Thermal losses[1,3]	< 265 W/m at 400°C (without any shield on the bellows)
Vacuum enclosure pressure	< 1.0 x 10^{-4} mbar
Expected lifetime	25 years
Aperture length ($L_{abs}/L_{HCE,nom}$)	0.961 at any HTF temperature
Note	-

[1] Average value for a reference lot | [2] Measured on the AR coated area | [3] Measured according to DLR procedure (ThermoRec equipment)

Figure A.1: Parabolic trough receiver data sheet

Product Information

SYLTHERM 800

Silicone Heat Transfer Fluid

SYLTHERM† 800 heat transfer fluid is a highly stable, long-lasting silicone fluid designed for high temperature liquid phase operation. It exhibits low potential for fouling and can often remain in service for 10 years or more. SYLTHERM 800 has essentially no odor, is low in acute oral toxicity, and is not listed as reportable under SARA Title III, Section 313††.

Recommended use temperature range:
-40°C (-40°F) to 400°C (750°F)

For health and safety information for this product, contact your Dow sales representative or call the number for your area on the second page of this sheet for a Material Safety Data Sheet (MSDS).

†† You may need to comply with similar or additional regulations in other countries.

Typical Properties of SYLTHERM 800 Fluid[1]

Composition: Dimethyl Polysiloxane

	As Supplied		After Extended Use	
Color:	Clear Yellow		Darkened	
Property	**SI Units**	**English Units**	**SI Units**	**English Units**
Viscosity @ 25°C (77°F)	9.1 mPa·s	9.1 cps	≥6.0 mPa·s	≥6.0 cp
Flash Point[3], Closed Cup, Typical	160°C	320°F	≥35°	≥95°
Flash Point[4], Open Cup, Typical	177°C	350°F	≥57°C	≥135°F
Fire Point[3]	193°C	380°F	≥68°C	≥155°F
Autoignition Point, ASTM D 2155	385°C	725°F	385°C	725°F
Acid Number, Typical	0.03		0.03	
Freeze Point	-60°C	-76°F	≤-40°C	≤-40°F
Density @ 25°C (77°F)	936 kg/m³	7.8 lb/gal	936kg/m³	7.8lb/gal
Specific Gravity 25°C (77°F)	0.93		0.93	
Heat of Combustion	28,659 kJ/kg	12,300 Btu/lb	28,659 kJ/kg	12,300 Btu/lb
Estimated Critical Temperature	367°C	692°F	367°C	692°F
Estimated Critical Pressure	10.9 bar	10.8 atm	10.9 bar	10.8 atm
Estimated Critical Volume	3.22 l/kg	0.0515 ft³/lb	3.22 l/kg	0.0515 ft³/lb

[1] Not to be construed as specifications
[2] Properties of the fluid at "equilibrium." Can be regarded as ongoing, long-term values for design purposes
[3] ASTM D92
[4] ASTM D93

Thermal Expansion of SYLTHERM 800 Fluid

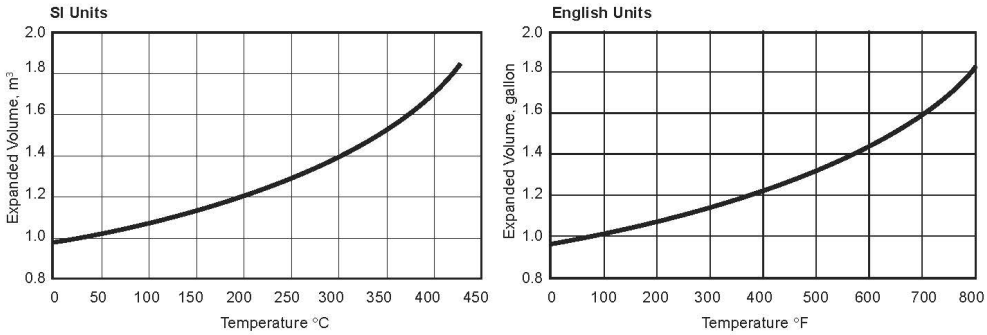

†Trademark of Dow Corning Corporation

Figure A.2: Kontas HTF data sheet - page 1

SYLTHERM 800
Silicone Heat Transfer Fluid

Saturated Liquid Properties of SYLTHERM 800 Fluid (SI Units)

Temp. °C	Specific Heat kJ/kg K	Density kg/m³	Thermal Conductivity W/m K	Viscosity mPa·s	Vapor Pressure kPa
-40	1.506	990.61	0.1463	51.05	0.00
0	1.574	953.16	0.1388	15.33	0.00
40	1.643	917.07	0.1312	7.00	0.10
80	1.711	881.68	0.1237	3.86	1.46
120	1.779	846.35	0.1162	2.36	9.30
160	1.847	810.45	0.1087	1.54	35.00
200	1.916	773.33	0.1012	1.05	94.60
240	1.984	734.35	0.0936	0.74	204.80
280	2.052	692.87	0.0861	0.54	380.20
320	2.121	648.24	0.0786	0.41	630.50
360	2.189	599.83	0.0711	0.31	961.20
400	2.257	547.00	0.0635	0.25	1373.00

Saturated Liquid Properties of SYLTHERM 800 Fluid (English Units)

Temp. °F	Specific Heat Btu/lb °F	Density lb/ft³	Thermal Conductivity Btu/hr ft² (°F/ft)	Viscosity cP	Vapor Pressure psia
-40	0.360	61.91	0.0845	51.00	0.00
40	0.378	59.32	0.0797	13.80	0.00
120	0.396	56.82	0.0749	6.10	0.00
200	0.414	54.37	0.0700	3.25	0.40
280	0.432	51.91	0.0652	1.94	2.60
360	0.451	49.38	0.0604	1.24	9.11
440	0.469	46.72	0.0555	0.83	23.42
520	0.487	43.90	0.0507	0.58	48.58
600	0.505	40.84	0.0459	0.42	86.84
680	0.523	37.49	0.0411	0.31	139.39
760	0.541	33.80	0.0362	0.24	206.50

For further information, call...

In The United States And Canada: 1-800-447-4369 • FAX: 1-517-832-1465
In Europe: +31 20691 6268 • FAX: +31 20691 6418
In The Pacific: +886 22 547 8731 • FAX: +886 22 713 0092
In Other Global Areas: 1-517-832-1556 • FAX: 1-517-832-1465

http://www.dow.com/heattrans

Published April 1998

NOTE: SYLTHERM heat transfer fluids are manufactured by Dow Corning Corporation and distributed by The Dow Chemical Company.

Printed in U.S.A.

NA/LA/Pacific: Form No. 176-01469-498 AMS
Europe: CH-153-311-E-498

Figure A.3: Kontas HTF data sheet - page 2

B Measurement Results

First Field Measurement Test Log - original experimental setup

Assesment:	no influence	critical influence	high influence

Date	Time	WP	Ambient Temperature		Wind		Irregularity	Rating / Comment
			T_amb, mean	Delta T_shift	v_wind	dir_wind		
		[°C]	[°C]	[K]	[m/s]	[°N]		
08.04.	11:00 AM	300	24	1	2	240	no	low influence
08.04.	1:50 PM	300	-	-	-	-	yes	high noise
08.04.	4:00 PM	300	-	-	-	-	yes	high noise
09.04.	1:00 PM	350	23	<1	6	90	no	low influence
10.04.	12:30 PM	350	25	1	3	290	no	low influence
10.04.	3:00 PM	350	27	<1	6	250	no	high influence
11.04.	12:00 PM	300	22	1	2	190	no	low influence
11.04.	12:45 PM	300	-	-	-	-	-	connection failure 12:30 PM
11.04.	2:45 PM	350	27	1.5	4	230	no	low influence
22.04.	3:30 PM	300	20	1.5	5	270	no	high influence
23.04.	12:30 PM	300	23	2	3	200	no	high influence
23.04.	4:00 PM	300	23	<1	4	250	no	no influence
24.04.	12:30 PM	350	22	1	5	230	no	low influence
24.04.	3:00 PM	350	-	-	-	-	-	bounced on pyrometer
28.04.	night	350	-	-	-	-	-	programming error
29.04.	night	350	-	-	-	-	-	KONTAS power black-out
30.05.	12:00 PM	350	25	4	3	200	no	high influence
05.05.	9:00 PM	350	20	2	5	90	no	high influence
05.05.	1:00 AM	350	15	2	3	100	no	high influence
05.05.	3:00 AM	350	13	<1	2	40	no	no influence
05.05.	6:30 AM	350	13	<1	3	50	no	no influence
06.05.	night	350	-	-	-	-	-	connection failure 21:30 PM
07.05.	9:00 PM	300	22	4	2	220	no	high influence
07.05.	1:00 AM	300	17	1.5	2	90	no	low influence
07.05.	5:00 AM	300	16	<1	4	90	no	high influence
08.05.	9:00 PM	300	20	4	3	110	no	high influence
08.05.	1:00 AM	300	14	1.5	1	100	no	low influence
08.05.	5:00 AM	300	-	-	-	-	-	programming error
12.05.	night	300	-	-	-	-	-	connection failure 21:00 PM
13.05.	night	300	-	-	-	-	-	connection failure 22:00 PM

Figure B.1: First field measurement test log - original setup

First Field Measurement Results - WP 300 - original experimental setup

Date		08.04.2014		11.04.2014		23.04.2014		07.05.2014		08.05.2014			
Time		11:00 AM		12:00 PM		12:30 PM		1:00 AM		1:00 AM			
Wind cover		no		no		no		no		no			
Fan power setting	[mA]	350		350		350		350		350			
Measurement Number		1st		1st		2nd		2nd		2nd			
Number of EndCuts		5		3		5		5		5			
First and last EndCut	[s]	1500	3500	1500	2500	1500	3500	1500	3500	1500	3500		
Emissivity Absorber	[-]	0.505		0.49		0.503		0.55		0.55		**statistics:**	
		mean	std	mean	std	mean	std	mean	std	mean	std	**mean**	**std**
T_air_mean	[°C]	24.21	0.25	23.65	0.24	89.25	0.53	16.73	0.06	15.14	0.04	33.80	27.96
T_abs_mean	[°C]	298.09	0.05	298.17	0.06	298.12	0.04	296.90	0.05	298.32	0.03	297.92	0.51
T_gl_mean	[°C]	61.91	0.18	62.59	0.04	62.42	0.18	58.70	0.22	62.94	0.18	61.71	1.54
AR - Algo1 - mean	[-]	0.0482	0.0011	0.0506	0.0019	0.0458	0.0011	0.0346	0.0020	0.0316	0.0020	0.0421	0.0076
AR - Algo2 - mean	[-]	0.0490	0.0022	0.0537	0.0013	0.0416	0.0012	0.0368	0.0022	0.0337	0.0010	0.0430	0.0074
AR - Global - mean	[-]	0.0484	0.0012	0.0515	0.0017	0.0446	0.0010	0.0356	0.0019	0.0322	0.0016	0.0425	0.0074
PS - Algo1 - mean	[rad]	-1.450	0.005	-1.437	0.011	-1.432	0.007	-1.483	0.011	-1.482	0.016	-1.457	0.022
PS - Algo2 - mean	[rad]	-1.447	0.010	-1.426	0.009	-1.446	0.008	-1.474	0.015	-1.468	0.008	-1.452	0.017
PS - Global - mean	[rad]	-1.449	0.006	-1.434	0.010	-1.436	0.006	-1.479	0.012	-1.478	0.012	-1.455	0.020
T_abs_norm	[°C]	10.60	0.09	10.49	0.12	10.41	0.07	10.70	0.09	10.29	0.06	10.50	0.14
T_gl_norm	[°C]	4.02	0.40	3.61	0.11	3.22	0.35	3.64	0.49	2.89	0.36	3.48	0.39
Delta Algo1	[°C]	0.010	0.300	-0.073	0.042	0.007	0.175	-0.018	0.183	0.093	0.171	0.004	0.081
Delta Algo2	[°C]	0.001	0.187	-0.049	0.007	0.007	0.071	-0.014	0.065	0.042	0.090	-0.003	0.046
ST. Dev. Algo1	[K]	0.163	0.046	0.118	0.001	0.144	0.008	0.099	0.031	0.090	0.028	0.123	0.047
St. Dev. Algo2	[K]	0.169	0.050	0.119	0.002	0.152	0.006	0.108	0.038	0.098	0.028	0.129	0.049
T_amb	[°C]	25.21	0.66	24.77	0.48	24.27	0.44	16.49	0.23	15.01	0.21	21.15	9.55
Pyrometer2 Noise	[K]	0.12	0.00	0.12	0.00	0.12	0.00	0.12	0.00	0.12	0.00	0.12	0.05

Figure B.2: First field measurement results - WP 300 - original setup

First Field Measurement Results - WP 350 – original experimental setup

Date		09.04.2014		10.04.2014		11.04.2014		24.05.2014		05.05.2014		05.05.2014	
Time		1:00 PM		12:30 PM		14:45 PM		12:30 PM		3:00 AM		6:30 AM	
Wind cover		no		no		no		no		no		no	
Fan power setting	[mA]	350		350		350		350		350		350	
Measurement Number		1st		1st		3rd		1st		3rd		4th	
Number of EndCuts		5		5		5		5		5		5	
First and last EndCut	[s]	1500	3500	1500	3500	1500	3500	1500	3500	1500	3500	1500	3500
Emissivity Absorber	[-]	0.485		0.49		0.5		0.53		0.538		0.538	
		mean	std	mean	std	mean	std	mean	std	mean	std	mean	std
T_air	[°C]	24.48	0.09	25.48	0.04	26.80	0.11	23.16	0.20	12.13	0.06	12.17	0.04
T_abs	[°C]	347.01	0.07	346.59	0.12	347.08	0.11	347.80	0.13	348.42	0.08	348.47	0.05
T_gl	[°C]	89.37	0.30	81.69	0.13	82.69	0.15	79.08	0.22	80.95	0.16	80.55	0.16
AR - Algo1 - mean	[-]	0.0650	0.0075	0.0791	0.0037	0.0662	0.0022	0.0497	0.0022	0.0565	0.0025	0.0713	0.0028
AR - Algo2 - mean	[-]	0.0578	0.0040	0.0773	0.0021	0.0674	0.0008	0.0466	0.0028	0.0549	0.0011	0.0699	0.0016
AR - Global - mean	[-]	0.0629	0.0060	0.0786	0.0032	0.0666	0.0016	0.0488	0.0017	0.0560	0.0020	0.0709	0.0024
PS - Algo1 - mean	[rad]	-1.453	0.034	-1.408	0.015	-1.404	0.010	-1.441	0.013	-1.433	0.014	-1.408	0.012
PS - Algo2 - mean	[rad]	-1.468	0.018	-1.413	0.011	-1.398	0.006	-1.452	0.018	-1.435	0.006	-1.414	0.008
PS - Global - mean	[rad]	-1.457	0.028	-1.409	0.014	-1.402	0.008	-1.444	0.011	-1.433	0.012	-1.410	0.011
T_abs_ norm	[°C]	10.28	0.13	10.75	0.24	10.04	0.23	9.98	0.27	10.32	0.16	10.31	0.10
T_gl_norm	[°C]	4.98	0.66	4.98	0.20	3.66	0.25	3.64	0.48	3.92	0.36	4.38	0.32
Delta Algo1	[°C]	-0.016	0.480	0.024	0.134	0.146	0.258	-0.059	0.399	-0.002	0.140	-0.016	0.284
Delta Algo2	[°C]	0.032	0.208	0.051	0.086	0.110	0.214	-0.004	0.180	-0.011	0.064	0.007	0.210
ST. Dev. Algo1	[K]	0.305	0.057	0.170	0.009	0.101	0.028	0.212	0.042	0.093	0.012	0.099	0.039
St. Dev. Algo2	[K]	0.332	0.082	0.174	0.010	0.105	0.029	0.228	0.047	0.097	0.013	0.103	0.037
T_amb	[°C]	24.73	0.45	25.37	0.08	26.28	0.71	23.59	0.24	12.14	0.39	12.25	0.13
Pyrometer2 Noise	[K]	0.11	0.00	0.11	0.00	0.12	0.00	0.11	0.00	0.13	0.00	0.13	0.01

Figure B.3: First field measurement results - WP 350 - original setup

First Field Measurement Test Log - with wind screen

Assessment: no influence | critical influence | high influence

Date	Time	WP	Ambient Temperature		Wind		Irregularity	Rating / Comment
			T_amb, mean	Delta T_shift	v_wind	dir_wind		
		[°C]	[°C]	[K]	[m/s]	[°N]		
14.05.	9:30 AM	300	21	<1	9	100	no	no influence
14.05.	1:00 PM	300	-	-	-	-	-	connection failure 12:00 PM
14.05.	2:30 PM	300	21	<0.5	9	90	no	no influence
15.05.	9:45 AM	350	16	1	8	90	no	high influence
15.05.	1:15 PM	350	20	<1	8	100	no	low influence
15.05.	night	350	-	-	-	-	-	connection failure 09:00 PM
19.05.	8:00 PM	300	18	3	1.5	250	yes	defective temeprature signal
19.05.	12:00 AM	300	15	3	1.5	250	yes	defective temperature signal
19.05.	night	300	-	-	-	-	-	connection failure 03:00 AM
20.05.	7:00 PM	300	26	1	5	230	Yes	defective temeprature signal
20.05.	night	300	-	-	-	-	-	KONTAS dysfunction 10:30 PM
26.05.	6:00 PM	350	24	1	4	260	yes	defective temeprature signal
26.05.	3:00 AM	350	15	2	2	90	no	low influence
26.05.	6:00 AM	350	14	3	4	90	no	high influence
27.05.	12:00 PM	350	22	3	4	250	no	high influence
27.05.	7:00 PM	350	22	1	5	250	no	high influence
27.05.	2:00 AM	350	15	1	2	100	no	low influence
27.05.	night	350	-	-	-	-	-	connection failure 03:30 AM
28.05.	11:00 AM	350	23	3	6	240	no	high influence
28.05.	night	350	-	-	-	-	-	KONTAS power blackout
28.05.	9:00 PM	350	22	1	4	300	no	high influence
28.05.	1:30 AM	350	18	3	2	300	no	high influence
28.05.	6:00 AM	350	15	3	2	0	no	high influence
29.05.	10:15 AM	350	22	1	3	200	no	high influence
29.05.	1:00 PM	350	24	1	2	200	no	high influence
29.05.	3:00 PM	350	25	1	4	240	no	high influence

Figure B.4: First field measurement test log - with wind screen

First Field Measurement Results - WP 300 – with wind sheet

Date		14.05		14.05			
Time		9:30 AM		2:30 AM			
Wind cover		Wind sheet		Wind sheet			
Fan power setting	[mA]	600		600			
Measurement Number		1st		2nd			
Number of EndCuts		5		5			
First and last EndCut	[s]	1500	3500	1500	3500		
Emissivity Absorber	[-]	0.485		0.485		**statistics:**	
		mean	std	mean	std	**mean**	**std**
T_air_mean	[°C]	23.14	0.12	24.64	0.05	23.89	0.75
T_abs_mean	[°C]	297.27	0.06	297.43	0.09	297.35	0.08
T_gl_mean	[°C]	62.79	0.14	64.22	0.18	63.50	0.71
AR - Algo1 - mean	[-]	0.0545	0.0006	0.0492	0.0015	0.0519	0.0026
AR - Algo2 - mean	[-]	0.0555	0.0007	0.0498	0.0018	0.0526	0.0029
AR - Global - mean	[-]	0.0548	0.0004	0.0494	0.0013	0.0521	0.0027
PS - Algo1 - mean	[rad]	-1.434	0.003	-1.424	0.010	-1.429	0.005
PS - Algo2 - mean	[rad]	-1.431	0.004	-1.422	0.013	-1.426	0.005
PS - Global - mean	[rad]	-1.433	0.002	-1.424	0.009	-1.428	0.005
T_abs_norm	[°C]	10.40	0.12	9.91	0.19	10.16	0.24
T_glass_norm	[°C]	3.92	0.27	2.98	0.38	3.45	0.47
Delta Algo1	[°C]	0.026	0.104	0.037	0.206	0.031	0.006
Delta Algo2	[°C]	0.017	0.046	0.016	0.097	0.017	0.001
ST. Dev. Algo1	[K]	0.131	0.003	0.102	0.009	0.117	0.014
St. Dev. Algo2	[K]	0.131	0.007	0.110	0.012	0.120	0.011
T_amb	[°C]	20.07	0.24	21.14	0.16	20.60	0.53
Pyrometer2 Noise	[K]	0.12	0.00	0.12	0.00	0.12	0.00

Figure B.5: First field measurement results - WP 300 - with wind screen

First Field Measurement Results - WP 350 – with wind screen

Date		15.05.2014		26.05.2014		27.05.2014			
Time		1:30 PM		3:00 AM		7:00 PM			
Wind cover		Wind sheet		Wind sheet		Wind sheet			
Fan power setting	[mA]	600		600		600			
Measurement Number		2nd		2nd		2nd			
Number of EndCuts		5		5		5			
First and last EndCut	[s]	2000	4000	2000	4000	2000	4000		
Emissivity Absorber	[-]	0.485		0.485		0.485		**statistik:**	
		mean	std	mean	std	mean	std	**mean**	**std**
T_air_mean	[°C]	25.68	0.16	23.07	0.04	19.10	0.01	22.62	0.07
T_abs_mean	[°C]	346.08	0.03	345.06	0.08	346.32	0.08	345.82	0.02
T_gl_mean	[°C]	81.34	0.24	74.64	0.09	70.16	0.11	75.38	0.07
AR - Algo1 - mean	[-]	0.0682	0.0071	0.0720	0.0021	0.0693	0.0034	0.0698	0.0021
AR - Algo2 - mean	[-]	0.0618	0.0060	0.0690	0.0014	0.0677	0.0026	0.0662	0.0020
AR - Global - mean	[-]	0.0663	0.0067	0.0711	0.0018	0.0688	0.0031	0.0687	0.0020
PS - Algo1 - mean	[rad]	-1.396	0.034	-1.394	0.009	-1.362	0.017	-1.384	0.011
PS - Algo2 - mean	[rad]	-1.416	0.029	-1.402	0.007	-1.368	0.014	-1.395	0.009
PS - Global - mean	[rad]	-1.402	0.032	-1.396	0.008	-1.364	0.016	-1.387	0.010
						0	0		
T_abs _norm	[°C]	11.23	0.06	10.12	0.17	9.86	0.16	10.40	0.05
T_gl_norm	[°C]	4.27	0.43	3.98	0.18	3.23	0.21	3.83	0.11
Delta Algo1	[°C]	0.116	0.304	0.023	0.109	0.009	0.135	0.049	0.086
Delta Algo2	[°C]	0.115	0.196	0.011	0.072	0.010	0.095	0.045	0.054
ST. Dev. Algo1	[K]	0.183	0.028	0.110	0.008	0.091	0.016	0.128	0.008
St. Dev. Algo2	[K]	0.174	0.031	0.108	0.012	0.091	0.017	0.124	0.008
T_amb	[°C]	20.46	0.30	15.28	0.44	13.04	0.27	16.26	0.07
Pyrometer2 Noise	[K]	0.11	0.00	0.12	0.00	0.12	0.00	0.12	0.00

Figure B.6: First field measurement results - WP 350 - with wind screen

Laboratory Measurements - WP 350 – originial experimental setup

Date		19.06.		19.06.		19.06.			
Time		9:00 AM		1:00 PM		5:00 PM			
Wind cover		no		no		no			
Fan power setting	[mA]	350		350		350			
Measurement Number		1st		2nd		3rd			
Number of EndCuts		5		5		5			
First and last EndCut	[s]	2000	4000	2000	4000	2000	4000		
Emissivity Absorber	[-]	0.485		0.485		0.485		**statistics:**	
		mean	std	mean	std	mean	std	**mean**	**std**
T_air_mean	[°C]	25.71	0.05	25.81	0.01	26.23	0.07	25.92	0.23
T_abs_mean	[°C]	349.10	0.11	349.68	0.11	349.92	0.15	349.57	0.34
T_gl_mean	[°C]	74.91	0.13	75.11	0.21	75.36	0.41	75.12	0.19
AR - Algo1 - mean	[-]	0.0629	0.0014	0.0631	0.0014	0.0622	0.0006	0.0628	0.0004
AR - Algo2 - mean	[-]	0.0641	0.0011	0.0616	0.0006	0.0654	0.0028	0.0637	0.0016
AR - Global - mean	[-]	0.0634	0.0012	0.0625	0.0009	0.0635	0.0014	0.0631	0.0005
PS - Algo1 - mean	[rad]	-1.401	0.006	-1.389	0.013	-1.401	0.006	-1.397	0.006
PS - Algo2 - mean	[rad]	-1.398	0.005	-1.394	0.004	-1.383	0.034	-1.391	0.006
PS - Global - mean	[rad]	-1.400	0.005	-1.391	0.008	-1.394	0.017	-1.395	0.004
						0	0		
T_abs _norm	[°C]	9.44	0.17	10.14	0.22	9.75	0.29	9.78	0.28
T_gl_norm	[°C]	3.59	0.48	3.44	0.45	3.19	0.73	3.40	0.16
Delta Algo1	[°C]	-0.027	0.108	0.002	0.058	0.021	0.061	-0.001	0.020
Delta Algo2	[°C]	-0.027	0.073	0.002	0.036	0.001	0.037	-0.008	0.014
ST. Dev. Algo1	[K]	0.076	0.023	0.057	0.003	0.059	0.003	0.064	0.009
St. Dev. Algo2	[K]	0.077	0.025	0.056	0.004	0.060	0.008	0.064	0.009
T_amb	[°C]	22.07	0.04	22.00	0.05	22.56	0.11	22.21	0.25
Pyrometer2 Noise	[K]	0.11	0.00	0.11	0.00	0.11	0.00	0.11	0.00

Figure B.7: Laboratory measurement results - WP 350 - original setup

Laboratory Measurements - WP 350 – with new wind screen

Date		17.07.		18.07.		18.07.			
Time		1:00 PM		9:00 AM		1:00 PM			
Wind cover		Iron wind sheet		Iron wind sheet		iron wind sheet			
Fan power setting	[mA]	650		650		650			
Measurement Number		1		1		2			
Number of EndCuts		5		5		5			
First and last EndCut	[s]	2000	4000	2000	4000	2000	4000		
Emissivity Absorber	[-]	0.485		0.485		0.485		**statistics:**	
		mean	std	mean	std	mean	std	**mean**	**std**
T_air_mean	[°C]	28.25	0.03	27.48	0.01	28.88	0.03	28.20	0.57
T_abs_mean	[°C]	348.34	0.08	348.66	0.04	349.22	0.10	348.74	0.36
T_gl_mean	[°C]	80.72	0.06	79.72	0.10	80.72	0.09	80.39	0.47
AR - Algo1 - mean	[-]	0.0642	0.0004	0.0629	0.0007	0.0655	0.0011	0.0642	0.0010
AR - Algo2 - mean	[-]	0.0633	0.0004	0.0650	0.0005	0.0659	0.0006	0.0647	0.0011
AR - Global - mean	[-]	0.0640	0.0004	0.0635	0.0006	0.0656	0.0009	0.0644	0.0009
PS - Algo1 - mean	[rad]	-1.403	0.002	-1.394	0.003	-1.395	0.005	-1.397	0.004
PS - Algo2 - mean	[rad]	-1.405	0.002	-1.387	0.003	-1.395	0.003	-1.396	0.007
PS - Global - mean	[rad]	-1.403	0.002	-1.392	0.003	-1.395	0.004	-1.397	0.005
						0	0		
T_abs _norm	[°C]	9.01	0.16	10.64	0.09	9.77	0.19	9.81	0.67
T_gl_norm	[°C]	3.40	0.10	3.72	0.12	3.68	0.13	3.60	0.14
Delta Algo1	[°C]	0.011	0.085	0.007	0.050	-0.070	0.063	-0.017	0.037
Delta Algo2	[°C]	0.012	0.063	-0.005	0.038	-0.050	0.040	-0.014	0.026
ST. Dev. Algo1	[K]	0.067	0.002	0.067	0.001	0.079	0.002	0.071	0.006
St. Dev. Algo2	[K]	0.067	0.003	0.068	0.002	0.080	0.002	0.072	0.006
T_amb	[°C]	24.95	0.07	23.12	0.05	24.65	0.07	24.24	0.80
Pyrometer2 Noise	[K]	0.11	0.00	0.12	0.00	0.11	0.00	0.11	0.00

Figure B.8: Laboratory measurement results - WP 350 - with new wind screen

Additional Field Measurements - Test Log - with new wind screen

Assessment: no influence | critical influence | high influence

Date	Time	WP	Ambient Temperature		Wind		Irregularity	Rating / Comment
			T_amb, mean	Delta T_shift	v_wind	dir_wind		
		[°C]	[°C]	[K]	[m/s]	[°N]		
02.09.	2:00 PM	350	26	<0.5	6	250	no	no influence
02.09.	5:30 PM	350	36	1	6	240	no	sun irradiated
02.09.	10:00 PM	350	30	3	2	250	no	high influenced
02.09.	1:00 AM	350	24	<0.5	1	200	no	no influence
02.09.	3:30 AM	350	24	2	4	100	no	high influenced
03.09.	2:30 PM	350	36	<0.5	6	260	no	no influence
03.09.	5:30 PM	350	35	<1	4	260	no	no influence
03.09.	9:00 PM	350	32	3	3	200	no	high influenced
03.09.	1:30 AM	350	23	2	1	200	no	high influenced
03.09.	4:00 AM	350	22	2	1	90	no	high influenced
03.09.	6:30 AM	350	22	<1	3	30	no	no influence
04.09.	10:00 PM	350	26	3	2	200	no	high influenced
04.09.	1:30 AM	350	23	<1	2	100	no	no influence
04.09.	4:00 AM	350	21	2	1	40	no	high influenced
04.09.	6:30 AM	350	20	<1	1	100	no	no influence

Figure B.9: Additional field measurement test log - WP 350 - with new wind screen

Additional Field Measurements – WP 350 – with new wind screen

Date		02.09.		02.09.		03.09.		03.09.		03.09.		04.09.	
Time		2:00 PM		5:30 PM		2:30 PM		17:30 PM		6:30 AM		1:30 AM	
Wind cover		iron wind sheet		iron wind sheet		iron wind sheet		iron wind sheet		iron wind sheet		iron wind sheet	
Fan power setting	[mA]	650		650		650		650		650		650	
Measurement Number		1st		4th		1st		2nd		6th		2nd	
Number of EndCuts		5		5		5		5		5		5	
First and last EndCut	[s]	2000	4000	2000	4000	2000	4000	2000	4000	2000	4000	2000	4000
Emissivity Glass	[-]	0.44		0.44		0.465		0.465		0.465		0.465	
		mean	std	mean	std	mean	std	mean	std	mean	std	mean	std
T_air_mean	[°C]	40.69	0.03	29.12	0.01	40.74	0.04	40.60	0.03	27.48	0.06	28.12	0.02
T_abs_mean	[°C]	349.56	0.03	349.90	0.02	348.73	0.09	349.32	0.30	349.43	0.07	348.86	0.04
T_gl_mean	[°C]	92.94	0.14	84.15	0.10	90.39	0.09	91.25	0.08	80.94	0.15	81.48	0.10
AR - Algo1 - mean	[-]	0.0657	0.0020	0.0605	0.0015	0.0564	0.0003	0.0659	0.0029	0.0576	0.0020	0.0609	0.0003
AR - Algo2 - mean	[-]	0.0621	0.0021	0.0592	0.0010	0.0531	0.0005	0.0646	0.0015	0.0575	0.0016	0.0622	0.0009
AR - Global - mean	[-]	0.0646	0.0018	0.0601	0.0013	0.0554	0.0003	0.0655	0.0025	0.0576	0.0018	0.0613	0.0004
PS - Algo1 - mean	[rad]	-1.409	0.011	-1.429	0.006	-1.404	0.001	-1.398	0.013	-1.431	0.008	-1.428	0.001
PS - Algo2 - mean	[rad]	-1.420	0.008	-1.432	0.005	-1.415	0.003	-1.403	0.007	-1.430	0.009	-1.424	0.005
PS - Global - mean	[rad]	-1.412	0.009	-1.430	0.006	-1.408	0.001	-1.400	0.011	-1.431	0.008	-1.427	0.002
						0	0						
T_abs _norm	[°C]	9.16	0.06	10.56	0.03	8.67	0.15	9.85	0.60	9.03	0.13	9.11	0.08
T_gl_norm	[°C]	3.63	0.20	4.25	0.20	2.87	0.12	3.59	0.13	3.55	0.25	3.77	0.21
Delta Algo1	[°C]	-0.003	0.155	0.056	0.147	0.006	0.101	0.046	0.222	0.082	0.253	0.041	0.172
Delta Algo2	[°C]	0.017	0.100	0.034	0.104	0.019	0.069	0.036	0.166	0.067	0.186	0.020	0.122
ST. Dev. Algo1	[K]	0.088	0.014	0.114	0.022	0.074	0.006	0.125	0.025	0.111	0.049	0.078	0.009
St. Dev. Algo2	[K]	0.093	0.014	0.113	0.023	0.078	0.006	0.126	0.020	0.115	0.048	0.081	0.009
T_amb	[°C]	36.58	0.08	22.58	0.30	36.45	0.27	36.10	0.93	21.43	0.40	21.41	0.21
Pyrometer2 Noise	[K]	0.11	0.00	0.11	0.00	0.10	0.00	0.11	0.00	0.11	0.00	0.11	0.00

Figure B.10: Additional field measurement results - WP 350 - with new wind screen